POLITECNICO DI TORINO

Master's Degree in Environmental and Land Engineering

Master's Degree Thesis

Earth Observation in Mining Activities: Phosphate Deposits in Morocco

Supervisor
PROFESSOR PIERO BOCCARDO

Co-Supervisor
SUSANNA GRITA (PHD CANDIDATE)

Candidate
SHAHABEDDIN SAHRAEIAN

October 2024

Summary

Identifying surface minerals remotely is crucial for natural resource management. Remote sensing enables efficient mapping of mineral distributions, benefiting the mining and energy sectors by reducing the costs and difficulties of on-the-ground exploration.

Mineral detection through hyperspectral sensors offers a powerful tool for characterizing ore deposits. However, challenges arise when minerals exhibit featureless spectral responses in certain sensor wavelength ranges or when overlapping spectral features complicate distinction.

To address these challenges, this study repurposes the ECOSTRESS sensor, originally developed to monitor Earth's surface temperature, for detecting and characterizing ore and host minerals of phosphate mines, essential for industrial applications.

In this study, the NDVI was used to characterize vegetation patterns in the Youssouffia region over five months in 2023. ECOSTRESS and EMIT images were acquired after selecting the appropriate preprocessing level. For ECOSTRESS, swath data was converted to GeoTIFF using a Python script, followed by band stacking, clipping, and conversion from emissivity to reflectance. Mineral spectral features were extracted in hyperspectral analysis and compared against spectral libraries.

While EMIT shows promise in hyperspectral analysis, it faces limitations when studying minerals with overlapping or featureless spectra in certain wavelengths (e.g., SWIR). ECOSTRESS data was used for spectral analysis, yielding valuable results in distinguishing key minerals such as quartz and apatite, which are integral to phosphate mining.

Although both EMIT and ECOSTRESS have technical shortcomings, reexamining the methodology with other sensors and satellites could enhance the reliability of this study. Ground truth verification and field studies would strengthen the results and provide a foundation for future applications, including AI training in mineral exploration.

Acknowledgements

I would like to express my deepest gratitude to Professor Piero Boccardo for his invaluable guidance, expertise, and unwavering support throughout the course of my thesis. His mentorship has been instrumental in shaping the direction of my research.

I am also grateful to Susanna Grita for her assistance and encouragement, which helped me navigate various challenges during this project.

And to my beloved Marziyeh, your endless support, patience, and love have been my greatest motivation. You have been my anchor through the challenges, reminding me of the strength we share. Together, we turn every hurdle into a stepping stone, making each victory even more meaningful.

Table of Contents

List of Tables

List of Figures

Chapter 1

Introduction

Since the beginning of the protectorate period in 1912, Morocco has been attempting to develop its economy on a modern basis. As the country is richly endowed with various natural resources, it was logical to promote mining initially. The urban middle class showed little interest in these issues and was thus reluctant to invest. The state had to step in everywhere. It advanced exploration in all parts of the country and founded companies that took over the exploitation of the most valuable deposits.[1]

1.1 General Situation

Mining has not lost its paramount importance to this day. In recent years, the country has consistently produced significant quantities of iron, manganese, lead, zinc, cobalt, copper, and antimony ores, anthracite and barite, and even some oil and gold. The mining sector provided employment opportunities for 41,000 individuals, supporting a significant portion of the workforce and contributing to the economic stability of the region.[2]
The entire phosphate industry is favored by the following fortunate circumstances:

Morocco was the top global exporter of phosphate rock, phosphoric acid, and phosphate fertilizers; it was the second-largest producer of phosphate rock, following China, contributing approximately 15.6% of the world's phosphate rock production in 2019. Together, Morocco and Western Sahara possessed 50 billion metric tons of phosphate rock reserves, amounting to about 70% of the world's total reserves.[2]

Unlike metallic ores, they are conveniently located on the so-called Phosphate Plateau before the Atlas, only 100 to 150 km from the Atlantic coast.

The exploitation of the unfolded, practically horizontal deposits poses no special problems and can even be partly carried out in open-pit mining.

In 2018, the mineral sector was the government's primary source of foreign exchange, with the phosphate rock mining and phosphate-based products industry remaining a key export sector, contributing roughly 19% to the country's total export value.[2]

1.2 The Phosphate Deposits

The phosphate deposits discovered so far are extensive, stretching almost continuously along the northern edge of the High Atlas from southwest to northeast, with the most significant concentrations located on the Phosphate Plateau around Khouribga-Oued-Zem. [3] Additionally, there are scattered deposits in the Middle and High Atlas regions, extending south of Marrakech all the way to the Ouarzazate area. Presently, mining activities are mainly concentrated on two key deposits: Ouled-Abdoun near Khouribga-Oued-Zem and Gantour near Youssoufia,

previously known as Louis-Gentil. These two sites are the primary focus of Morocco's phosphate mining industry due to their substantial reserves and strategic importance.

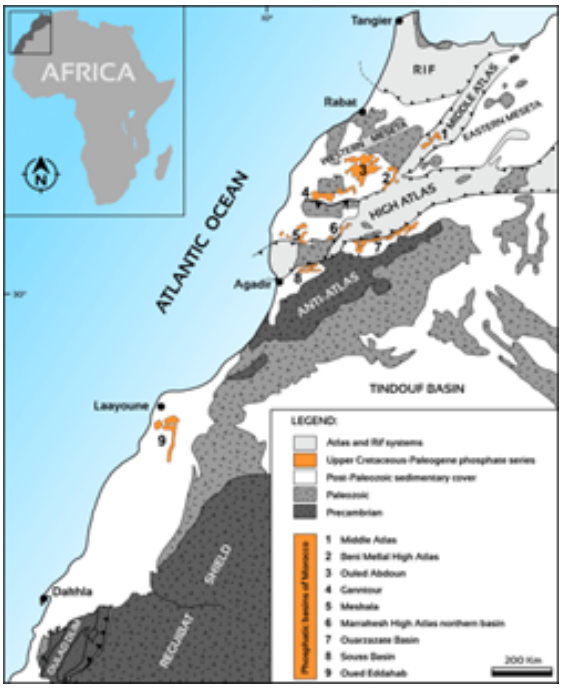

Figure 1.1: Simplified geological map of Morocco illustrating the distribution of phosphate accumulations in the different structural domains of Morocco[3]

Moroccan phosphates were formed 60 to 70 million years ago (Eocene) in a shallow, warm marine environment. They likely resulted from chemical precipitation as deep, phosphorus-rich waters rose to the surface. The cooler, phosphorus-laden waters mixed with the warmer shelf waters, causing phosphorus and calcium to precipitate. This episodic process explains the rhythmic layers in the deposits, known as the abiolithic theory.

1.3 The Mines of Youssouffia

In 1930, the foundation of Youssoufia was laid following the discovery of a phosphate deposit in the Gantour plateau by the French geologist Lois Gentil. The city originally bore the name of Gentil until 1960 when it was renamed Youssoufia by King Mohamed V, commemorating his visit on that date. The exploitation and development of these phosphate deposits, along with the increasing demand for labor, have significantly contributed to the city's economic growth and accelerated

its urbanization.

In 2021, the OCP Group extracted 24.5 million tons of dry, merchant-grade (DMG) phosphate rock across its mining sites. This included 17.8 million tons from Khouribga, 5 million tons from Gantour, and 1.8 million tons from Phosboucraâ. The increased extraction volumes at Khouribga (12.1 million tons) and Gantour (1.5 million tons) contributed to 37% of phosphate rock shipments, with Khouribga accounting for 40% and Gantour for 23% of these shipments.

1.4 Transportation and Shipment

The rail connection, managed by Morocco's leading export earner, the state-owned Office Cherifien des Phosphates (OCP), links the phosphate mines in Youssoufia with the chemical plants in Safi.[4]

1.5 Production and Export

Production and export have not always developed uniformly since the opening of the Khouribga mines in 1921. In 1930, 2,000,000 tons were produced for the first time. The economic crisis of the 1930s and World War II interrupted the upward trend.[1] From 1945 onwards, the activities of the O.C.P. steadily unfolded, barely influenced by the economic uncertainty following the end of the protectorate. Today, Morocco ranks third among the producing countries and is by far the leading exporter.[4][4] Most of the tonnage goes to Europe (85%), but it is the countries of South America, Africa, and Asia whose capacity the O.C.P. keeps in mind when expanding its facilities, as phosphates are still three-quarters of the starting material for fertilizer production. However, their diverse industrial usability also suggests an increase in consumption in industrialized countries.

1.6 Mineralogy

The mineralogical and geochemical composition of Moroccan phosphates is characterized by the presence of francolite as the main phosphate mineral, along with associated gangue minerals. The article also mentions the potential of igneous phosphates in Morocco, particularly in alkaline and carbonatite complexes. These complexes have high P_2O_5 contents and the presence of strategic elements like rare earth elements.

The compositions of sedimentary rocks in Morocco, specifically the sedimentary phosphates, are as follows:

- The main phosphate mineral is carbonate fluorapatite (CFA), formerly known as francolite.
- Other phosphate minerals that may be present include dahllite (carbonate hydroxyapatite).
- Gangue minerals commonly associated with phosphate rocks in Morocco include calcite, dolomite, quartz, gypsum, and clay minerals such as smectite, illite, palygorskite, sepiolite, and kaolinite.
- Accessory minerals that can be found in Moroccan phosphates include glauconite, sulfides (mainly pyrite), iron oxides (e.g., hematite and goethite), and feldspar.

Moroccan sedimentary phosphates also contain minor and trace elements, including uranium (U), strontium (Sr), cadmium (Cd), and rare earth elements (REE). The concentrations of these elements can vary depending on the specific phosphate deposit.

The main gangue (cheap and useless) minerals found in Moroccan sedimentary phosphates are:

1. Calcite: This mineral is commonly associated with phosphate rocks and is often found as a non-phosphatic phase in the sedimentary deposits.
2. Dolomite: Another common gangue mineral found in Moroccan phosphates, dolomite is a calcium magnesium carbonate mineral that can occur alongside the phosphate minerals.
3. Quartz: Quartz is a common mineral found in many types of rocks, including phosphate rocks. It is often present as a non-phosphatic phase in the sedimentary deposits.
4. Gypsum: Gypsum is occasionally found as a gangue mineral in Moroccan phosphates. It is a hydrated calcium sulfate mineral.
5. Clay minerals: Various clay minerals, such as smectite, illite, palygorskite, sepiolite, and kaolinite, can be present as gangue minerals in Moroccan sedimentary phosphates. These clay minerals are often associated with the fine-grained matrix of the phosphate rocks[3].

Chapter 2

Literature Review

2.1 Environmental imapcts of dust on nature

As regulations on emissions, air quality, and pollution become more stringent, and as public awareness and sensitivity to the environmental impact of industries grow, dust generation in many heavy industries, such as mining, has come under increased scrutiny. [5]

Over the past few decades, there has been growing awareness and concern about the environmental effects of human activities, particularly in industries like mining. The mining industry's reputation has suffered, partly due to a history of environmental harm and a few well-known failures of metal mining tailings dams. As mining operations expand and affect larger areas, public concern about the industry's ability to manage and reduce its environmental impact has only intensified.

In response, many governments have introduced stricter legislative and regulatory requirements for the mining industry to protect ecosystems, ensure a safe and secure environment, and safeguard the well-being of people living near mine sites.

Phosphate mining activities are known to disrupt land, leading to increased concentrations of dissolved and suspended toxic metals and radioactive elements in the environment. These pollutants can significantly affect water quality, air pollution, and public health. The key environmental impacts of mining include soil erosion and the runoff of mine waste into surface waters, contamination from tailings impoundments and heap leaching, the formation of acid mine drainage, and the release of harmful contaminants through dewatering of acid mine water.[6]

Dust is a common issue across all types of mining, but in phosphate mining, the most significant air quality concerns stem from fluoride emissions and the release of radon gas.[6]

Regarding Phosphate, the environmental impacts of phosphate mining include the following:

1. **Water contamination**: The extraction and processes involved in increasing the phosphate concentration can lead to large quantities of powder, which can be transported by water and contaminate water bodies.[7, 8, 9] This can negatively impact aquatic ecosystems and the availability of clean water for human consumption. [10] In addition, acid mine drainage occurs after rainfall, resulting in the contamination of groundwater.[11]

2. **Soil contamination:** Phosphate mining can lead to soil contamination, especially when mine tailings are disposed of in unprotected areas, often near urban centers. These tailings can accumulate harmful trace metals like uranium (U), cadmium (Cd), chromium (Cr), molybdenum (Mo), vanadium (V), and thallium (Tl), which may exceed safe levels for soil. This poses a serious threat to both the environment and human health.[12]

3. **Air pollution**: Dust and emissions from mining operations, such as blasting,

crushing, and ore transport, can contribute to air pollution, affecting air quality and potentially causing respiratory problems for nearby communities. Dominant winds transport toxic dust and sulfur emissions from the mine wastes to nearby villages, polluting homes, cattle, and farmland. [13] Dust from solid phosphate waste can be deposited in the atmosphere, posing a threat to human health and the environment. Additionally, Saharan wind currents can contribute to the displacement of Saharan dust mixed with mine dust, further enhancing anthropogenic air pollution.[14]

4. **Soil degradation:** Phosphate mine wastes, such as waste rock and tailings, cover large areas and are subject to wind and water erosion, leading to soil degradation. Also, they contain small nutrient quantities and are contaminated by metals and fluoride, which can prevent good plant growth.[9, 15]

5. **Landscape degradation**: The piles of phosphate waste rock and tailing ponds spoil the landscape. [16, 17, 18]

6. **Fauna and flora impact:** Phosphate extraction can have negative effects on regional ecosystems, including the fauna and flora[19]. Land resources can be destroyed, leading to the loss of habitat for various species. Air and water pollution can also impact the health and survival of plants and animals in the area[19].

7. **Health risks:** Pollution from phosphate mining presents serious environmental and health risks to communities living near the mines.[20] The presence of potentially toxic metals (PTMs) in phosphate rocks, products, and waste materials can be harmful, posing health dangers to both adults and children.

2.2 Minerals Spectral Features in SWIR and TIR

Among the various spectral regions used for mineral analysis, the Short-Wave Infrared (SWIR) and Thermal Infrared (TIR) regions provide invaluable insights into mineral composition and characteristics. The SWIR region, spanning wavelengths from approximately 1,000 to 2,500 nanometers, is renowned for its ability to identify a wide range of minerals based on their distinct absorption features. These features are particularly useful in detecting hydroxyl-bearing minerals, carbonates, and sulfates, which exhibit characteristic absorption bands due to molecular vibrations and overtones.[21] Conversely, the TIR region, which covers wavelengths from around 8,000 to 12,000 nanometers, offers a different set of diagnostic capabilities. TIR spectral data are critical for analyzing the fundamental vibrations of molecules within minerals, providing valuable insights into their molecular structure and composition. The ability to distinguish and interpret these spectral features is essential for mineral exploration, environmental monitoring, and geological research. By leveraging SWIR and TIR data, researchers can gain deeper insights into mineralogical compositions, hydration states, and surface properties, which are crucial for a variety of applications including resource management, environmental

assessments, and planetary exploration. This chapter explores the spectral features of minerals in the SWIR and TIR regions, focusing on their unique signatures and the methodologies employed for their analysis. The mineralogical and geochemical

Region	Wavelength range	Minerals or groups of ions
VNIR	0.40-1.20 um	Fe, Mn and Ni oxide, hematite, goethite
SWIR	1.30-2.50 um	Hydrate, carbonate and sulfate
	1.47-1.82 um	Sulfates, such as alunite
	2.16-2.24 um	Minerals containing Al-OH groups of ions, such as kaolinite
	2.24-2.30 um	Minerals containing Fe-OH groups of ions, such as jarosite
	2.26-2.32 um	Carbonates, such as calcite, dolomite
	2.30-2.40 um	Minerals containing Mg-OH groups of ions, such as talc
TIR	8.00-14.0 um	Quartz, felspar, chalcedony, calcite, dolomite

Figure 2.1: Typical minerals of different wavelengths

profile of Moroccan phosphate deposits is dominated by carbonate fluorapatite (CFA), also referred to as francolite, which is the primary phosphate mineral. These phosphates are often found alongside various gangue minerals, such as calcite, dolomite, quartz, gypsum, and a range of clay minerals, including smectite, illite, palygorskite, sepiolite, and kaolinite. Additionally, minor accessory minerals like glauconite, pyrite, hematite, goethite, and feldspar can be found. Moroccan phosphates also contain trace amounts of elements like uranium (U), strontium (Sr), cadmium (Cd), and rare earth elements (REE), with their concentrations varying across different deposits[3].

Sedimentary phosphate rocks from Morocco, specifically those containing gangue minerals, are frequently associated with **calcite and dolomite**, both of which appear as non-phosphatic phases within the sedimentary layers. **Quartz** is another common non-phosphate mineral that occurs in these rocks. Occasionally, **gypsum** is also found as part of the gangue mineralogy. The presence of clay minerals such as **smectite, illite, palygorskite, sepiolite**, and **kaolinite** contributes to the fine-grained matrix of the phosphate deposits [3].

2.2.1 Apatite

Apatite, the most common phosphate mineral, shows distinct absorption features at 9160 nm and 9620 nm due to the asymmetric stretching of PO_4 .Clavier [22] discuss TIR vibrational modes for other phosphates, while Adler [23] notes that PO_4^{3-} can be replaced by AsO_4^{3-} and VO_4^{3-}, with major absorption features shifting to longer wavelengths as these substitutions occur.

In the Short-Wave Infrared (SWIR) range, fluorapatite generally has a flat spectrum [24]. However, the sample shows significant absorption bands at 2318 nm and 2499 nm, indicative of ferroan dolomite, and subtle absorption features around

$$\sim$$

1200 nm, likely due to REE^{3+}[25].

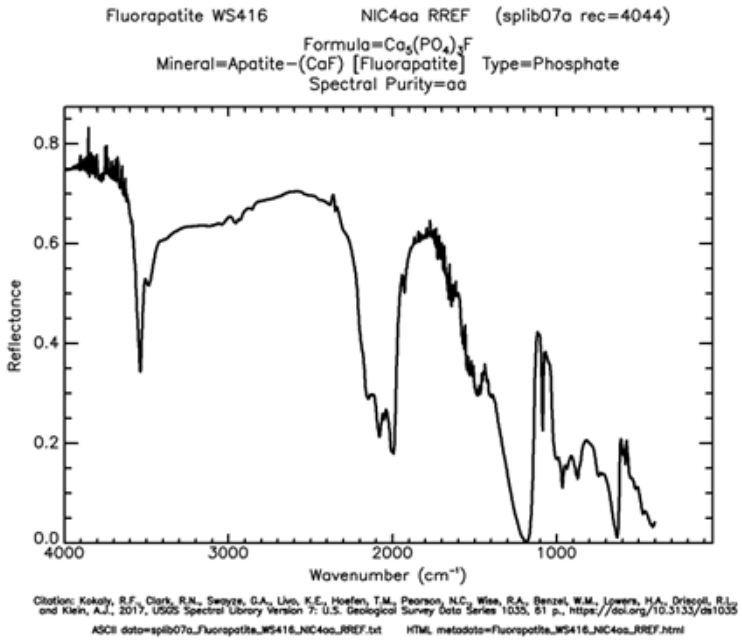

Figure 2.2: spectral signature of fluorapatite

Major infrared active features of carbonates lie in the thermal region around 6500 nm, 11 300 nm and 14 000 nm, with the latter two features being most useful for differentiating mineral species. A scatter diagram of the wavelength of the 14 000 nm feature vs that of the 11 300 nm feature, powerfully differentiates carbonates.

2.2.2 Quartz

Quartz lacks distinctive features in the visible to shortwave infrared wavelength range, as observed in WorldView-3 data and other airborne hyperspectral data used for mineral mapping at Rodalquilar [26, 27]. However, quartz exhibits clear diagnostic emission features in the thermal infrared region of the electromagnetic spectrum. Specifically, the emission spectrum of quartz shows prominent emissivity features between 8.2 m and 9.2 m, with a peak near 8.63 m [28].

Certain anisotropic minerals, like quartz, talc, and apatite, show a unique "M-shaped" feature in their reflectance spectra, where the primary reststrahlen bands split into two regions. For quartz, Spitzer and Kleinmann [29] explained this as a weak resonance lying close to a stronger one at longer wavelengths, creating this pattern. The weak resonance occurs at 8598 nm and the strong one at 9328 nm. Cudahy [30] used the depth of this feature to estimate quartz abundance in drill core spectra. This feature, called Resonance Strength Contrast (RSC), is also seen in other anisotropic minerals.

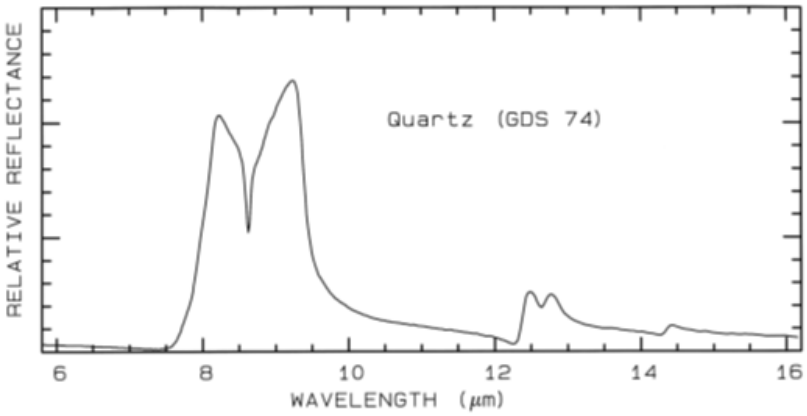

Figure 2.3: Relative reflectance of powdered quartz[24]

2.2.3 Illite

The illite reference spectrum shows a distinct absorption feature at 2.2 μm, distinguishing it from kaolinite in WorldView-3 multispectral imagery. Additionally, illite exhibits absorption features around 1410 nm, 1910 nm, and 2210 nm, which, while similar to those of illite-smectite and smectite, vary in intensity. The spectral distinction of illite can be determined by comparing the ratio of the minima of the H_2O absorption feature to the AlOH absorption feature. [31] In contrast, the goethite spectrum is characterized by a sharp drop in reflectance from 0.7 μm to shorter wavelengths and an absorption feature near 0.9 μm [24].

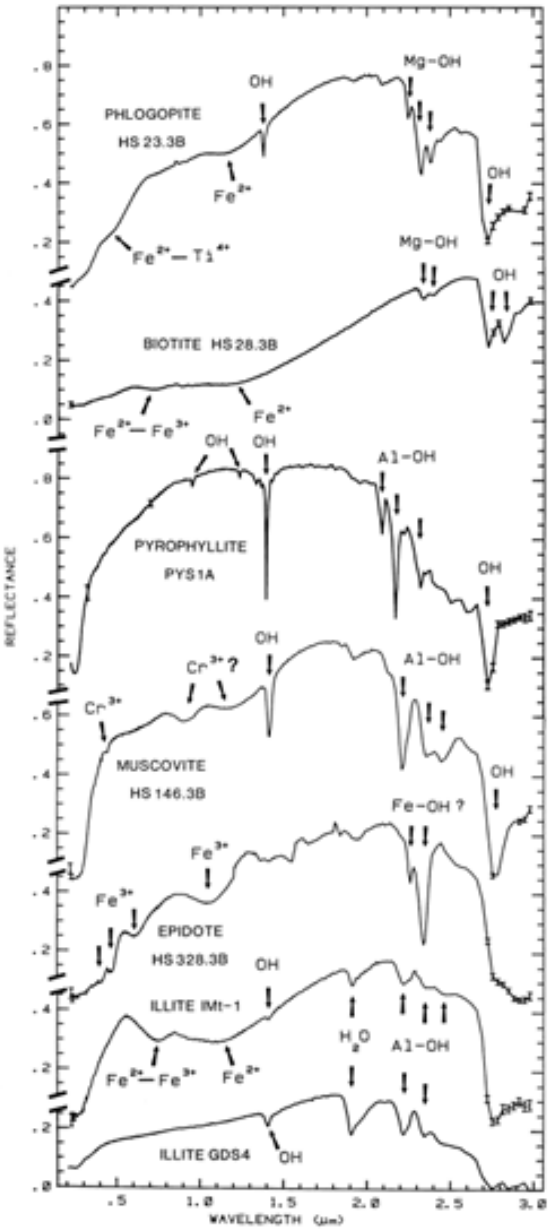

Figure 2.4: Reflectance spectra of phlogopite, biotite, pyrophyllite, muscovite, epidote, and illite

2.2.4 Calcite

The distinctive absorption characteristics of calcite are marked by strong vibrational absorption bands centered at 2.34 m (Zaini 2009).

However, the specific positions of these absorption bands in the thermal infrared

(TIR) exhibit notable variability depending on grain size fractions, typically ranging between 11.45–11.75 m and 14.00–13.92 m for pure calcite [32].

In the study of carbonate minerals' absorption features in the SWIR band, calcite shows significant variations in the precise position of its absorption bands as reported by various researchers. Huang and Kerr[33] observed that calcite has an absorption band centered at 3.92 µm. Hunt and Salisbury [34, 28] found calcite's absorption band at 2.35 µm. Gaffey [35]reported that calcite's absorption is centered around 2.33-2.34 µm, while Van der Meer [36] concluded that the absorption band is at 2.3465 µm. In the TIR region, Huang and Kerr [33] indicated a strong absorption band for calcite at 11.40 µm. Clark [24] suggested that the position of the absorption band can slightly shift due to different compositions of calcite. Reig et al.[37] used FTIR spectroscopy to determine specific absorption features of calcite at 875 cm^1 (11.43 µm) and 712 cm^1 (14.04 µm).

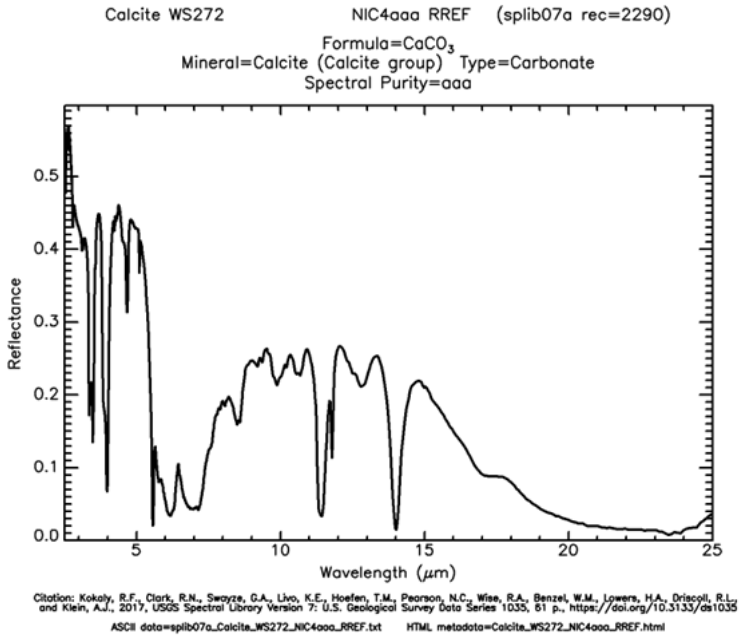

Figure 2.5: Calcite Spectral Signature

2.2.5 Dolomite

Dolomite exhibits key vibrational absorption features across various spectral regions. In the SWIR region, pure dolomite shows prominent absorption bands at 2.32138 m and 2.51485 m, while its diagnostic bands in the TIR region are found between 11.42–11.67 m and 13.65–13.44 m [32]. Multiple studies highlight variation in dolomite's absorption features. Early research by Huang and Kerr [33] identified a

band at 3.95 m, while Hunt and Salisbury [34, 28] reported a 2.33 m band, and [36] observed a band at 3.3039 m. Recent work by Huang et al. [7] confirmed a strong absorption band at 11.35 m in the TIR region. Clark [24] emphasized that dolomite's absorption band positions may shift due to compositional differences. Using FTIR spectroscopy, Reig et al. [37] pinpointed absorption features at 881 cm^1 (11.35 m) and 730 cm^1 (13.70 m).

The reflectance spectra of calcite-dolomite mixtures in the SWIR and TIR regions are influenced by the calcite-to-dolomite ratio, with absorption bands in the SWIR shifting from 2.32-2.34 m and 2.51-2.54 m as the mixture transitions from pure dolomite to pure calcite[32]. Further studies also report dolomite's SWIR absorption features. Gaffey [35] found a band at 2.31-2.32 m, and Clark [24] reiterated that compositional variations affect these bands' precise positions.

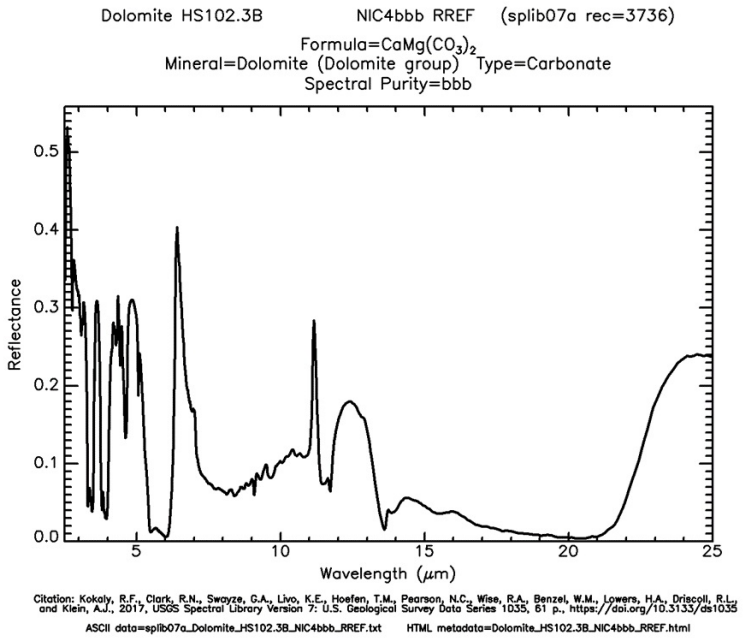

Figure 2.6: Spectral Signature of Dolomite

2.2.6 Gypsum

Gypsum exhibits distinct spectral absorption features in the VNIR and SWIR regions, primarily due to water molecules in its crystals. Key features include a minimum around 1.2 m, caused by H–O–H bending and the first overtone of O–H stretching, with additional absorption bands between 1.38 and 1.61 m linked to the first overtone of O–H stretch. Absorption near 1.75 m results from H–O–H bending, O–H stretching fundamentals, and low-frequency vibrational modes of

the crystal water. Another significant minimum occurs near 1.91 m, reflecting the combined effects of O–H stretching and H–O–H bending, while absorption around 2.21 m integrates O–H stretching and the first overtone of water [34, 38, 39].

Identifying gypsum using spectral absorption features can be challenging due to overlapping signals from soil components and atmospheric interference. Key absorption features for gypsum are found around 1.5 m, 1.75 m, and 2.2 m [34, 28]. However, the 1.5 m feature is often obscured by atmospheric water vapor, and the 2.2 m feature can be confused with clay minerals, complicating its use in remote sensing. The 1.75 m feature remains the most reliable for detecting gypsum, though interference from vegetation, plant residues, and pollutants like hydrocarbons—particularly those absorbing near 1.75 m—can complicate gypsum mapping[40, 24].

In the context of laboratory studies, USGS spectra highlight these gypsum absorption features, particularly in the water-vapor-affected regions. The 1.2 m feature results from a combination of H–O–H bending and O–H stretching, while the range between 1.38 and 1.61 m is dominated by the first overtone of O–H stretch[41, 34] . At 1.75 m, gypsum exhibits a strong signal from the combined effects of H–O–H bending and O–H stretching, along with vibrational modes of the crystal water. Around 1.91 m, the absorption is caused by O–H stretching and H–O–H bends, and at 2.21 m, it arises from the combination of O–H stretching and water overtone effects [38].

While these absorption features help in identifying gypsum, spectral discrimination is difficult when mixed with other materials like clay, starch, and hydrocarbons. Particularly, dry plant materials and industrial pollutants can overlap with gypsum's spectral range, limiting its detectability in remote sensing [42, 24].

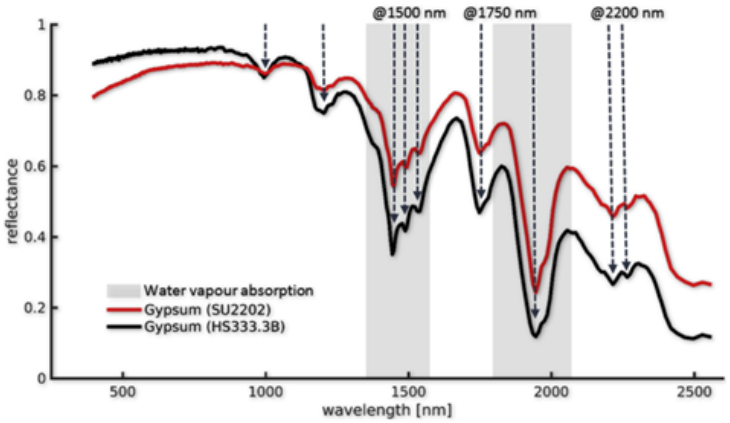

Figure 2.7: USGS laboratory spectra of gypsum, highlighting the key absorption wavelengths of the mineral as well as the regions affected by water vapor absorption.

2.2.7 Sepiolite

The third surface crust type (sample P68, Figure 2c) is primarily composed of calcite (CaCO3) at 45%, mixed with 16% sepiolite ($MgSiO(OH) \cdot 6HO$). The associated field spectrum reveals a strong absorption feature around 2340 µm, which is characteristic of both calcite and sepiolite [43]. Sepiolite's absorption features in the infrared spectrum, particularly near 2340 µm, are attributed to the vibrational modes of its silicate structure and hydroxyl groups[34, 28] . In the VNIR-SWIR range, sepiolite exhibits key absorption features near 1.38, 1.42, 1.91, 2.18, and 2.31 µm due to the presence of aluminum and magnesium [44]. Specifically, sepiolite is identified by a distinct doublet at 1388 and 1415 nm, caused by OH vibrations, a 1910 nm band from water vibrations, and a 2311 nm band from Mg-OH vibrations [45]. These features are essential for distinguishing sepiolite in spectral analyses.

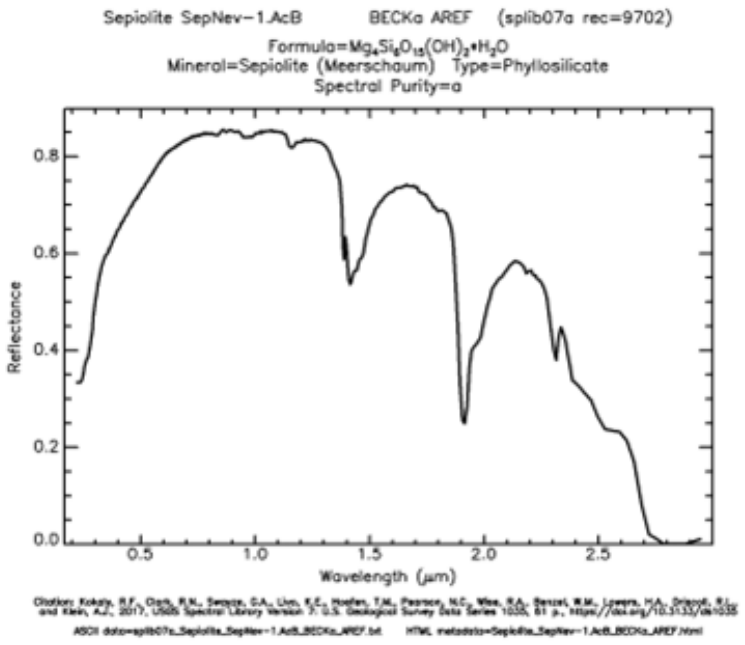

Figure 2.8: Spectral Signature of Sepiolite

2.2.8 Kaolinite

The spectral analysis of kaolinite reveals prominent absorption features at approximately 1400, 1900, 2200, and 2300 nm. Notably, the kaolinite reference spectrum displays a broad absorption band around 2200 nm, attributed to the characteristic Al-OH doublet absorption feature near 2170–2200 nm ([24]). The absorption regions from 1400 to 2450 nm are linked to the first harmonic of inner-surface (OH) stretching vibrations, as well as the combination of outer-surface (OH) stretching overtones and Al-OH bending modes ([46, 47]).

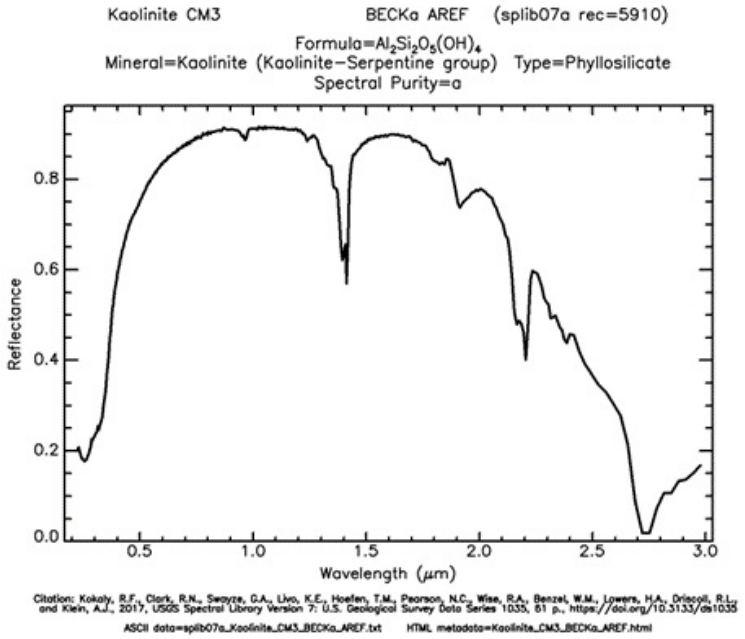

Figure 2.9: Spectral Signature of Kaolinite

To further illustrate the spectral characteristics discussed above, the key absorption features of the minerals analyzed in the Short-Wave Infrared (SWIR) and Thermal Infrared (TIR) regions are summarized in the following table. This table provides a concise comparison of the diagnostic wavelengths associated with each mineral, highlighting their distinctive spectral signatures. The table serves as a reference for understanding how specific absorption bands aid in the identification and differentiation of various minerals, thus reinforcing the importance of SWIR and TIR data in remote sensing applications.

Mineral	Wavelength (nm)	Type of feature	Phenomenon	Citation
Apatite	8400	—-	Christiansen Frequency	(Laukamp et al., 2021)
	9160	Trough	Reststrahlen (M Shaped)	
	9600	Peak		
Quartz	8630	Trough	Strong absorption band	(Clark, 1999a)
Calcite	2340	Trough	Strong absorption band	(Zaini, 2009)
	11450-11750, 14000-13920			
Dolomite	2321-2514	Trough	Strong absorption band	(Zaini, 2009; McCormick et al., 2021)
	11420-11670, 13650-13440			
Gypsum	1500	Trough	Strong absorption band	(Khan et al., 2020)
	1750			
	2200			
Sepiolite	2340	Trough	Strong absorption band	(Milewski, Chabrillat, and Behling, 2017)

The table of spectral features provides a detailed overview of the key absorption wavelengths associated with various minerals. Complementing this summary, the linear diagram visually depicts the specific wavelengths where these absorption features occur, allowing for a clear comparison between different minerals. This diagram highlights not only the wavelengths where features are expected but also illustrates how certain minerals exhibit features at similar wavelengths or have closely spaced absorption bands. This dual representation enhances our understanding of mineral differentiation and the potential for overlapping spectral signatures in remote sensing analyses.

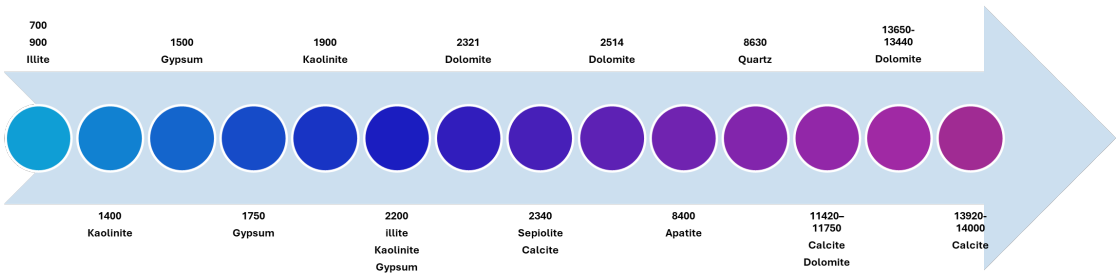

Figure 2.10: Mineral Distribution based on their features Along the Electromagnetic Spectrum

Chapter 3

Methodology

Sensor and Satellite Specifications

In this study, three different satellite sensors, including EMIT, ECOSTRESS, and Landsat 9, are utilized to monitor and analyze the Earth's surface characteristics. Each of these sensors has unique capabilities in terms of spectral range, spatial resolution, and applications, which provide comprehensive insights into mineral composition, plant water use, and land cover changes. The following table summarizes key features of these instruments.

Feature	EMIT (Earth Surface Mineral Dust Source Investigation)	ECOSTRESS (ECOsystem Spaceborne Thermal Radiometer Experiment on Space Station)	Landsat 9
Primary Objective	Determine mineral composition of dust aerosols	Measure plant water use by monitoring temperature	Land cover/land use change, natural resource management
Launch Date	2022	Jul-18	Sep-27, 2021
Platform	International Space Station (ISS)	International Space Station (ISS)	Sun-synchronous orbit
Number of Bands	285	5	11
Spectral Range	Visible to shortwave infrared (400-2500 nm)	Thermal infrared (8000-12000 nm)	Visible to thermal infrared (443-1373 nm, 10600-12510 nm)
Spectral Resolution	∼7.5 nm	-	-
Spatial Resolution	60 meters	70 meters	30 meters (visible, NIR, SWIR); 100 meters (thermal)
Temporal Resolution	Varies (dependent on ISS orbit)	Varies (dependent on ISS orbit)	16 days
Applications	Climate modeling, dust source identification, air quality	Agriculture, water management, heat stress, volcanic activity	Land cover mapping, agriculture, forestry, water resources
Principal Investigator	Robert Green, NASA Jet Propulsion Laboratory	Simon Hook, NASA Jet Propulsion Laboratory	Jeff Masek, NASA Goddard Space Flight Center

Table 3.1: A comparison of mission goals and specifications of EMIT and ECOSTRESS sensors and LANDSAT 9[48, 49, 50]

3.1 Normalized Difference Vegetation Index

Numerous vegetation indices derived from remote sensing have been developed and utilized based on the idea that specific mathematical combinations of spectral

bands captured from remote sensing can provide insights into various aspects of vegetation, such as its structure, health, photosynthetic activity, leaf density, distribution, water content, mineral deficiencies, and signs of stress or parasitic infestation[7].

The way leaves are structured, specifically for photosynthesis, influences how plants interact with sunlight. Inside the leaves, two main processes take place: absorption and scattering of light. Plant pigments like chlorophyll and carotenoids, along with water, absorb certain wavelengths of light. Scattering happens due to the complex internal structure of leaves, which consists of air spaces and irregularly shaped, water-filled cells. This scattering is caused by the differences in the refractive index between the air and water-filled cells, as well as internal reflections from the irregular cell shapes. Green leaves absorb light strongly in the blue and red regions of the spectrum but less in the green region, which is why they appear green. Beyond the visible spectrum, from 700 nm to over 1300 nm, there is no absorption, leading to higher reflectance levels from green vegetation. This lack of absorption is due to the strong absorption of light by liquid water in this range.[51] The normalized difference vegetation index (NDVI) is calculated by taking the difference between the near-infrared (NIR) and red (R) bands and then dividing that difference by the sum of the two bands [52]:

$$\mathrm{NDVI} = \frac{R_{\mathrm{NIR}} - R_{\mathrm{R}}}{R_{\mathrm{NIR}} + R_{\mathrm{R}}} \tag{3.1}$$

In the NDVI calculation, NIR represents the reflectance in the near-infrared band, while RED denotes the reflectance in the visible red band. The NDVI algorithm leverages the fact that healthy green vegetation reflects more NIR light and less visible light, whereas sparse or less green vegetation reflects more visible light and less NIR. By combining these reflectance properties into a ratio, NDVI serves as an index of photosynthetic activity. The values range from -1 to +1, with positive values indicating vegetated areas. Higher NDVI values correspond to greater chlorophyll content. NDVI is widely used to analyze and interpret various phenological metrics, which describe the timing of plant life-cycle events and their responses to seasonal and annual climate variations.

The duration of photosynthetic activity, as identified by NDVI, can be used to determine the length of the growing season. The peak NDVI value corresponds to the period of maximum photosynthesis. Seasonally integrated NDVI reflects the overall photosynthetic activity throughout the growing season, while changes in NDVI can indicate the rate at which photosynthesis is increasing or decreasing. These metrics are influenced by various vegetation characteristics, with one of the most significant being the leaf area index (LAI), which measures the leaf area per unit of ground area [53].

3.1.1 Characterizing the Vegetation using NDVI

The absolute value of the NDVI is a valuable resource for quickly detecting problem areas within a farm or field. This simple index ranges from negative one to positive one, providing a clear snapshot of crop health irrespective of the plant species. By analyzing the NDVI, farmers can efficiently identify regions experiencing stress or suboptimal growth conditions.

3.1.2 NDVI Stack Photo Interpretation using the 'Build Layer Stack' Tool

Stacking NDVI layers combines multiple NDVI images taken at different times into a single multi-temporal file, where each layer represents NDVI values for specific time periods, such as monthly data over a year. This technique enhances our understanding of vegetation health and facilitates several important applications.

Temporal Analysis allows us to observe trends in vegetation health by tracking NDVI changes over time, revealing seasonal growth patterns. Change Detection helps identify shifts in vegetation cover and health, indicating phenomena like deforestation or land use changes. Anomaly Detection enables the identification of disturbances, such as natural disasters or human activities, by spotting sudden NDVI value changes.

Examining NDVI across months reveals Seasonal Patterns in growth, useful for agricultural planning and understanding climate impacts. Finally, the insights from stacked NDVI layers serve as valuable Decision Support tools across sectors like agriculture and environmental management, informing practices such as crop scheduling and forest conservation.

3.1.3 Vegetation Charachterization Procedure

The steps of characterization of flora in the area are as follows:

- Image Acquisition: Landsat images were acquired for five nonconsecutive months in 2023 to capture seasonal variations in the study area.
- NDVI Generation: NDVI (Normalized Difference Vegetation Index) images were generated for each selected month to assess vegetation health.
- Layer Stacking: The five NDVI images were combined using a layer stacking technique to enable the visualization of temporal changes or the comparison of features through false color composition.
- False Color Composition: The resulting composite images were classified by assigning red, green, and blue colors to represent different false color classes.
- Interpretation: Vegetation types were interpreted by analyzing the NDVI values corresponding to each false color class, providing insights into the distribution and health of vegetation.
- Comparative Analysis: A comparative analysis was performed with relevant literature to validate the findings and enhance the understanding of the vegetation in the region.

Vegetation Index	Formula	Details	Citation
Simple Ratio	$\frac{R_{\mathrm{NIR}}}{R_{\mathrm{R}}}$	Measures green vegetation cover, depends on sensor	Person 1972
Normalized Difference Vegetation Index	$\frac{R_{\mathrm{NIR}}-R_{\mathrm{R}}}{R_{\mathrm{NIR}}+R_{\mathrm{R}}}$	Widely used for green vegetation cover	Rouse et al. 1974; Tucker 1979
Enhanced Vegetation Index	$2.5 \times \frac{(R_{\mathrm{NIR}}-R_{\mathrm{RED}})}{R_{\mathrm{NIR}}+6R_{\mathrm{RED}}-7R_{\mathrm{BLUE}}+1}$	Enhances sensitivity to dense vegetation, reduces atmospheric effects	Huete et al. 2002
Perpendicular Vegetation Index	$\frac{R_{\mathrm{NIR}}-aR_{\mathrm{RED}}-b}{\sqrt{1+a^2}}$	Measures distance from soil line in spectral space	Richardson and Wiegand 1977
Soil Adjusted Vegetation Index	$\frac{(R_{\mathrm{NIR}}-R_{\mathrm{RED}})}{R_{\mathrm{NIR}}+R_{\mathrm{RED}}+L} \times (1+L)$	Minimizes soil brightness in areas with low vegetation cover	Huete 1988
Modified Soil Adjusted Vegetation Index	$\frac{2R_{\mathrm{NIR}}+1-\sqrt{(2R_{\mathrm{NIR}}+1)^2-8(R_{\mathrm{NIR}}-R_{\mathrm{R}})}}{2}$	Reduces soil brightness in sparse vegetation areas	Qi et al. 1994
Transformed Soil Adjusted Vegetation Index	$\frac{aR_{\mathrm{NIR}}-bR_{\mathrm{RED}}-b}{R_{\mathrm{RED}}+a\sqrt{R_{\mathrm{NIR}}-b}+0.8(1+a^2)}$	Reduces soil background effects, useful in sparse vegetation	Baret and Guyot 1991
Soil and Atmospherically Resistant Vegetation Index	$\frac{R_{\mathrm{NIR}}-\sqrt{R_{\mathrm{RED}}-L(R_{\mathrm{BLUE}}-R_{\mathrm{RED}})}}{R_{\mathrm{NIR}}+\sqrt{R_{\mathrm{RED}}-L(R_{\mathrm{BLUE}}-R_{\mathrm{RED}})}+L}$	Minimizes effects of soil and atmospheric conditions	Kaufman and Tanre 1992

Table 3.2: Vegetation indices and their formulas[54, 52, 51, 55, 56, 57, 58, 59, 60]

NDVI	INTERPRETATION
<0	Water
0.0 - 0.1	Bare soil/Urban area
0.1 - 0.2	Almost absent canopy cover
0.2 - 0.3	Very low canopy cover
0.3 - 0.4	Low canopy cover, low vigour or very low canopy cover, high vigour
0.4 - 0.5	Mid-low canopy cover, low vigour or low canopy cover, high vigour
0.5 - 0.6	Average canopy cover, low vigour or mid-low canopy cover, high vigour
0.6 - 0.7	Mid-high canopy cover, low vigour or average canopy cover, high vigour
0.7 - 0.8	High canopy cover, high vigour
0.8 - 0.9	Very high canopy cover, very high vigour
0.9 - 1.0	Total canopy cover, very high vigour

Table 3.3: NDVI value interpretation

- Vegetation Characterization: The specific vegetation types present in the study area were characterized, offering a comprehensive overview of the ecological landscape.

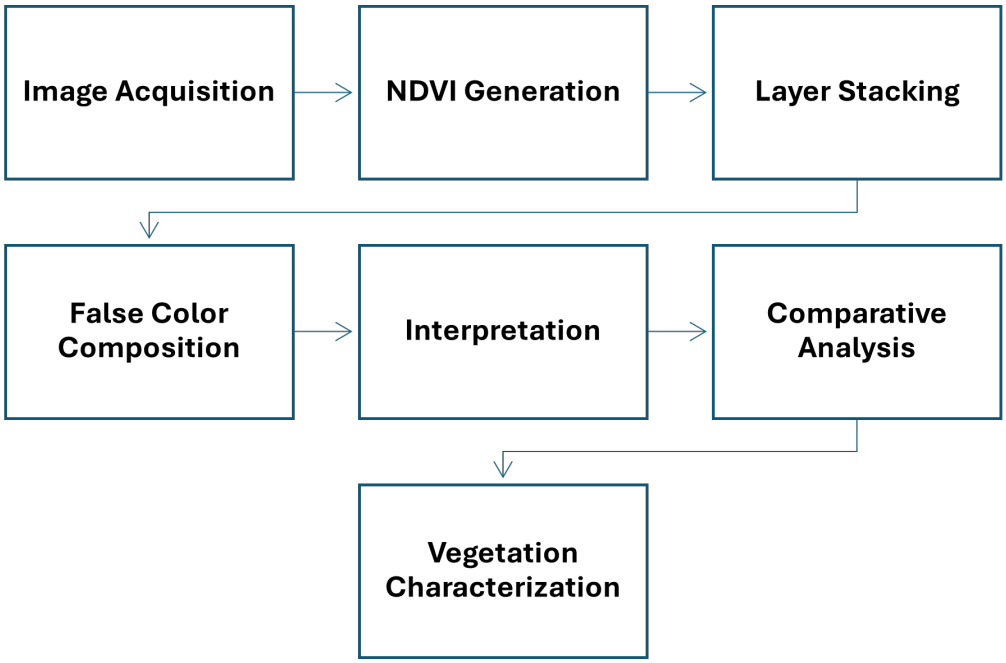

Figure 3.1: The procedure for characterization of the vegetation in the area based on Layerstacked NDVI images during a year

3.2 Mineral Characterization

In the field of mineral characterization, accurate and efficient data processing is essential for extracting meaningful information from remote sensing imagery. This process involves preparing images acquired from advanced satellite and airborne sensors, ensuring they are suitable for detailed analysis. Proper image preparation enhances the results' reliability and facilitates the comparison of spectral signatures with known mineral databases. The following sections outline the specific steps taken in preparing ECOSTRESS and EMIT images, setting the stage for the subsequent hyperspectral analysis.

To be able to study the spectrum of the ore and gangue minerals in the Youssoufia region, data from different spectrometers such as Perkin, Beckman and IGCP 264 are considered. To study the spectrum of ore and gangue minerals in the Youssoufia region, data from various spectrometers, including Perkin, Beckman, and IGCP 264, are utilized. These spectrometers provide a comprehensive understanding of the mineral compositions by covering different parts of the electromagnetic spectrum. The short-wave infrared (SWIR) range, typically spanning from 0.9 to 2.5 micrometers (µm), is crucial for this analysis. However, this range is incompatible with the Nicolet spectrometer library, which is designed for mineral and rock sample spectra ranging from 2.5 to 15 µm. The Nicolet spectrometer's range makes it particularly useful for applications like ECOSTRESS, which require data within this specific spectral range. ECOSTRESS (Ecosystem Spaceborne Thermal Radiometer Experiment on Space Station) relies on accurate thermal infrared measurements, which align well with Nicolet's capabilities.

Understanding Bad Bands

Bad bands refer to specific spectral bands within a remote sensing dataset that are corrupted or contain insufficient information for analysis. These bands can be caused by various factors such as sensor anomalies, atmospheric interference, or data processing errors. While the term "bad bands" can be applied to any sensor type, it's particularly relevant to hyperspectral sensors due to their large number of bands. Emissive sensors, which measure emitted energy rather than reflected sunlight, are also susceptible to bad bands.

Band 128-142 (1320 nm - 1439 nm)

This wavelength range is notably impacted by strong absorption features caused by water vapor and carbon dioxide in the atmosphere. The presence of these gases results in considerable attenuation of the signal from the Earth's surface, leading to unreliable data in this range. Consequently, this spectral interval is often excluded from analysis to maintain data integrity.

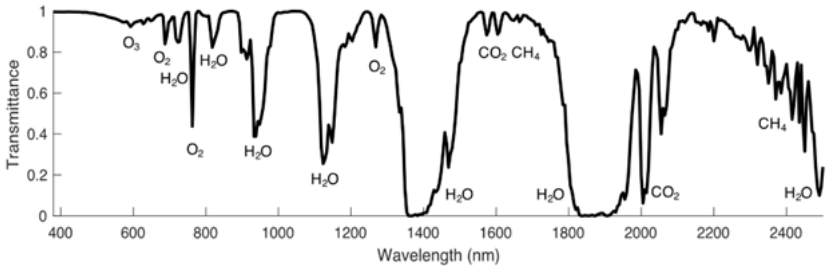

Figure 3.2: Atmospheric gas absorption by wavelength across the EMIT spectral interval. Certain spectral bands are missing due to atmospheric interference. Specifically, the intervals from band 127-143 (1320 nm - 1439 nm) and band 188-213 (1766 nm - 1967 nm) are affected by significant atmospheric absorption.[61]

Band 188-213 (1766 nm - 1967 nm)

Similarly, this range is subject to significant absorption by atmospheric water vapor and molecular overtones. The attenuation caused by these gases renders the data from this range less useful for accurate surface measurements. As a result, this interval is frequently omitted or corrected to account for atmospheric interference.

3.2.1 Image Preparation

To effectively analyze mineral characteristics, the images from ECOSTRESS and EMIT must undergo a series of preparation steps. These steps ensure that the data is accurately preprocessed and formatted, enabling reliable comparisons and interpretations in the subsequent analysis. Below are the detailed procedures for preparing the ECOSTRESS and EMIT images.

ECOSTRESS Image Preparation

1. Choose the level of preprocessing: all the images acquired for this work are of level 2 of preprocessing, which denotes that they already include—radiometric calibration, geometric correction, atmospheric correction, cloud masking, and land surface temperature retrieval.

2. Download the image of the driest month of the year based on NDVI analysis from the Earth Data Search portal of NASA[49].

3. Conversion of the ECOSTRESS Swath data to GeoTIFF: The script from NASA's GitHub repository[62] is used to transform ECOSTRESS swath data from HDF5 format into GeoTIFF, which is suitable for GIS and remote sensing applications. It georeferences the data based on user-specified projections,

resamples it onto a grid, and facilitates batch processing for multiple files. The script also manages metadata such as scale factors and fill values and provides options for selecting data layers and projections, making it crucial for effective and precise geospatial data handling.

4. Stack the emissivity bands into one image.

5. Clip the image to the area of interest (AOI).

6. Fix the header file by adding FWHM and wavelength information.

7. To convert the emissivity bands from ECOSTRESS data into reflectance bands, we use the relationship between emissivity and reflectance. According to Kirchhoff's law of thermal radiation:

$$R = 1 - \varepsilon$$

Where:

- R is the reflectance,
- ε is the emissivity.

This equation indicates that reflectance is equal to 1 minus emissivity. Since ECOSTRESS data is acquired in emissivity format, we can convert it to reflectance by applying this formula. This conversion makes the data comparable to spectral libraries, which are typically based on reflectance values for mineral identification.

EMIT Image Preparation

1. Choose the level of preprocessing: all the images acquired for this work are of level 2A, in which surface reflectance is extracted by screening clouds and correcting for atmospheric effects.

2. Download the NDVI image of the driest month of the year, with the analysis focusing on vegetation patterns in the Youssouffia region. To enhance the accuracy of mineral detection, a night image was used, reducing the impact of temperature on the emissivity data. By discarding the temperature component and retaining only the emissivity part, the analysis ensures a clearer focus on the spectral characteristics of the minerals, crucial for distinguishing ore and host minerals in phosphate mining.

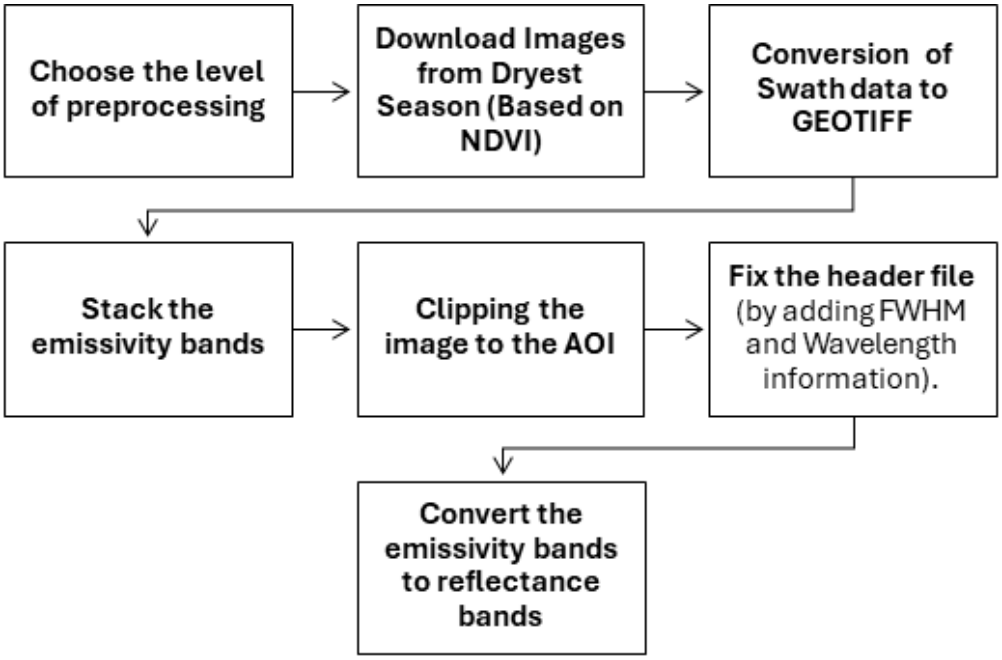

Figure 3.3: The steps of preparing data of ECOSTRESS to be processed in ENVI

3. Reproject in ENVI: This step converts EMIT's Geographic Lookup Table (GLT) to a standard Geographic Lat/Lon WGS-84 projection.

4. Clip the image to the area of interest (AOI).

3.2.2 Hyperspectral Analysis Procedure

The hyperspectral analysis procedure is a systematic approach to identifying and characterizing minerals using remote sensing data. This process involves multiple steps, from literature review and feature identification to advanced data processing techniques. Each step plays a crucial role in ensuring accurate mineral identification, facilitating comparisons with spectral libraries, and ultimately enhancing the reliability of the findings.

1. Literature Review and Mineral Identification: Researching and identifying existing minerals in the study area.

2. Feature Identification: Study the literature to determine important spectral features of the minerals found in the area.

3. Create a diagram for mineral identification based on their features along the electromagnetic spectrum to depict possible interferences and similarities in the detection of minerals.

4. Library Sample Selection: Choose mineral samples from ENVI's spectral library. It should be noted that the range of the spectrometer chosen from the library (Nicolet, Beckman, etc.) should match the characteristics of the observation device (ECOSTRESS or EMIT) and also cover the features of interest.

5. Spectral Library Resampling: Resample the ENVI spectral library to modify it so that its spectral data matches the spectral resolution or wavelength sampling intervals of the study's sensor.

6. Checking for Bad Bands: Some specific wavelengths or parts of the spectrum may not be reliable or may contain significant noise. Therefore, they should be discarded to avoid distorting the results. Typical factors leading to bad bands include atmospheric absorption (such as water vapor absorptions around 1.4 µm and 1.9 µm in the SWIR range), sensor limitations, saturation (high reflections of clouds or snow), and thermal noise (due to temperature fluctuations in the sensor or environment).

7. Formulating Spectral Features: Develop mathematical formulas to emphasize the specific spectral features or signatures of the minerals being studied.

8. Reference Band Math Table: Create a table that records the band math operations (like simple band ratios or ratios that consider heads and shoulders of a feature) performed on the spectral library samples, establishing a reference range for each mineral.

9. Band Math on Image Data: Apply the same band math formulas to the actual image data from the acquisition device to extract relevant spectral information.

10. Range Comparison: Compare the results obtained from the reference band math table with the band math applied to the image.

    (a) If there is no overlap between the two, it indicates that the minerals in the image differ from those in the spectral library.

    (b) If there is an overlap between the ranges of band math reference tables and the image band math values, they are highlighted using a raster color slice, and a shapefile of possible distributions of the study mineral is created.

    Note:

    The following steps for verifying the hyperspectral analysis results were not conducted in this study. Although ground truthing, field validation, and comparison with existing geological maps are critical for ensuring the accuracy and reliability of hyperspectral analysis, due to limitations in time, resources, or sample availability, these steps were not implemented.

11. Verifying the Results: To ensure the accuracy and reliability of hyperspectral analysis, the following steps can be taken:

    (a) Ground Truthing: Collect and analyze physical samples from the study area using techniques such as X-ray diffraction (XRD) or scanning electron microscopy (SEM). The mineral composition obtained can then be compared with the distribution identified in the hyperspectral analysis for consistency.

    (b) Field Validation: If physical samples are unavailable, conduct field observations using a portable spectrometer to measure the spectral reflectance of minerals directly. These measurements should align with the spectral features detected through remote sensing.

    (c) Comparison with Existing Geological Maps: Compare the mineral distribution results with established geological or mineralogical maps of the area to determine if the detected mineral patterns are consistent with known geological formations.

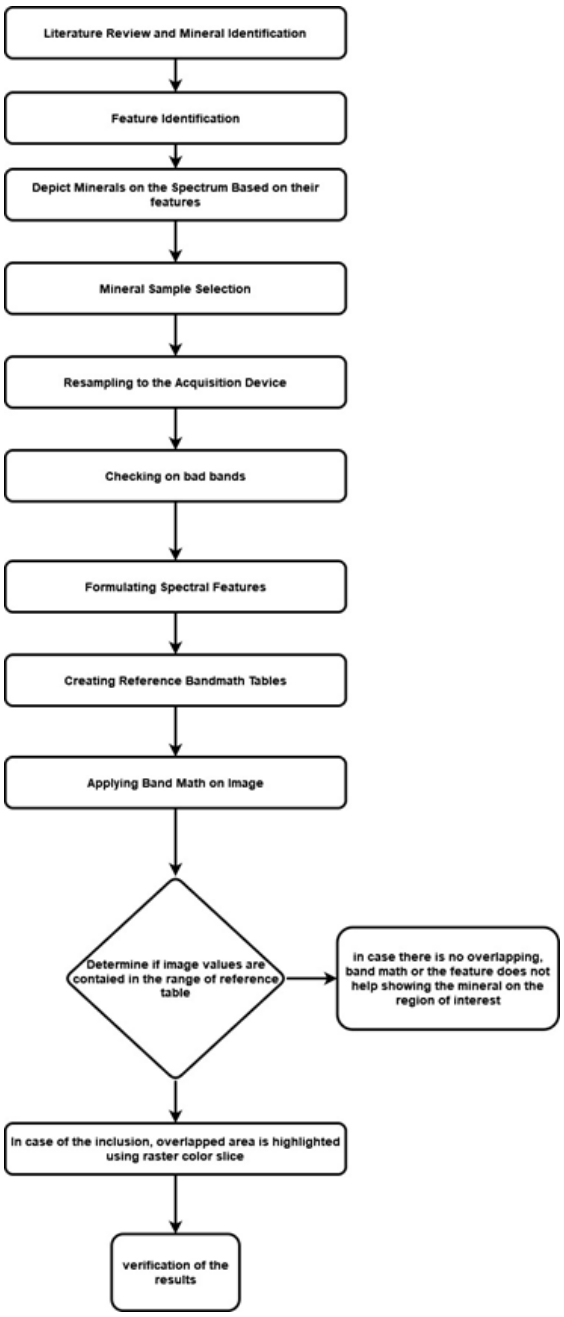

Figure 3.4: The steps adapted to perform spectral analysis for minerals and charachterization of the area of interest based on the mineral features

Chapter 4

Results and Discussion

4.1 Vegetation Charachterization

4.1.1 Vegetation's Seasonal Changes: A Simple 5 Months Comparison

A color-sliced raster image illustrating NDVI values for five months of 2023 in Youssoufia reveals several key environmental and ecological trends. The Normalized Difference Vegetation Index (NDVI) is a critical metric for assessing vegetation health and density, and the image provides a clear visual representation of how these factors vary across different times of the year in Youssoufia. One of the primary observations from the image is the minimal surface water coverage throughout the region, which aligns with the area's typical arid or semi-arid hydrological regime. This scarcity of surface water is a significant factor influencing the overall vegetation patterns and ecosystem dynamics in the area. The vegetation cover in Youssoufia peaks in March, as indicated by the NDVI values, though it is primarily dominated by low-canopy species. This suggests that the region may experience a brief period of increased plant growth during the late winter to early spring, likely due to seasonal rains that temporarily boost soil moisture levels. However, the predominance of low-canopy vegetation points to a landscape that supports more drought-resistant or hardy species, which are adapted to the generally dry conditions and limited water availability. The timing of this peak also reflects the broader climatic patterns of the region, where the cooler and wetter months contribute to a short-lived but noticeable increase in vegetation. Conversely, the image shows that September exhibits the lowest vegetation density of the five months observed. This decline in vegetation cover could be attributed to the onset of the dry season, where higher temperatures and reduced rainfall likely lead to increased evapotranspiration and soil moisture deficits. As a result, many plants may enter a dormant state or experience stress, leading to reduced NDVI values. This pattern underscores the seasonal variability in vegetation health and the challenges that the region's flora face in maintaining growth during periods of environmental stress. Notably, the image also highlights small portions of the study area that support high-canopy vegetation, particularly during November, March, and May. These areas of denser, taller vegetation may indicate the presence of microenvironments where conditions are more favorable for growth, such as areas with slightly higher moisture retention or less human disturbance. The presence of high-canopy vegetation during these months suggests that, while the region is predominantly low-canopy, there are pockets of more robust plant life that could play a critical role in local biodiversity and ecosystem stability. Overall, the NDVI analysis provides valuable insights into the seasonal and spatial dynamics of vegetation in Youssoufia, revealing the complex interplay between climate, hydrology, and plant life in this region.

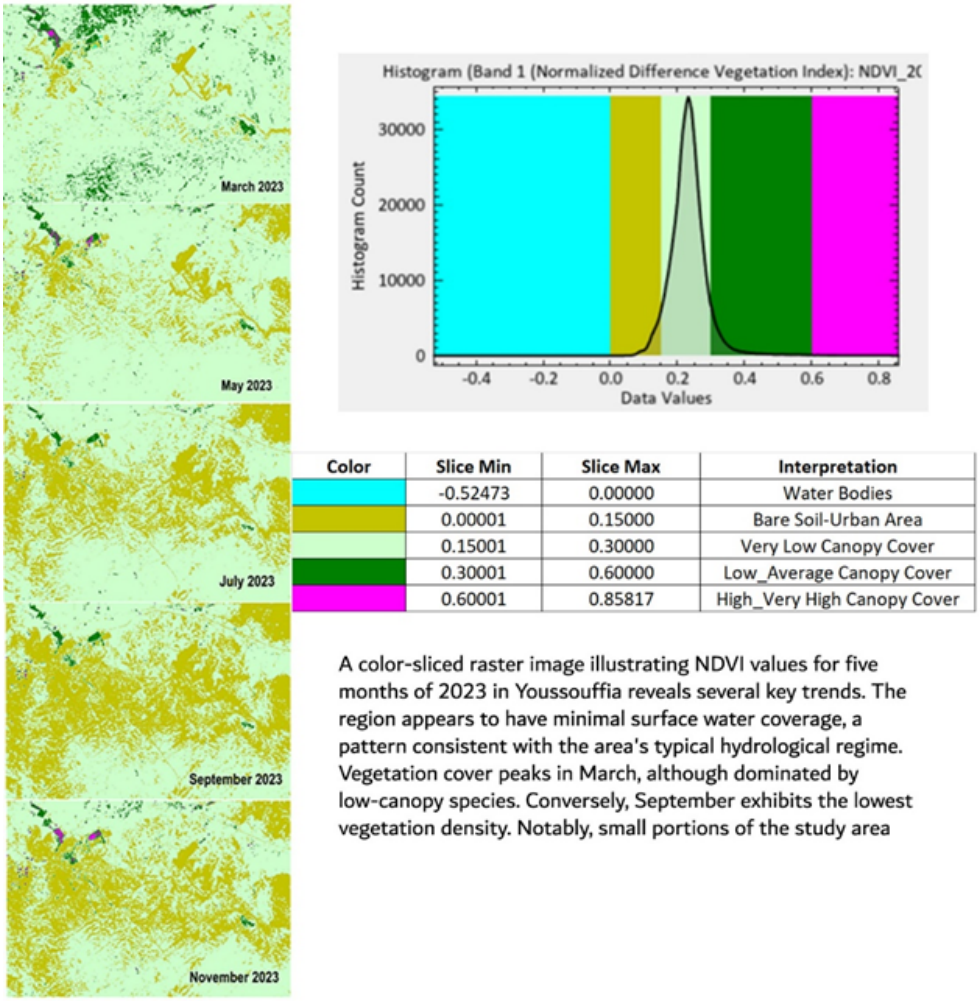

Figure 4.1: Vegetation's Seasonal Changes: NDVI analysis for Youssoufia in 2023 shows peak vegetation in March and lowest density in September. High-canopy areas are visible in November, March, and May.

4.1.2 Vegetation's Seasonal Changes: Characterizing the flora based on the seasonal change

The Youssoufia Mine study involved the preparation of NDVI (Normalized Difference Vegetation Index) images for each of five specific months, enabling a detailed analysis of vegetation health or type over time. NDVI is a crucial remote sensing index used to assess vegetation by measuring the difference between near-infrared (which vegetation strongly reflects) and red light (which vegetation absorbs). For this study, Grey style NDVI images were first generated for March, May, July, September, and November of 2023. These NDVI images were then combined using

the "build layer stack" tool, a process that aligns the data layers into a single multi-band image. The reordering of the months in this layer stack allowed for the creation of a new NDVI composite specifically tailored for analyzing the Area of Interest (AOI) at the Youssoufia Mine.

In the newly created NDVI stack, the bands were organized in a chronological sequence to reflect the progression of the months: March was assigned to band 1, May to band 2, July to band 3, September to band 4, and November to band 5. This configuration is particularly useful for temporal analysis because it retains the chronological order, making it easier to observe and compare changes in vegetation across different times of the year. By using this stacking method, researchers can track seasonal variations and trends in vegetation health, which are often influenced by factors such as climate, mining activities, and other environmental changes.

The choice of months for this study was strategic, capturing the transitions between different seasons—spring, summer, and autumn. These seasonal changes are significant in regions like Youssoufia, where vegetation may respond differently to climatic conditions throughout the year. For example, March and May images might highlight the initial growth phases in spring, while July could show peak summer conditions. September and November images would then reveal the transition into autumn, capturing the potential decline in vegetation as temperatures drop and rainfall patterns change. This detailed temporal information is crucial for understanding the broader environmental impacts on the mine's surrounding areas.

Ultimately, this approach provides a powerful tool for environmental monitoring and management. By analyzing the NDVI data across multiple months, stakeholders can identify areas of vegetation stress, recovery, or decline within the Youssoufia Mine AOI. Such insights can inform better land management practices, including the planning of rehabilitation efforts, the assessment of mining impacts, and the development of strategies to mitigate adverse environmental effects. The use of NDVI stacking thus represents a valuable method for sustaining the ecological balance in mining regions, ensuring that economic activities are balanced with environmental conservation.

False Color Composite

Using false colors to interpret the Temporal NDVI, March, July and November are assigned to RGB as the first sequence of months to be analyzed.

To determine the types of vegetation in an area using NDVI color composites, we analyze the variations in the color patterns over multiple temporal data sets. Each color in the composite represents vegetation activity for specific months, with different hues indicating growth, decline, or stability of vegetation. NDVI values reflect vegetation health, where high values suggest dense, healthy vegetation, while low values indicate sparse or stressed vegetation. For instance, black or grey areas

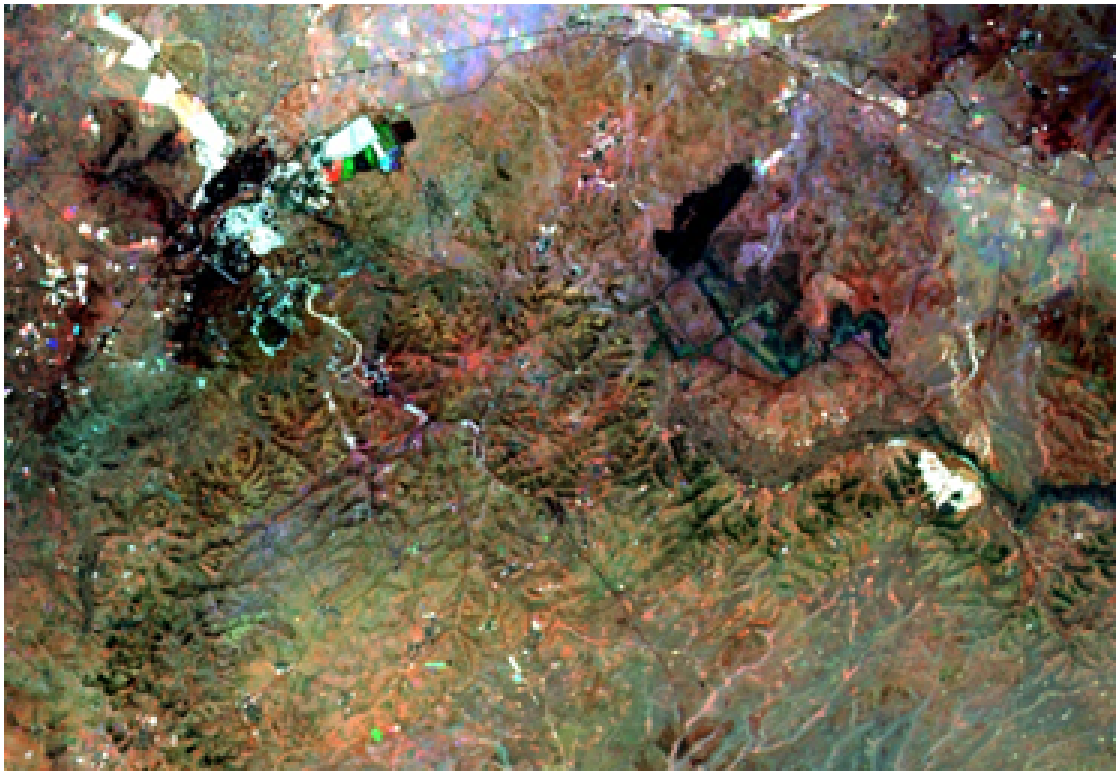

Figure 4.2: Enter CapNDVI of three months of November, March and July after being stacked in 3 layers and assigned to colors of blue, red and green respectively.tion

typically correspond to urban or barren lands with minimal vegetation change, while red, green, or blue shades indicate seasonal variations in plant growth.

The NDVI color composite helps identify the most active growth periods for different vegetation types. For example, vegetation showing a red hue may peak in March, indicating winter cereals or legumes, while green might signify peak growth in May, suggesting crops like barley or wheat. By interpreting these temporal patterns, we can infer the presence of various crops, shrubs, or managed green spaces.

Grey Tones (March-May-July)

In multi-temporal color composites, grey tones (ranging from black to white) indicate areas that have remained unchanged over time, reflecting stability. Key observations include:

- **Dark Urban Areas**: These regions show consistently low NDVI values,

indicating minimal vegetation across the months.

- **Water Bodies**: Dark areas like rivers also exhibit low NDVI due to a lack of significant vegetation.
- **White Areas**: High and stable NDVI values across all acquisition dates suggest healthy vegetation, often attributed to:
  - **Irrigated Crops**: Such as citrus, olive, or date palms that maintain greenness year-round.
  - **Perennial Vegetation**: Mediterranean shrubs like rosemary and argan trees that thrive in arid conditions.
  - **Managed Green Spaces**: Parks and lawns with consistent irrigation, contributing to year-round greenery.
  - **Evergreen Forests**: Eucalyptus or pine plantations help maintain stable NDVI values.

Red (March)

Red indicates areas with a peak in NDVI during March, suggesting the presence of winter cereals or legumes. These plants typically grow in cooler months and are harvested in spring, leading to lower NDVI values afterward.

Green (July)

Green represents areas where NDVI values increase in July. This pattern is indicative of crops that are most active in summer, such as:

- **Cereal Crops**: Barley and wheat, often sown in autumn and harvested in late spring or early summer.
- **Vegetation**: Grasses and shrubs that thrive in warmer conditions.

Blue (November)

Blue reflects NDVI values prevalent in November, indicating seasonal crops and vegetation that remain active as the growing season transitions. Typical crops include:

Cereal Crops: Wheat and barley, which may still show some greenness in late fall.

Cyan (July and November)

Cyan is prominent in July and November, indicating healthy vegetation and seasonal crops such as:

- **Cereal Crops**: Showing growth during the latter part of the growing season.
- **Natural Grasslands** and **Mediterranean Shrubs**: These might flourish as temperatures stabilize.

Yellow (March and July)

Yellow indicates NDVI values that peak in both March and July. This suggests crops such as:

Barley, **wheat**, and possibly **rape**, which bloom in spring and show a decline by summer.

Magenta (March and November)

Magenta is evident in March and November, indicating vegetation types that complete their life cycle early in spring. Possible plants include:

Esparto Grass and **Saltbush**, which thrive in semi-arid conditions and can exhibit growth patterns tied to seasonal changes.

The short list of vegetation groups are completely in accordance with botanical researches in the area such as Zine et al. [63] provided detailed information on plant species, taxonomic families, life forms, and life spans found in phosphate mining sites in Morocco as well as Chakkour et al [64] that explores the dominance of therophytes, high phyto-diversity, and native arable plant species in traditional agroecosystems of the Rif Mountains in Morocco.

Color	**Seasons**	**Probable Flora**
Black	Consistent (Mar-May-Jul)	Urban areas, deserted land, water bodies
White	Consistent (Mar-May-Jul)	Irrigated crops, perennial shrubs, managed green spaces, evergreen forests, alfalfa
Blue	March	Wheat, barley
Green	May	Barley, wheat, lentils
Red	July	Winter cereals, legumes, native grasses, shrubs
Cyan	March and May	Seasonal crops, grasslands, shrubs
Yellow	May and July	Winter cereals, legumes
Magenta	March and July	Esparto grass, saltbush, Mediterranean cypress

Table 4.1: Summary of Vegetation Types in Youssouffia Based on NDVI Color Composite (March-May-July 2023)

4.2 Mineral Characterization

In the field of mineral characterization, accurate and efficient data processing is essential for extracting meaningful information from remote sensing imagery. This process involves preparing images acquired from advanced satellite and airborne sensors, ensuring they are suitable for detailed analysis. Proper image preparation not only enhances the reliability of the results but also facilitates the comparison of spectral signatures with known mineral databases. The following sections outline the specific steps taken in the preparation of ECOSTRESS and EMIT images, setting the stage for the subsequent hyperspectral analysis.

Spectral resampling is a technique used to adapt the spectral resolution of data obtained from one sensor to match that of another sensor. This process is crucial in remote sensing and spectroscopy, where data from different instruments need to be compared or combined. For instance, when integrating data from a high-resolution spectrometer with data from a satellite sensor, spectral resampling adjusts the wavelengths and spectral response functions to ensure consistency. The process often involves interpolation or convolution methods to align the spectral characteristics accurately. Effective spectral resampling enhances the reliability of data analysis and ensures that comparisons or integrations of datasets are meaningful and accurate[65].
The need for spectral resampling arises due to the diverse spectral sensitivities of different sensors, which can affect the interpretation of the data. Without resampling, discrepancies in spectral resolution can lead to errors in identifying and quantifying substances or features in the observed scenes. By aligning the spectral profiles, researchers can mitigate these issues, leading to more robust and interpretable results. This technique is essential in fields like environmental monitoring, where precise spectral information is critical for identifying vegetation health, water quality, or soil properties[66].

The image clearly demonstrates that after resampling the spectrometer data (specifically from a Nicolet spectrometer) to match the ECOSTRESS spectral resolution, significant characteristic features of the spectra are lost. The original spectra, rich with detailed features, are essentially reduced to a simplified version that captures only broad trends. This loss of detailed spectral information is a substantial limitation when using ECOSTRESS for mineral detection.

4.2.1 EMIT Spectral Analysis

Apatite Band math

By inspection of sample apatites from ASTER library three features are observed at 1989nm, 2152nm and 2308 nm.

Apatite features: Wavelength 1989.15 (nm)

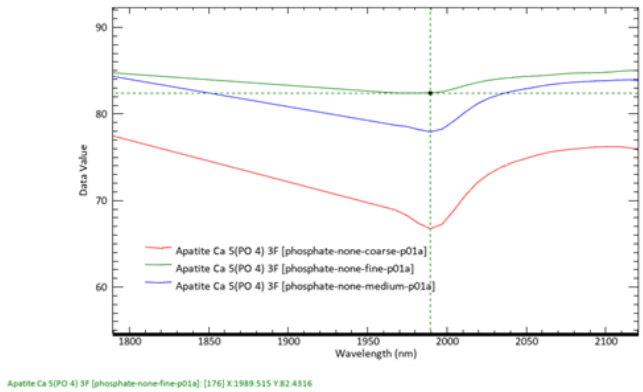

Figure 4.3: first observed feature in the SWIR range, at wavelength of 1989 nm which is band 217 of EMIT, right after the missing bands due to atmospheric disruption which indeed leads to missing bands.

This wavelength is equivalent to band 217 of EMIT, therefore the band math to be applied on the library samples and the image is:

Feature Wavelengths from Resampled Spectra in nm	1967	1989	2197	Band Math
Equivalent bands	**B214**	**B217**	**B224**	**B214+b224/b217**
Reflectance value for Apatite Fine Grain	81.61310	82.89370	82.52930	0.50501
Reflectance value for Apatite Medium Grain	67.89270	69.97860	68.80500	0.51192
Reflectance value for Apatite Coarse Grain	76.76800	79.14400	78.72010	0.50900

Table 4.2: Before proceeding with the "band math" on the ROI, it is necessary to compute band math for the spectra at hand which are acquired from ASTER library embedded in ENVI, in other to obtain a specific range to be used later when performing “Raster Color Slice”.

After applying the band math in the table above the folowing image grey-style image is created:

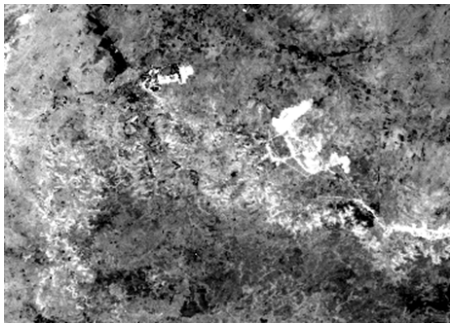

Figure 4.4: EMIT image after applying the shoulder band math at wavelength 1989nm

The results of shoulder band math after applying raster color slice. The red color is the range of 2.07 to 2.146 which corresponds respectively to medium grain apatite and coarse grain apatite. Again, the yellow color corresponds to the range between 2.02 and 2.07 in which according to table are fine and medium sized grains.

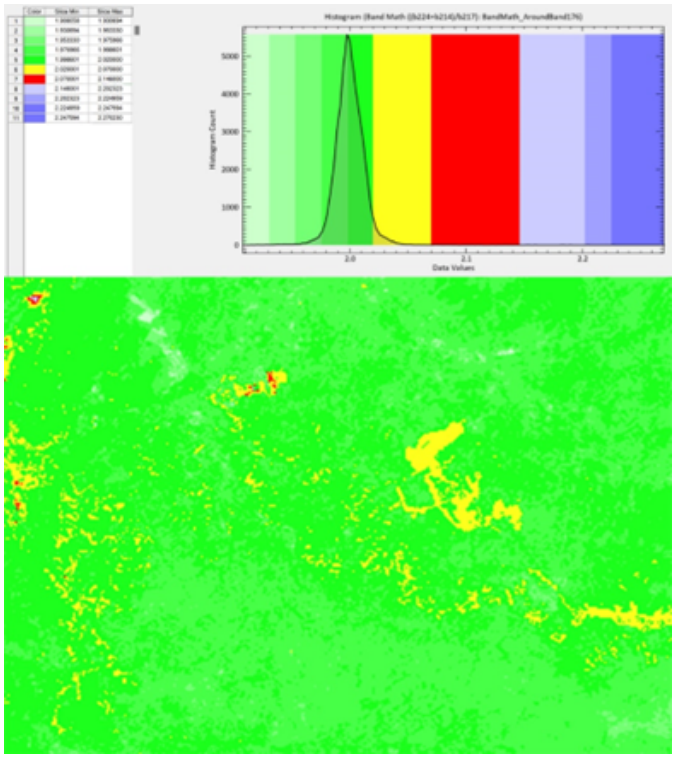

Figure 4.5: Analysis of Shoulder Band Math Results Using Raster Color Slice (Shown in Red)

Apatite features: Wavelength 2152 (nm)

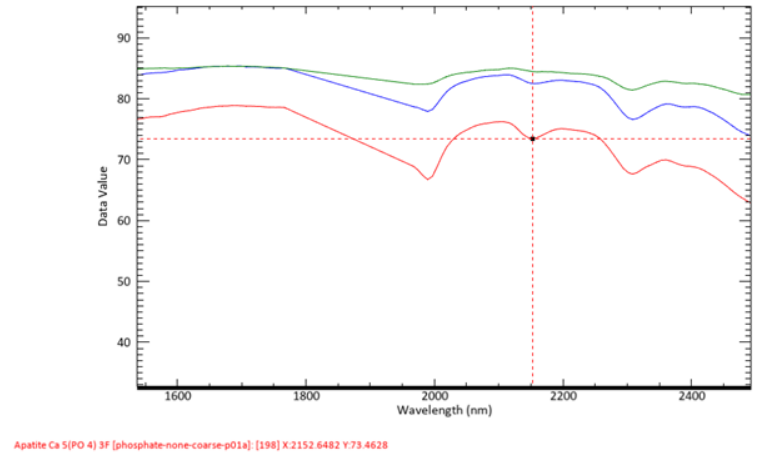

Figure 4.6: The 2nd observed feature of apatite in the SWIR range, at wavelength of 2152 nm which is band 239 of EMIT

Feature Wavelengths from Resampled Spectra in nm	1989	2115	2152	2197	2308	Band Math
Equivalent bands	b217	B234	B239	B245	B260	(b234+b245)/(b218+b239+b260)
Reflectance value for Apatite Fine Grain	82.43160	85.01580	84.47470	84.31690	81.43810	0.68185
Reflectance value for Apatite Medium Grain	77.93390	83.95010	82.48590	83.05320	76.60390	0.70458
Reflectance value for Apatite Coarse Grain	66.74900	76.07480	73.46280	75.09030	67.62870	0.72731

Table 4.3: Reference Table for Apatite feature at 2152nm

The analysis of the shoulder band mathematics reveals significant insights after the application of raster color slicing techniques. The red color in the visual representation highlights a specific reflectance range of 0.70458 to 0.72731, indicating the presence of medium grain apatite and coarse grain apatite. This distinction is crucial for identifying the varying characteristics of apatite minerals. In contrast, the yellow color in the image corresponds to a reflectance range between 2.02 and 2.07, which, as outlined in the accompanying table, relates to fine and medium-sized grains. This color-coding provides an intuitive visual guide to understanding the mineral composition and can facilitate further analysis of apatite mineral distributions.

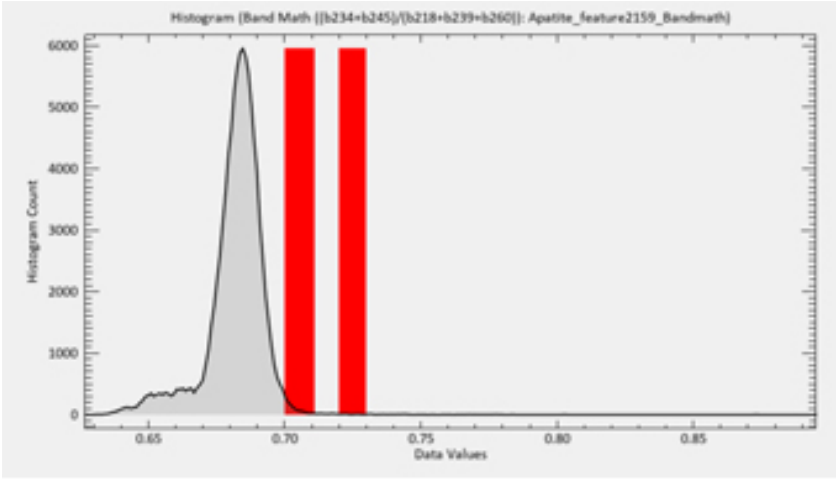

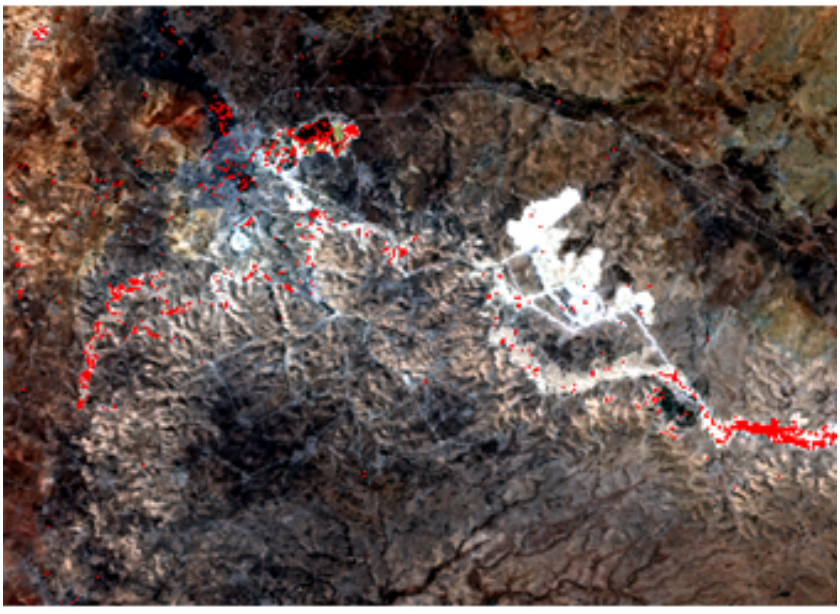

Figure 4.7: Reflectance Analysis of Apatite Grains Using Shoulder Band Math and Raster Color Slicing (Shown in red)

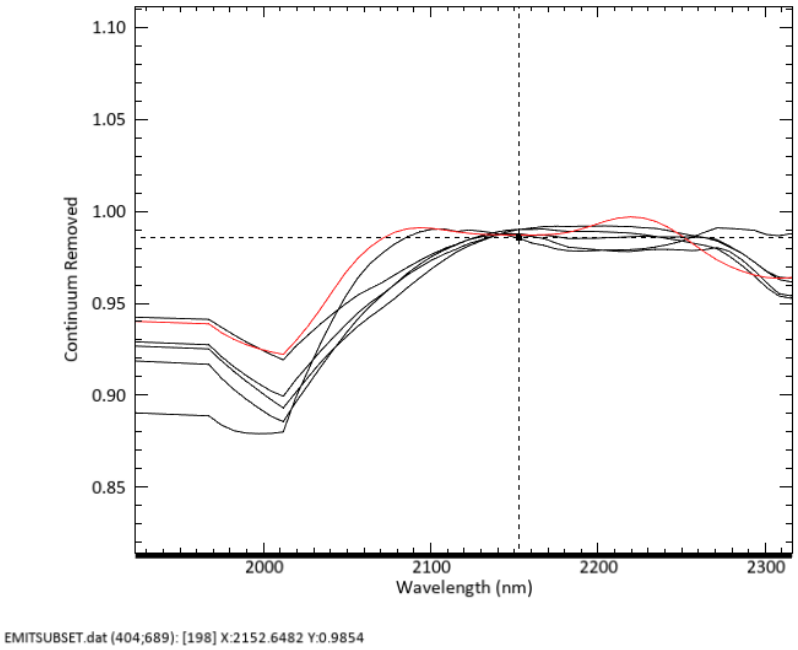

Figure 4.8: Comparison of the selected Apatite(feature at 2152nm) sample from the spectral library of ENVI(in red) with spectral profiles obtained from various points within the area of interest (in black) reveals weak similarities.

Apatite features: Wavelength 2308 (nm)

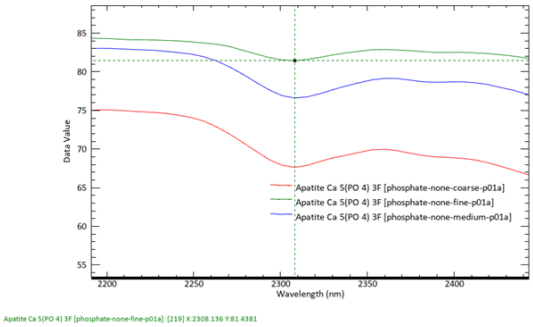

Figure 4.9: The 3rd observed feature of apatite in the SWIR range, at wavelength of 2308 nm which is band 260 of EMIT

Feature Wavelengths from Resampled Spectra in nm	2256	2308	2359	Band Math
Equivalent bands	b253	b260	b267	(b253+b267)/b260
Reflectance value for Apatite Fine Grain	83.72200	81.43810	82.89370	2.04592
Reflectance value for Apatite Medium Grain	81.92240	76.60390	79.14400	2.10259
Reflectance value for Apatite Coarse Grain	73.57000	67.62870	62.97760	2.01908

Table 4.4: Reference Table for apatite at 2308 nm

The results of the shoulder band math, enhanced by raster color slicing, reveal important insights into apatite grain sizes. In this analysis, the red color represents a reflectance range from 2.01908 to 2.04592, which corresponds to coarse and fine grain apatite. Meanwhile, the yellow color highlights a reflectance range of 2.04592 to 2.10259, indicating the presence of fine and medium-sized grains. This color coding not only simplifies the identification of different apatite types but also enhances our understanding of their distribution and characteristics.

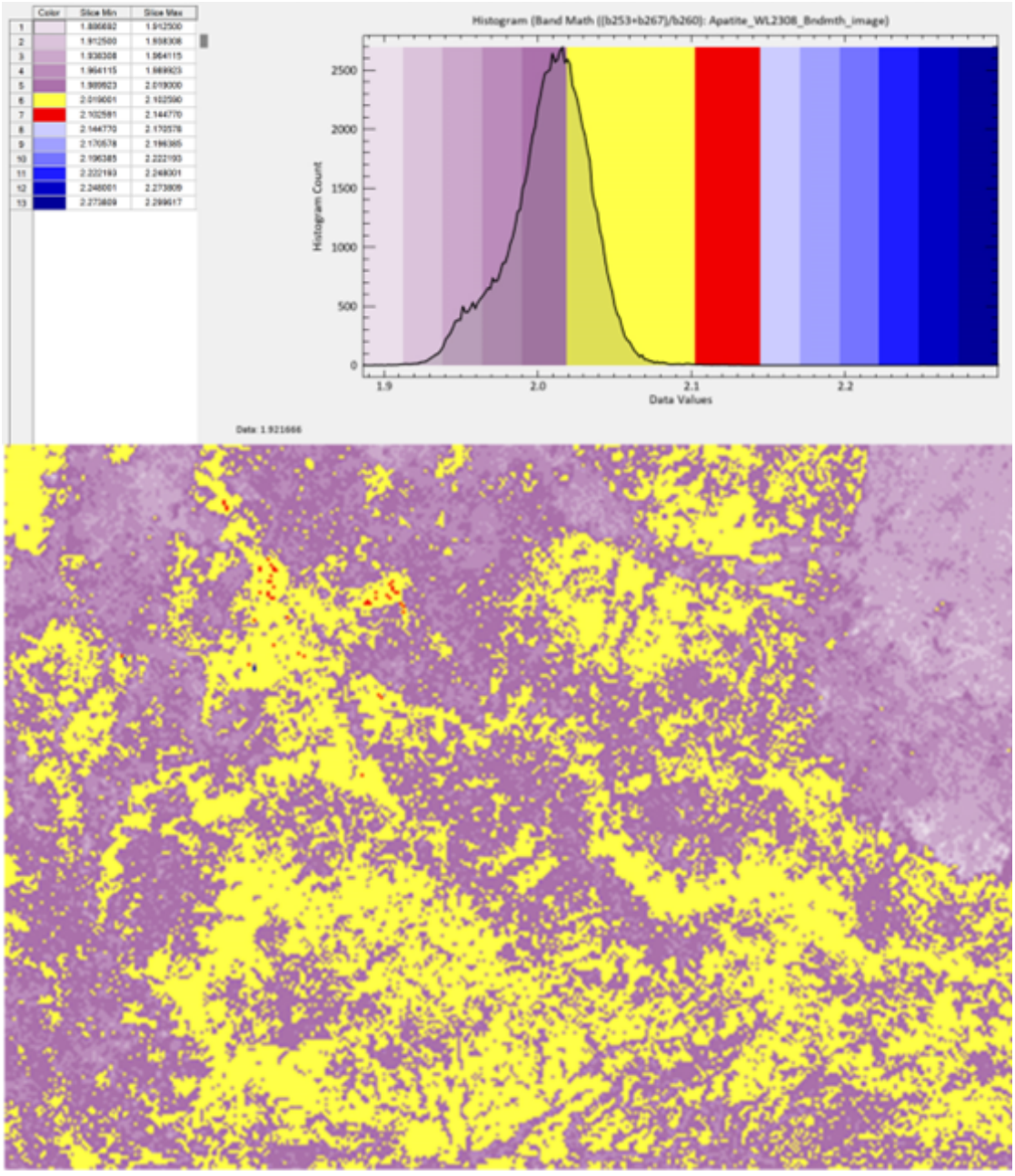

Figure 4.10: Reflectance Analysis of Apatite Grains Using Shoulder Band Math centered at 2308 nm and Raster Color Slicing

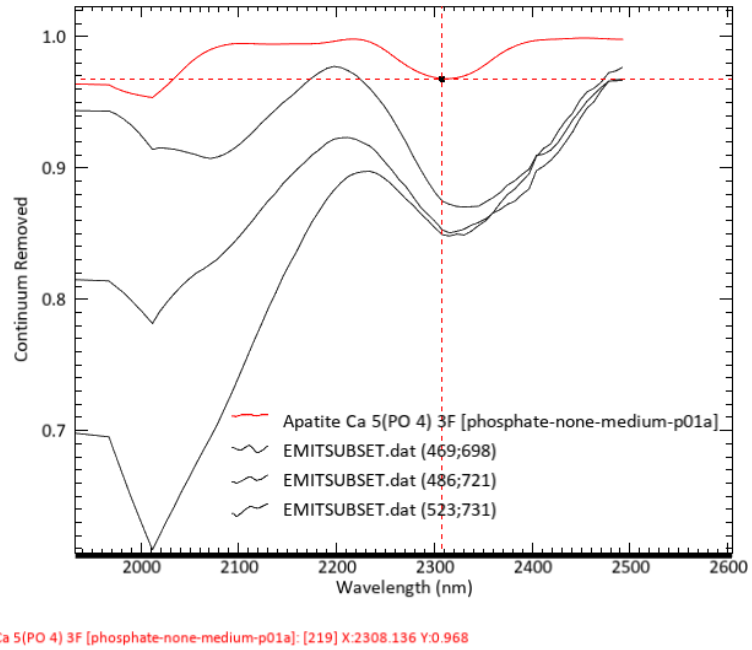

Figure 4.11: Comparison of the selected Apatite(feature at 2308nm) sample from the spectral library of ENVI(in red) with spectral profiles obtained from various points within the area of interest (in black) reveals weak similarities.

Kaolinite Band Math

In kaolinite with high crystallinity, four bands are associated with the vibrational O-H process. Absorption bands at 1345 nm, 1379 nm, and 1393 nm correspond to inner-surface OH groups, while well-ordered kaolinite exhibits near-infrared bands forming a doublet at 2180 nm and 2190 nm, resulting from stretching and bending vibrations of OH groups. An additional absorption band at 2208 nm is linked to combined modes of inner-surface hydroxyl groups. In disordered kaolinite, the OH bands reflect disorder, with localized absorption bands at 1340 nm, 1395 nm, and 1409 nm tied to stretching processes (García-Vicente et al. 2021b).

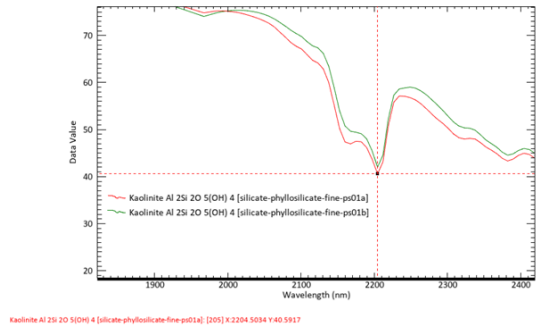

Figure 4.12: The absorption band of Kaolinite centered at 2208 nm is associated with the combined stretching and bending modes of inner-surface hydroxyl groups

Wavelength of Kaolinite from Perkin Spectral Library (nm)	2182	2204	2234	Feature Band Math
Equivalent EMIT band	243	246	250	(b243+b250)/b246
Perkin_Kaolinite fine a	47.40770	40.59170	57.13870	2.57556
Perkin_Kaolinite fine b	49.10990	42.01150	58.64030	2.56478

Table 4.5: Reference Table for Kaolinite at 2204 nm

Since the range of pixel values of the band math image [1.963218, 2.358985] is out of the range of Perkin spectral library [2.57556, 2.56478] there is no color association with Kaolinite in the image. This implies that the material represented by the pixel values in the band math image is not Kaolinite, or at least, it does not exhibit the spectral signature typically associated with Kaolinite according to the Perkin spectral library. the same procedure of creating a raster color slice image is repeated with samples from Beckman Library. in this 2nd attempt to delineate the whereabouts of Kaolinite, another partitioning of the pixel values are considered using values from Beckman spectra. This time, the Range computed band math using spectra from Beckman [2.27985, 2.32859] has overlap with pixel value of the image with a range of [1.963218, 2.358985]. This overlapping is shown with the red color in the image.

Wavelength of Kaolinite From Beckman Spectral Library (nm)	2182	2204	2322	Feature Band Math
Equivalent EMIT band	243	246	250	(b243+b250)/b246
Kaolinite fine a	61.04360	57.97010	71.11960	2.27985
Kaolinite fine b	56.49200	52.83520	66.53940	2.32859

Table 4.6: The Band Math values are again computed for the reflectance values of spectra of Beckman Instrument to examine if there is a range overlapping with the image of band Math.

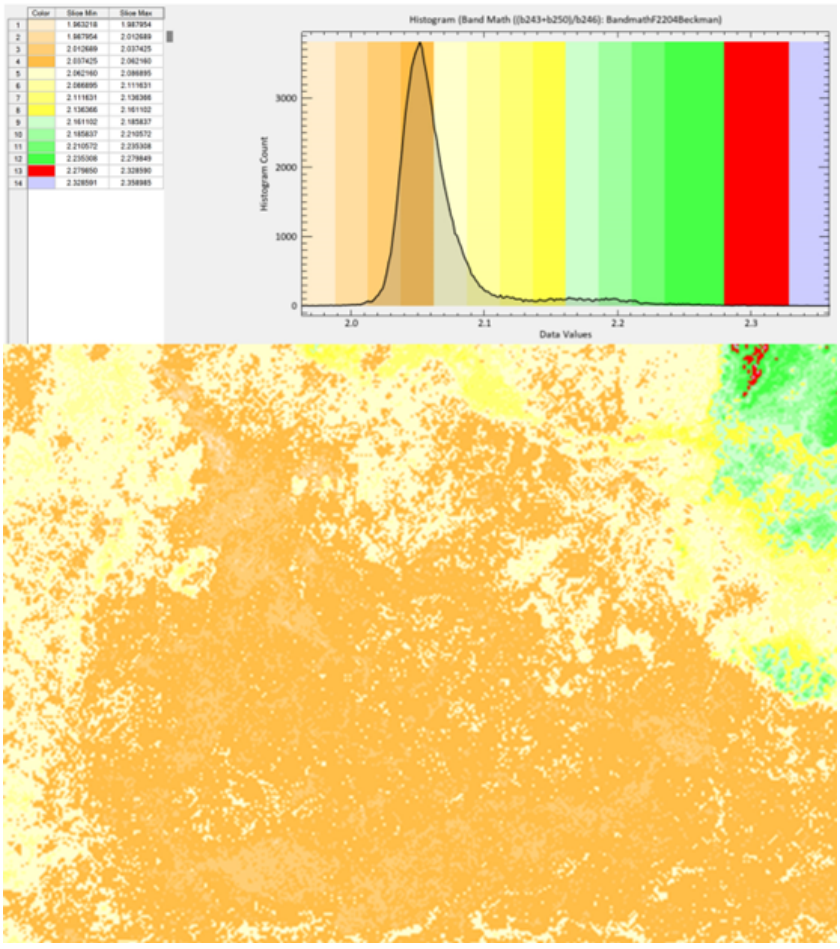

Figure 4.13: This image shows the second attempt to delineate kaolinite distribution, highlighting the overlap between the Beckman spectra range of [2.27985, 2.32859] and the pixel values [1.963218, 2.358985] in red.

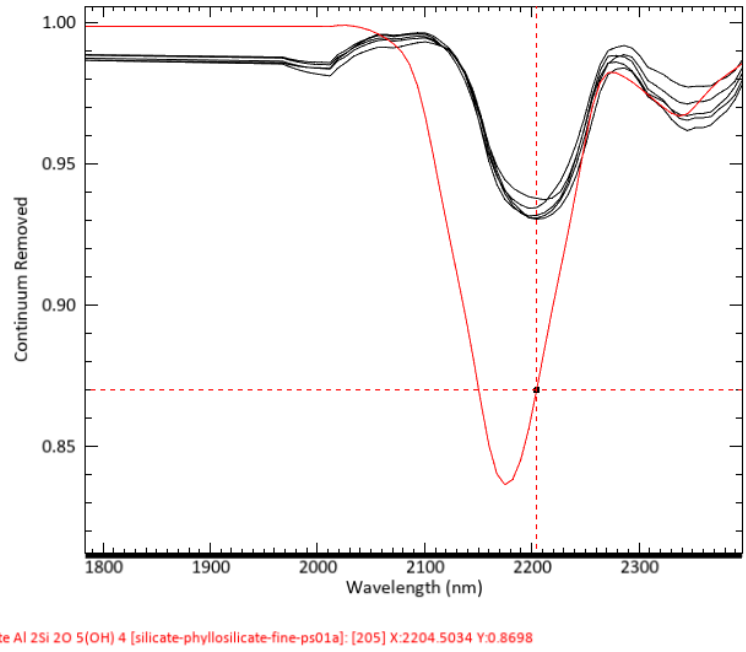

Figure 4.14: Comparison of the selected Kaolinite (feature at 2204nm) sample from the spectral library of ENVI(in red) with spectral profiles obtained from various points within the area of interest (in black) reveals similar patterns.

Dolomite Band Math

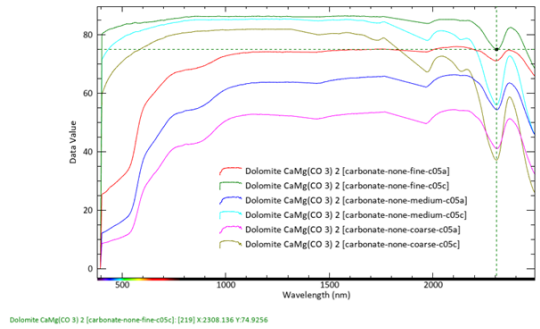

Figure 4.15: Dolomite Feature Centered at 2308nm

Wavelength of Dolomite From Beckman Spectral Library (nm)	2174	2308	2367	Band Math
Equivalent EMIT band	242	260	268	(b242+b268)/b260
Dolomite [Carbonate_fine_c05a]	75.41870	71.13740	74.68700	2.11008
Dolomite [Carbonate_fine_c05c]	84.81150	74.92560	82.27240	2.23000
Dolomite [Carbonate_Medium_c05a]	65.73660	54.25110	63.38830	2.38013
Dolomite [Carbonate_Medium_c05c]	78.44120	55.95440	72.72790	2.70165
Dolomite [Carbonate_Coarse_c05a]	53.84500	40.95990	58.71250	2.74799
Dolomite [Carbonate_Coarse_c05c]	67.75070	37.06550	51.27560	3.21124

Table 4.7: Six types of dolomites have been selected from the Beckman spectral library embedded in ENVI to obtain a range of pixel values for band math. This band math has been applied to highlight the characteristic features of the material.

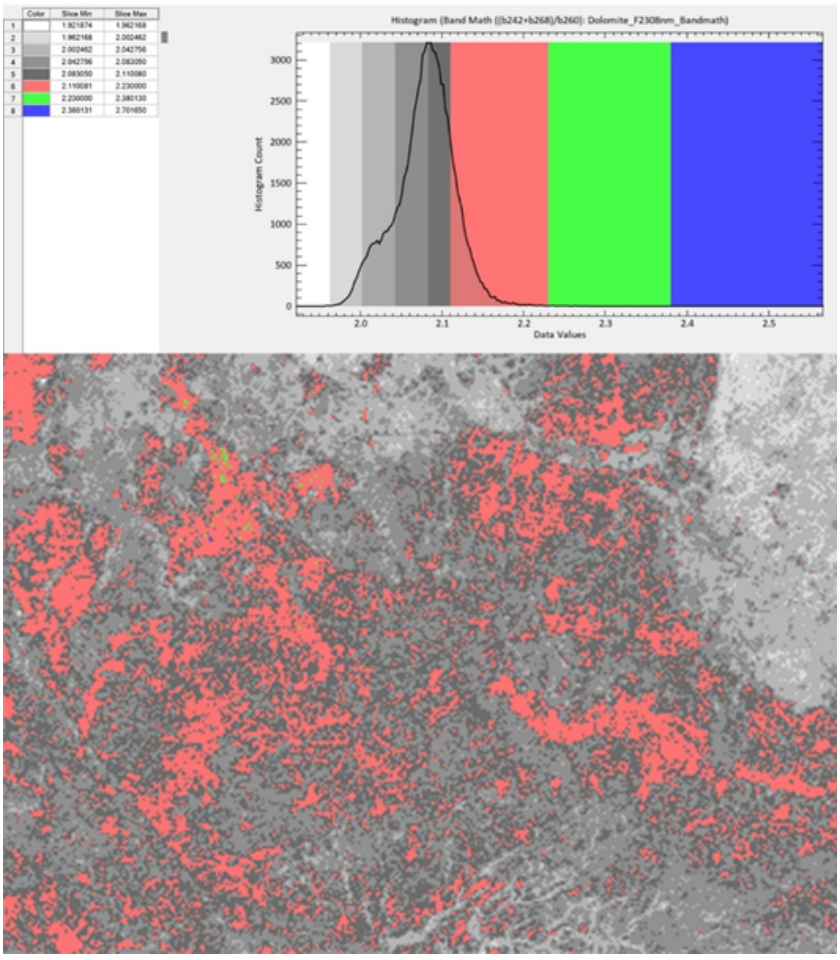

Figure 4.16: The red areas in the imagery specifically indicate the presence of dolomite, suggesting a significant distribution of this mineral type within the observed region.

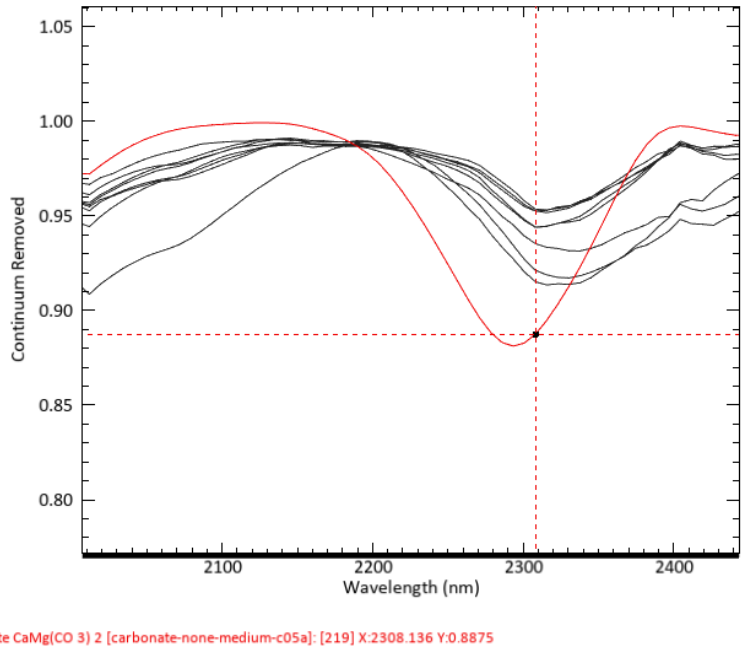

Figure 4.17: Comparison of the selected Dolomite (feature at 2308nm) sample from the spectral library of ENVI(in red) with spectral profiles obtained from various points within the area of interest (in black) reveals similar patterns.

Gypsum Band Math

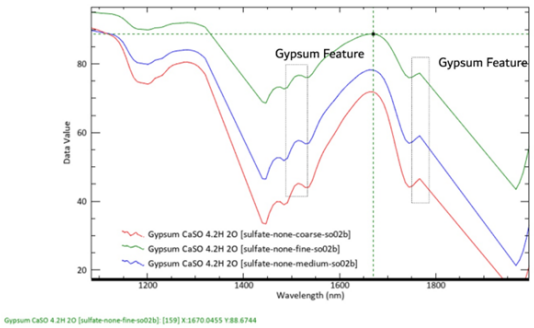

Figure 4.18: Gypsum Signature -Highlighting the feature between 1500nm and 1750 nm

Gypsum exhibits distinctive spectral features at wavelengths of 1500 nm and 1700 nm in the SWIR range. However, the 1.5 m feature is unsuitable for remote sensing due to interference from atmospheric water vapor absorption. Additionally, the 2.2 m doublet absorption can be confused with similar features found in clay minerals, making spectral discrimination challenging, particularly when dealing with low-quality spectral data. To simplify the analysis and improve accuracy, both features are combined into a single band math calculation. The wavelength of 1670 nm, which represents a peak between the 1500 nm and 1700 nm features, is used as the reference point for this calculation. This approach helps to highlight gypsum more effectively while minimizing the interference from other materials.

Gypsum Feature at 1670 nm

Wavelength of Gypsum From Beckman Spectral Library (nm)	1513	1670	1766	Band Math
Equivalent EMIT band	153	174	187	(b153+b187)/b174
Gypsum CaSO4.2H2O (Sulfate_None_fine_so02b)	76.6938	88.6744	77.3118	1.7368
Gypsum CaSO4.2H2O (Sulfate_None_medium_so02b)	57.7418	78.2063	59.0851	1.4938
Gypsum CaSO4.2H2O (Sulfate_None_coarse_so02b)	45.2332	71.8532	46.6342	1.2785

Table 4.8: Gypsum Refrence Table in SWIR with the feature centered at 1670nm

Based on the pixel value range, it can be inferred that this band math primarily captures medium and fine-grained gypsum. The band math value of 1.2785, which corresponds to coarse-grained gypsum, falls outside the pixel range.

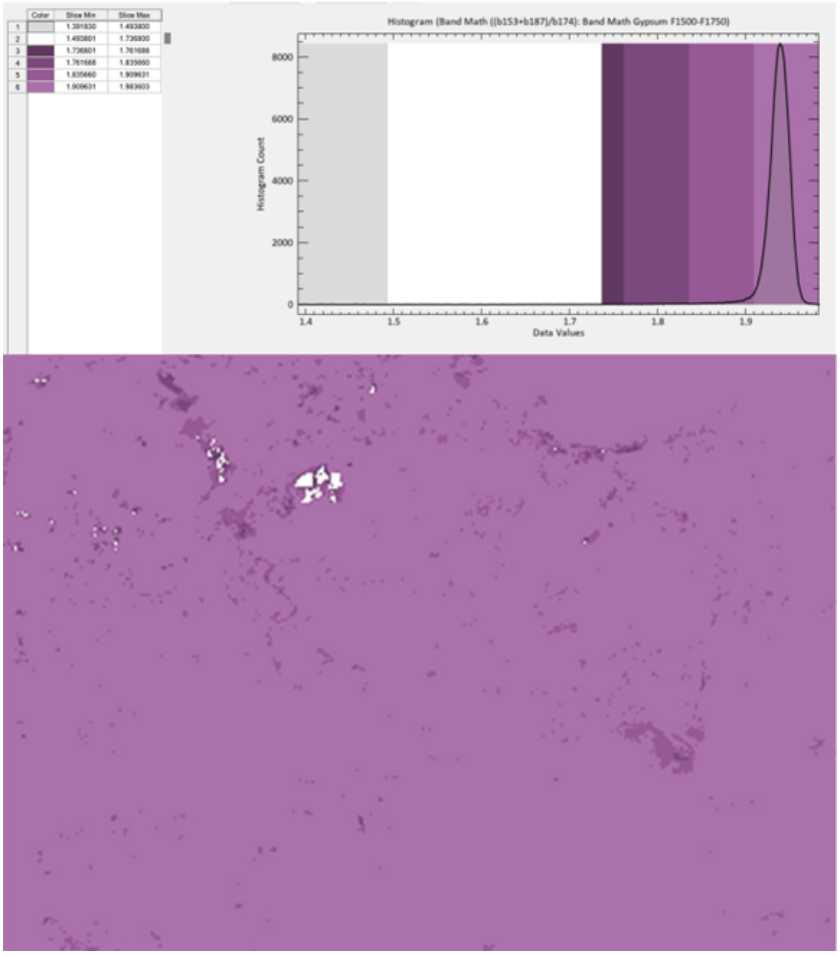

Figure 4.19: The raster color slice image and the histogram of the area of interest which includes the two characteristic features at 1500nm and 1750 nm in a single band math

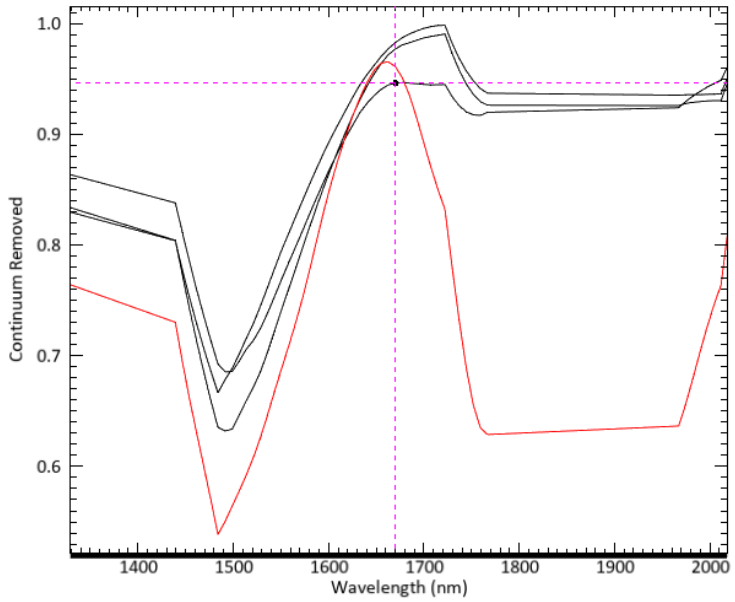

Figure 4.20: Comparison of the selected Gypsum (feature in range 1500-1750nm) sample from the spectral library of ENVI(in red) with spectral profiles obtained from various points within the area of interest (in black) reveals similar patterns.

Gypsum Feature at 2200 nm

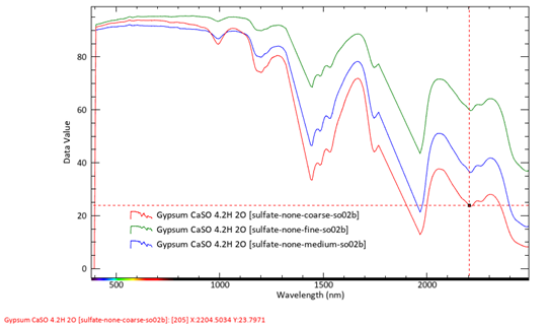

Figure 4.21: The absorption band of Gypsum centered at 2204 nm

This time, to perform the band math, two steps on the right side of the absorption feature are used to increase the likelihood of accurately capturing gypsum in the image. For the absorption feature at 2204 nm, the left shoulder wavelength is set at 2056 nm, while the right shoulder wavelengths are set at 2241 nm and 2308 nm. This approach enhances the detection accuracy of gypsum by incorporating additional reference points on both sides of the absorption feature, improving spectral discrimination and reducing potential interference from other materials.

Wavelength of Gypsum From Beckman Spectral Library (nm)	2056	2204	2241	2308	Band Math
Equivalent EMIT band	226	246	251	260	(b226+b251+b260)/b246
Gypsum CaSO4.2H2O (Sulfate_None_fine_so02b)	71.6359	59.9576	61.9724	64.2127	3.2993
Gypsum CaSO4.2H2O (Sulfate_None_medium_so02b)	51.0849	36.6014	38.9851	41.7981	3.6028
Gypsum CaSO4.2H2O (Sulfate_None_coarse_so02b)	37.6907	23.7971	25.6420	28.0616	3.8406

Table 4.9: Gypsum exhibits another distinct feature at 2200 nm. To increase accuracy, instead of choosing a single shoulder on the right, both steps on the right side are selected for the band math.

After conducting band math centered at 2204 nm, the resulting image from the raster color slice reveals a different location compared to the previous image, which was generated using band math for two other features at 1500 nm and 1750 nm.

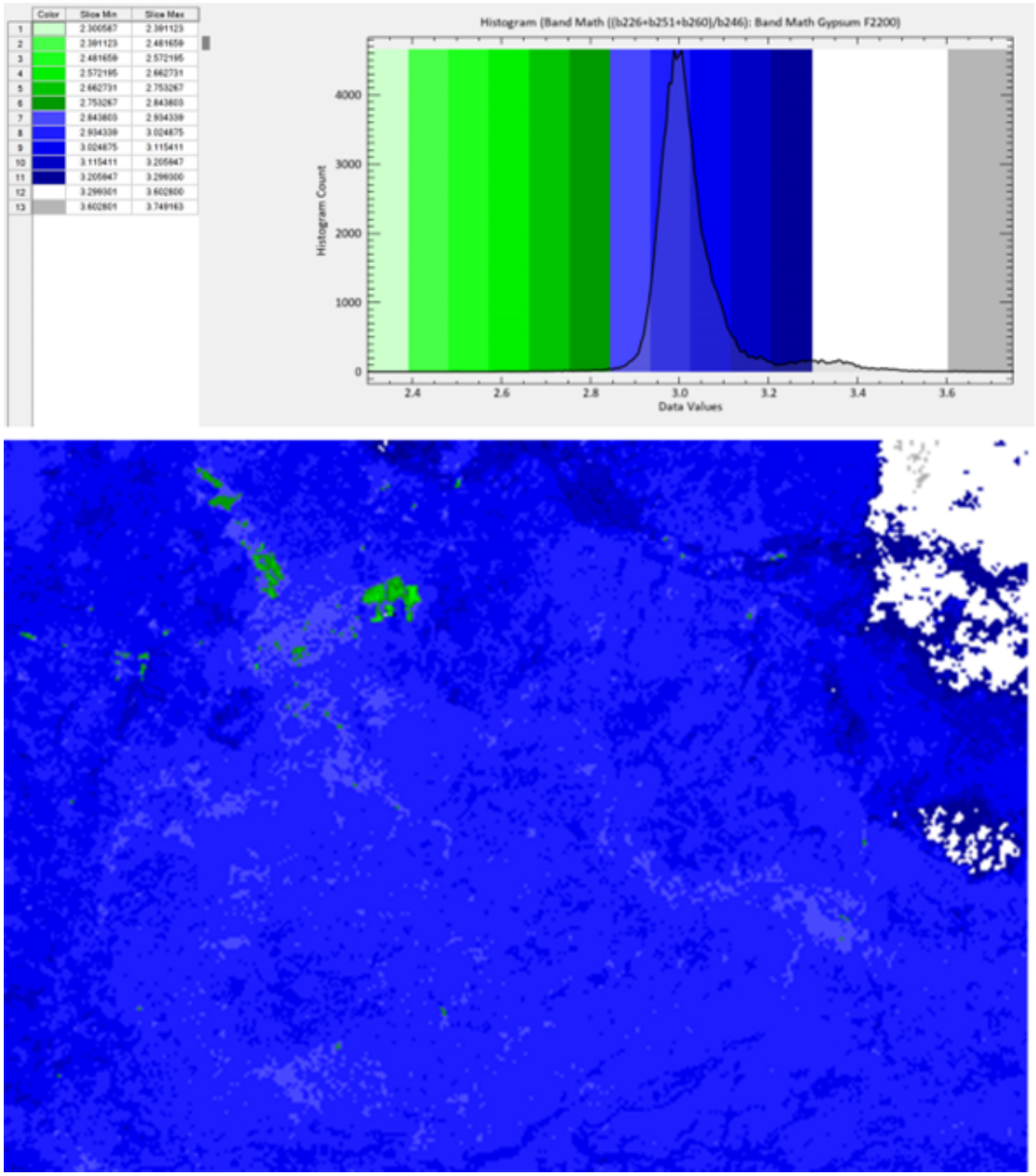

Figure 4.22: After band math centered at 2204 nm, the raster color slice image shows different locations compared to band math at 1500 nm and 1750 nm. Gypsum is shown is White Here.

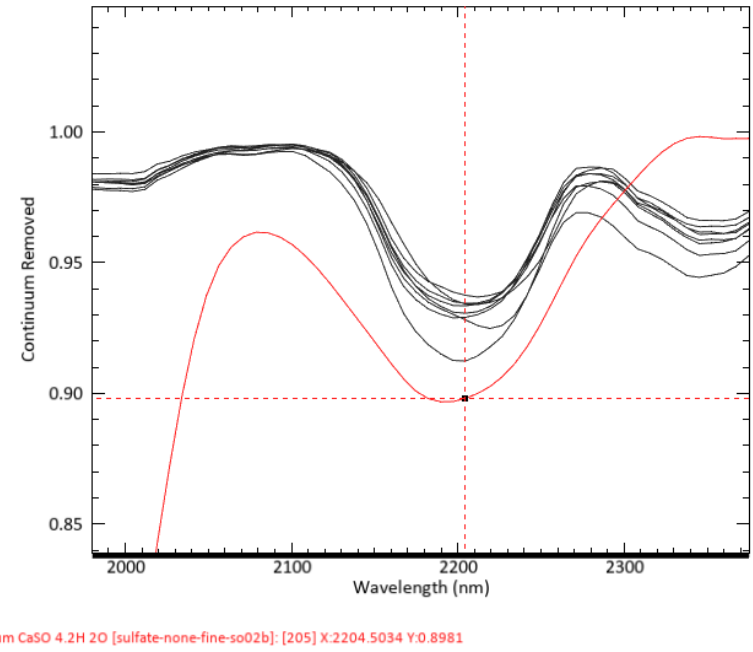

Figure 4.23: Comparison of the selected Gypsum (feature at 2200nm) sample from the spectral library of ENVI(in red) with spectral profiles obtained from various points within the area of interest (in black) reveals similar patterns.

Illite Band Math

Illite has distinct absorption features at approximately 1410 nm, 1910 nm, and 2210 nm. Although these features are similar to those of illite-smectite and smectite, their intensities differ. The spectral distinction of illite can generally be determined by examining the ratio of the minima of the H2O absorption feature to the minima of the AlOH absorption feature.[31]

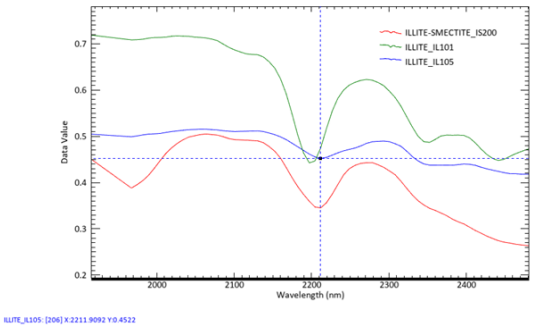

Figure 4.24: The absorption band of illite centered at 2211 nm

Wavelength of Illite From IGCP Spectral Library (nm)	2130	2211	2271	Band Math
Equivalent EMIT band	236	247	255	(b236+b255)/b247
Illite Smectite IS200	0.4901	0.3451	0.4429	2.7036
Illite IL101	0.6764	0.4748	0.6228	2.7363
Illite IL105	0.5117	0.4522	0.4848	2.2037

Table 4.10: Band Math calculation for Illite feature at 2211nm from IGCP Spectral Library (nm)

The raster color-sliced image and the corresponding histogram of the band math image for illite reveal its potential geographical distribution within the area of interest. The analysis indicates that illite is primarily concentrated in the top-right section of the region, highlighted in beige on the resulting image. This visualization offers a clear spatial representation of illite's presence, providing valuable insight into its distribution patterns in the studied area.

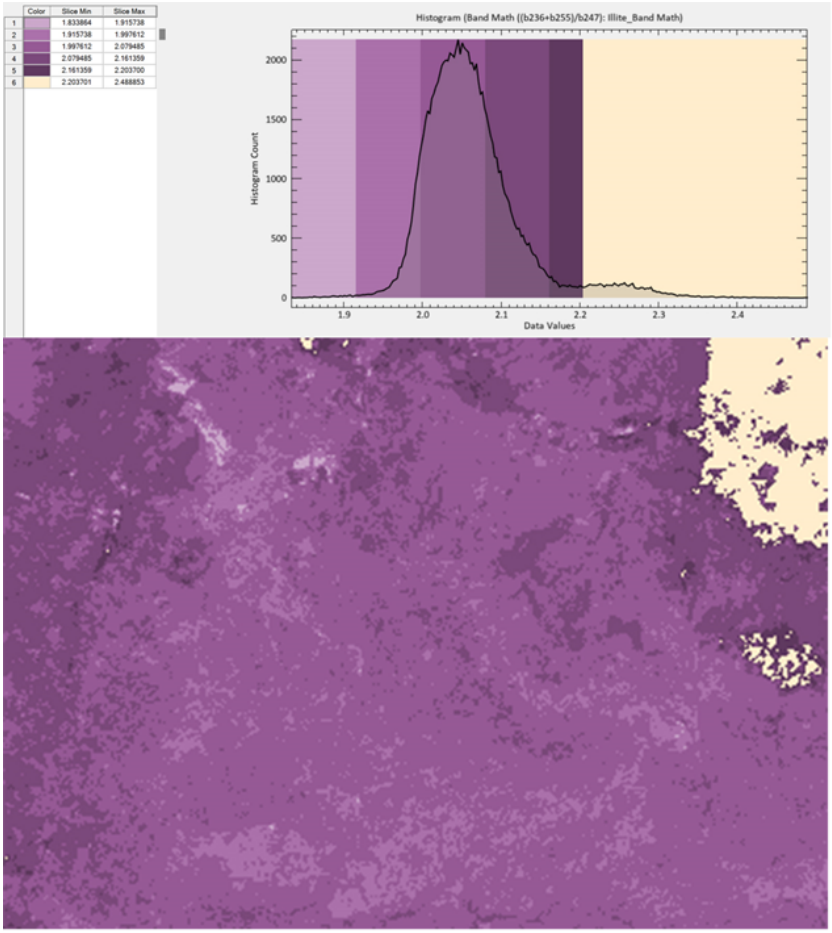

Figure 4.25: Raster color-sliced image and histogram of the band math for illite, highlighting its distribution in the top-right area in beige

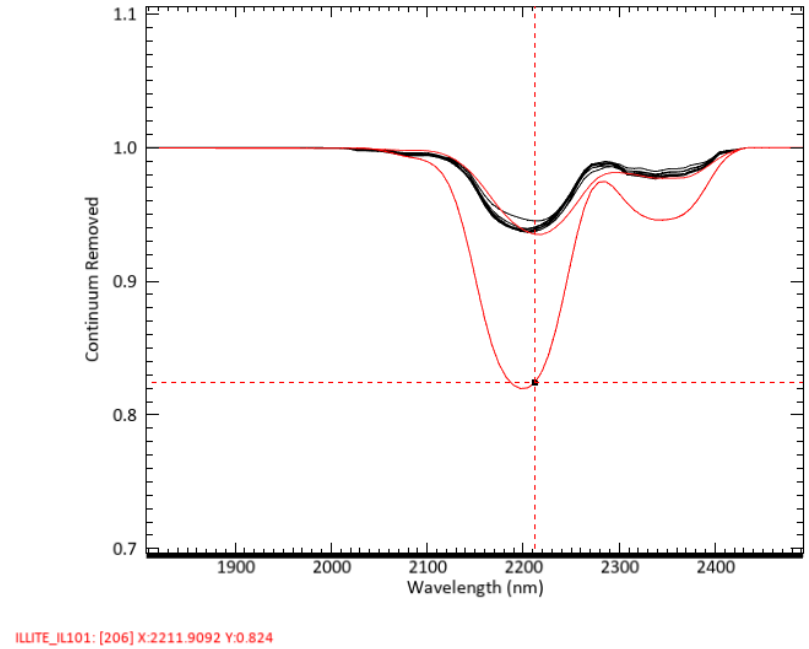

Figure 4.26: Comparison of the selected Illite sample from the spectral library of ENVI(in red) with spectral profiles obtained from various points within the area of interest (in black) reveals similar patterns.

Calcite Band Math

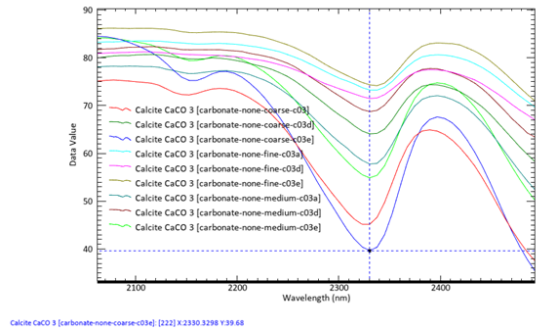

Figure 4.27: Nine samples are selected from Beckman spectral library to study their features.

The raster color-sliced image of the area of interest, along with its corresponding

Wavelength of Calcite From Beckman Spectral Library (nm)	**2189**	**2330**	**2396**	**Band Math**
Equivalent EMIT band	**244**	**263**	**272**	**(b244+b272)/b263**
Calcite CaCO3 [Carbonate_None_Fine_c03a]	82.94660	73.27900	80.63380	2.23230
Calcite CaCO3 [Carbonate_None_Fine_c03d]	80.35050	74.35780	77.48320	2.12262
Calcite CaCO3 [Carbonate_None_Fine_c03e]	85.35920	71.49680	83.12180	2.35648
Calcite CaCO3 [Carbonate_None_Medium_c03a]	77.32710	57.78780	72.07860	2.58542
Calcite CaCO3 [Carbonate_None_Medium_c03d]	81.56280	68.74860	77.71590	2.31683
Calcite CaCO3 [Carbonate_None_Medium_c03e]	80.45720	54.89610	74.77140	2.82768
Calcite CaCO3 [Carbonate_None_Coarse_c03]	73.50750	45.16260	64.68160	3.05981
Calcite CaCO3 [Carbonate_None_Coarse_c03d]	79.76010	64.09680	74.34850	2.40431
Calcite CaCO3 [Carbonate_None_Coarse_c03e]	77.14080	39.68000	67.46520	3.64430

Table 4.11: The reference table for reflectance values of the samples at the calcite feature wavelength, along with two other values as reference points, are chosen to establish pixel value ranges for performing the raster color slice.

histogram, illustrates the distribution of various calcite types. Light purple represents fine calcites (c03a, c03d), while red highlights fine calcite c03e and medium calcite c03d. The image shows minimal results according to this type of sample.

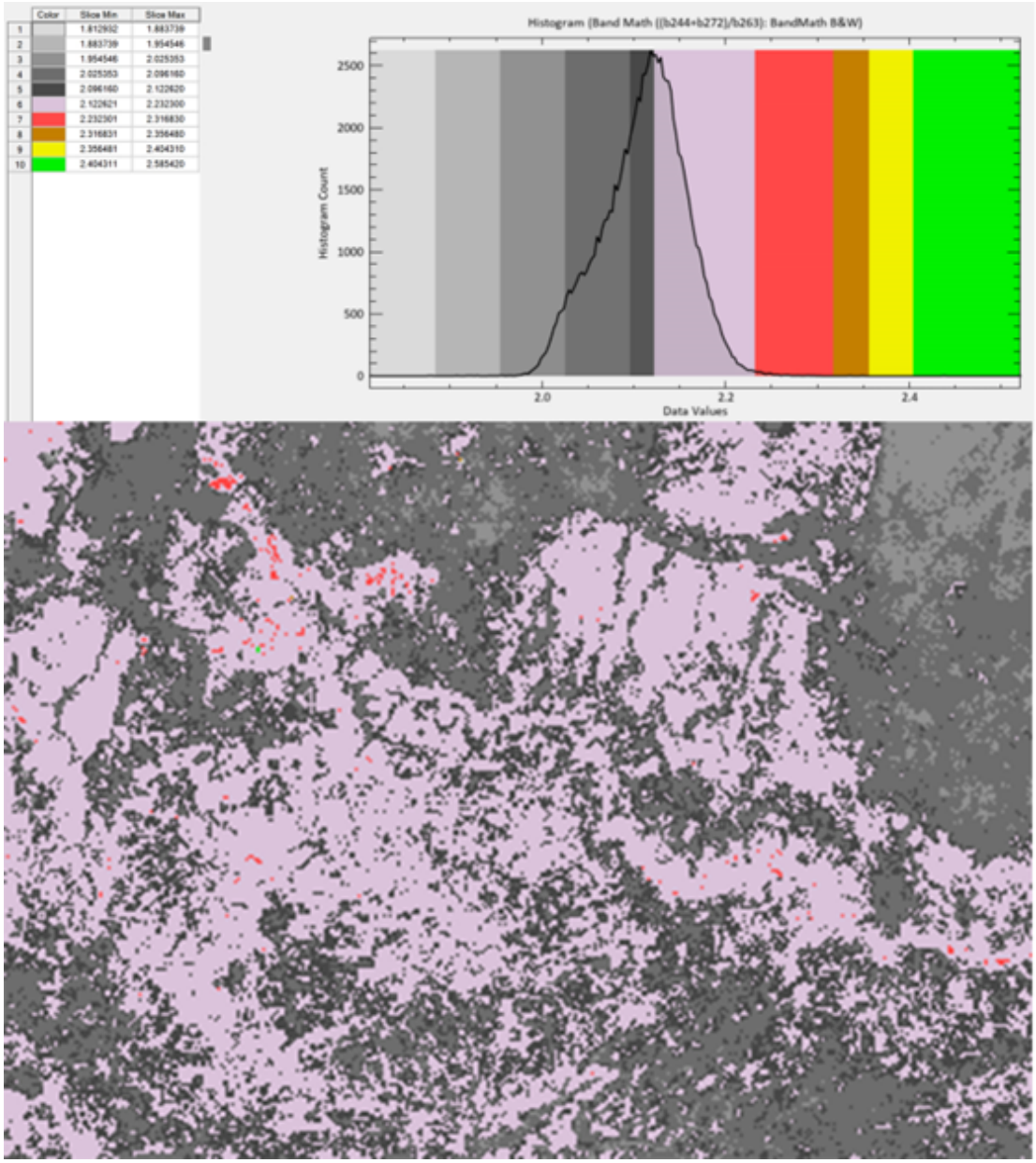

Figure 4.28: Raster color-sliced image and histogram depicting the distribution of fine and medium calcites,minimal results according to the selected samples.

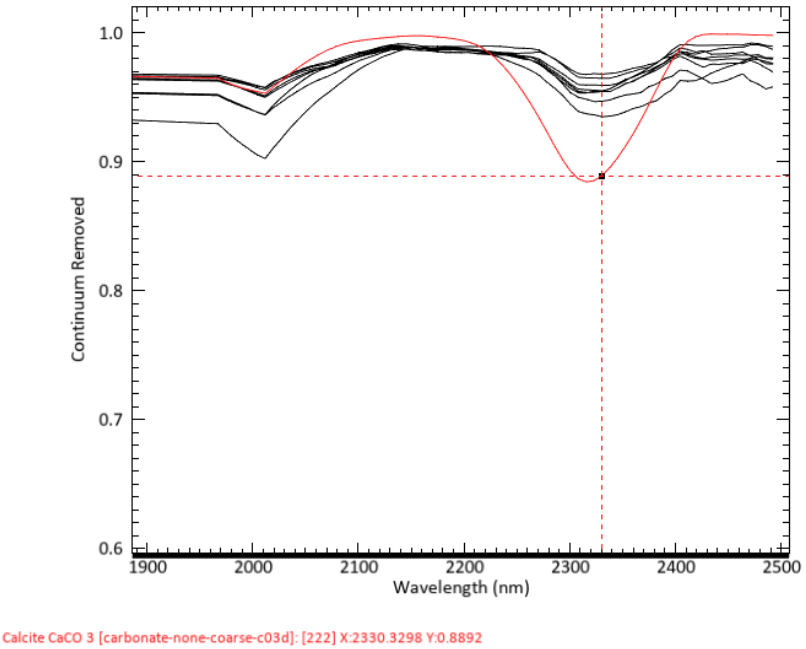

Figure 4.29: Comparison of the selected calcite sample from the spectral library of ENVI (red color) with spectral profiles obtained from various points within the area of interest (black color)reveals similar patterns.

Sepiolite Band Math

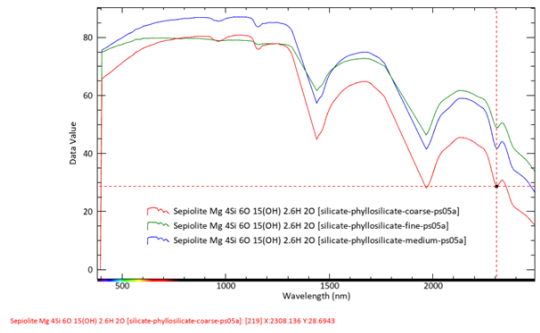

Figure 4.30: Three samples of sepiolite are selected from Beckman spectral library to study their features.

Regarding the literature and the spectral library of the Beckman, the only feature for sepiolite that can be practically used for band math is 2308 nm. For

highlighting this feature, reflectance values of different samples of sepiolite are read for the wavelengths of 2241nm and 2330 nm to be used in a band math ratio.

Wavelength of Sepiolite From Beckman Spectral Library (nm)	**2241**	**2308**	**2330**	**Band Math**
Equivalent EMIT band	**251**	**260**	**263**	**(b251+b263)/b260**
Sepiolite Mg4Si6O15(oh)2.6H2O [Silicate_phyllosilicate_fine_ps05a]	58.8525	48.8567	50.5587	2.2394
Sepiolite Mg4Si6O15(oh)2.6H2O [Silicate_phyllosilicate_medium_ps05a]	55.6110	41.6671	44.0803	2.3926
Sepiolite Mg4Si6O15(oh)2.6H2O [Silicate_phyllosilicate_coarse_ps05a]	41.8437	28.6943	30.7626	2.5303

Table 4.12: The refrence table of reflectance values of the samples at the sepiolite feature wavelength, along with two other values as reference points, are chosen to establish pixel value ranges for performing the raster color slice.

The raster color slice of the area of interest, accompanied by a histogram, highlights key spectral features associated with sepiolite distribution. Yellow spots, marked with dotted lines, indicate regions with fine to medium grain sepiolite.

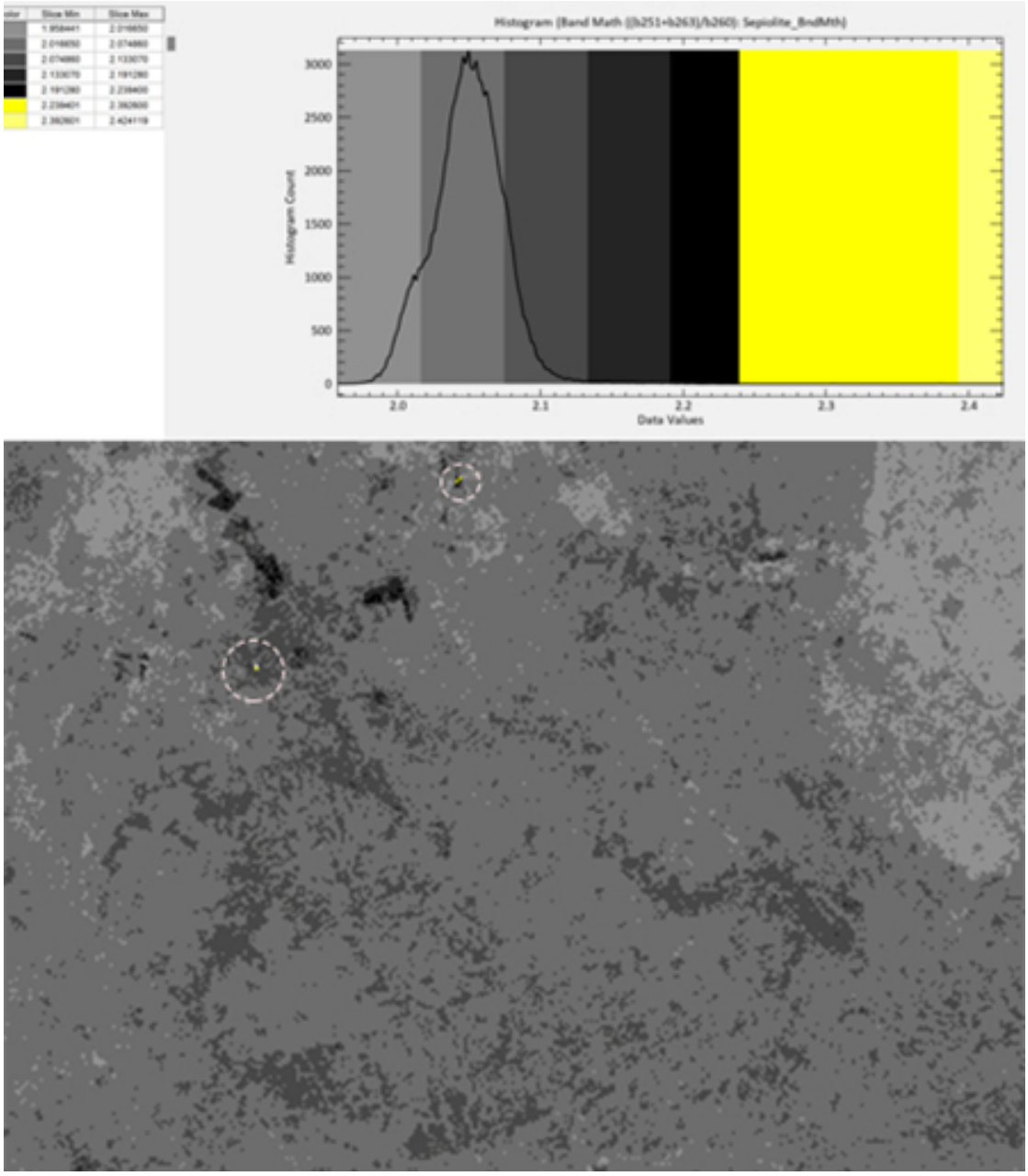

Figure 4.31: Raster color slice of the area of interest with a histogram, showing yellow spots encircled in dotted lines according to the selected sepiolite samples

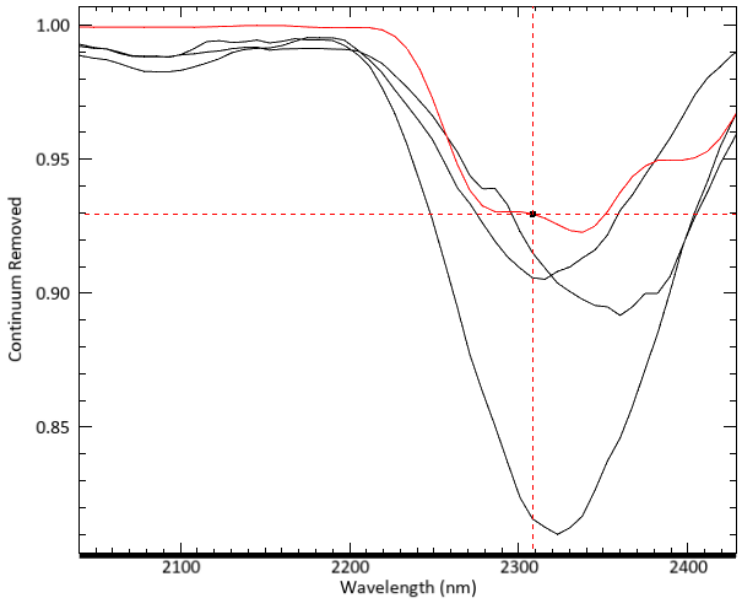

Figure 4.32: Comparison of the selected Sepiolite sample from the spectral library of ENVI with spectral profiles obtained from various points within the area of interest reveals similar patterns.

4.2.2 ECOSTRESS Spectral Analysis

The Nicolet spectrometer provides high-resolution spectral data, which is crucial for identifying specific minerals based on their unique spectral signatures and features. However, when this data is resampled to the lower resolution of ECOSTRESS, many of these unique features are no longer discernible. The resampled spectra may only capture general trends, such as broad absorption features, rather than the detailed characteristics necessary for accurate mineral identification.

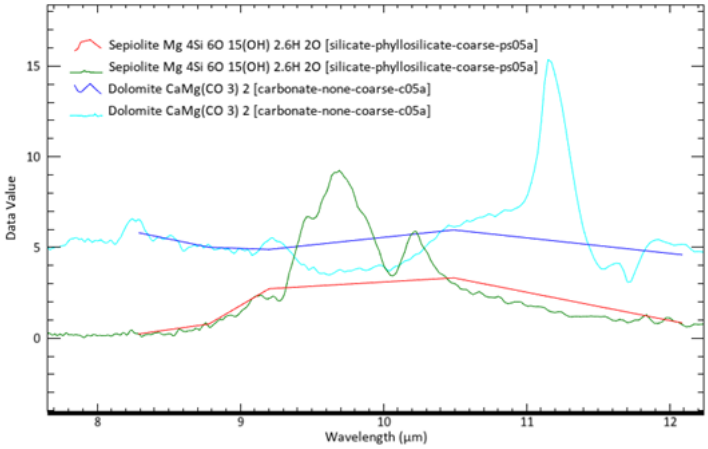

Figure 4.33: A comparison of the spectra of Sepiolite and Dolomite, selected from the Nicolet instrument data collection embedded in ENVI, was conducted before and after resampling. The results clearly show that significant data, including key characteristic features of the selected minerals, is lost during the resampling process

Accordingly, to address the limitations of the ECOSTRESS in terms of number of bands that probably leads to losing information if used for the detection of minerals, two band math approaches can be employed which are Using "Reference Tables" and "Logical Constraints."

4.2.3 ECOSTRESS Spectral Analysis-Reference Tables

When performing band math ratios, the goal is to identify and highlight a specific absorption or reflection feature within the data. . Unlike broadband ratio images, RBD images are highly specific, using spectral channels that define a single absorption feature. This method provides a local continuum correction[67], effectively addressing radiometric offsets and atmospheric absorption. RBD images are produced by summing channels from both absorption band shoulders and dividing them by the sum of channels from the absorption band minimum.[41] The shoulders refer to the points on either side of the feature where the signal stabilizes or shows consistent behavior. By applying this ratio, an image is generated where each pixel is assigned a value that reflects the strength or presence of the identified feature. The resulting image contains a range of pixel values that can be analyzed further. This ratio-based approach serves to normalize the data, providing a consistent basis for comparing pixels across the image. By normalizing, the comparison is not merely based on raw reflection or absorption values but rather on how these values relate to the expected behavior of the feature in question. The expected values are determined using the reflection data (y-axis values) from the resampled spectra, which have been adjusted to match the resolution of the imaging system. This normalization is crucial for accurately interpreting the band math results, especially when dealing with varying lighting conditions or other factors that could affect the raw data.

Once the band math has been applied to the resampled spectra, the resulting values can be compared to the pixel values in the band math image. If the calculated band math values from the resampled spectra overlap with the pixel values in the image, this alignment suggests that certain locations within the image may have a higher concentration of the feature being studied. These locations would appear more prominently, indicating areas where the feature is more abundant compared to others. This process helps in isolating and analyzing specific features across a geographic area or material sample. To better visualize the distribution and concentration of the feature, a raster color slice tool can be employed. This tool allows for the segmentation of the image into different color ranges based on the calculated band math values. By determining the exact ranges that correspond to different grain sizes or qualities of the feature, the tool can produce a clear and detailed representation of how the feature varies across the image.

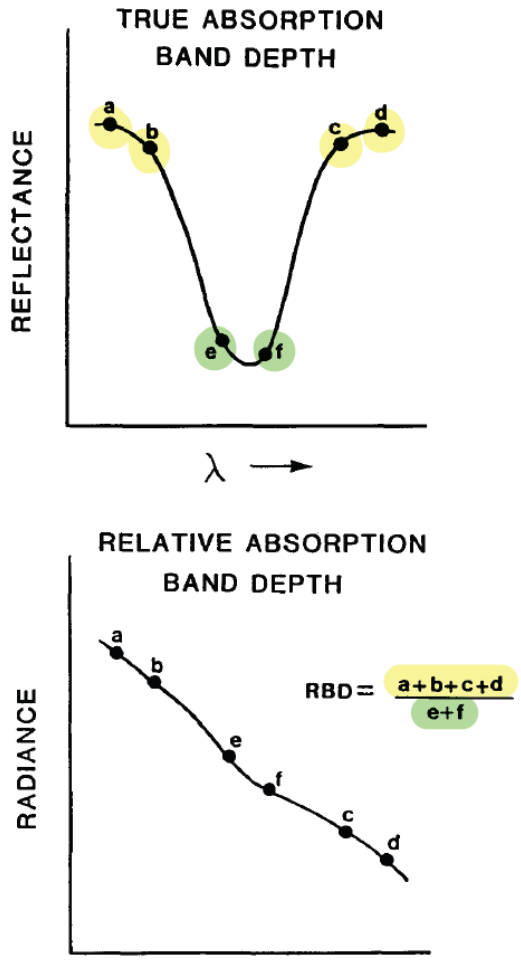

Figure 4.34: The relative absorption band-depth concept involves summing the digital numbers (DNs) of channels flanking an absorption band (on a per-pixel basis) and dividing this by the sum of DNs from channels near the band minimum. The upper diagram illustrates a hypothetical mineral reflectance spectrum, highlighting the channels necessary to determine the depth of the absorption feature. The lower diagram shows uncalibrated AIS data, where the radiometric curve is influenced by atmospheric absorption and solar radiance. By calculating the relative absorption band-depth, a local continuum correction is achieved, allowing mineral absorption features to be identified without requiring additional normalization procedures.

ECOSTRESS: Sepiolite Spectral Analysis using Reflectance Reference Tables

Range of pixel images [3.2454, 13.6050]is **not** consistent with the range that is calculated for 4 out of 5 bands with a center at band 4 [1.3732, 1.9215] .

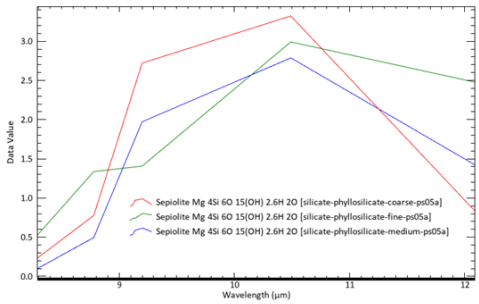

Figure 4.35: After resampling the spectra of Sepiolite from the Nicolet instrument to ECOSTRESS bands, four ECOSTRESS bands are consistently included in a common observed pattern.

Bands Used in Band Math for Sepiolite Detection	**b1**	**b2**	**b3**	**b4**	**b5**	**(b2+b3+b5)/b4**
Sepiolite $Mg_4Si_6O_{15}(OH)_2{\cdot}6H_2O$ (silicate_phyllosilicate_fine_ps05a)	0.5256	1.3367	1.4074	2.9908	2.4771	1.9215
Sepiolite $Mg_4Si_6O_{15}(OH)_2{\cdot}6H_2O$ (silicate_phyllosilicate_medium_ps05a)	0.0992	0.4959	1.9724	2.7872	1.4210	1.4310
Sepiolite $Mg_4Si_6O_{15}(OH)_2{\cdot}6H_2O$ (silicate_phyllosilicate_coarse_ps05a)	0.2332	0.7773	2.7211	3.3226	0.8311	1.3732

Table 4.13: Resampled Spectra Band Math values for detecting Sepiolite using ECOSTRESS bands1, 2, 3, 4, and 5, along with their reflectance values (y-axis) and the calculated ratio (b1+b2+b3+b5)/b4 for selected samples

Therefore, no place on the image is associated with sepiolite using this band math for ECOSTRESS.

ECOSTRESS: Dolomite Spectral Analysis using Reflectance Reference Tables

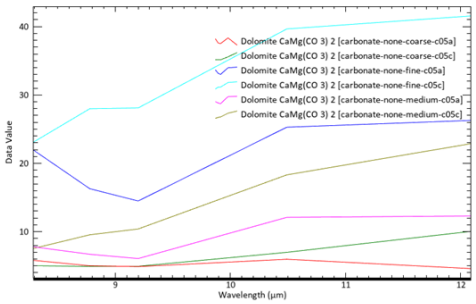

Figure 4.36: After resampling the spectra of Dolomites from the Nicolet instrument to ECOSTRESS bands, only 2 ECOSTRESS bands are consistently included in a common observed pattern.

Resampled mineral from Nicolet instrument to ECOSTRESS	b3	b4	Band Math Equation b4/b3
Dolomite CaMg(CO3)2 [Carbonate-None-fine-c05a]	14.48540	25.28450	1.74552
Dolomite CaMg(CO3)2 [Carbonate-None-fine-c05c]	28.10250	39.66030	1.41127
Dolomite CaMg(CO3)2 [Carbonate-None-Medium-c05a]	6.06620	12.09570	1.99395
Dolomite CaMg(CO3)2 [Carbonate-None-Medium-c05c]	10.3948	18.31020	1.76148
Dolomite CaMg(CO3)2 [Carbonate-None-Coarse-c05a]	4.88760	5.96380	1.22019
Dolomite CaMg(CO3)2 [Carbonate-None-Coarse-c05c]	4.93150	6.97720	1.41482

Table 4.14: Dolomite Reflectance Reference Table: After resampling the spectra of Dolomites from the Nicolet instrument to ECOSTRESS bands, only 2 ECOSTRESS bands are consistently included in a common observed pattern.

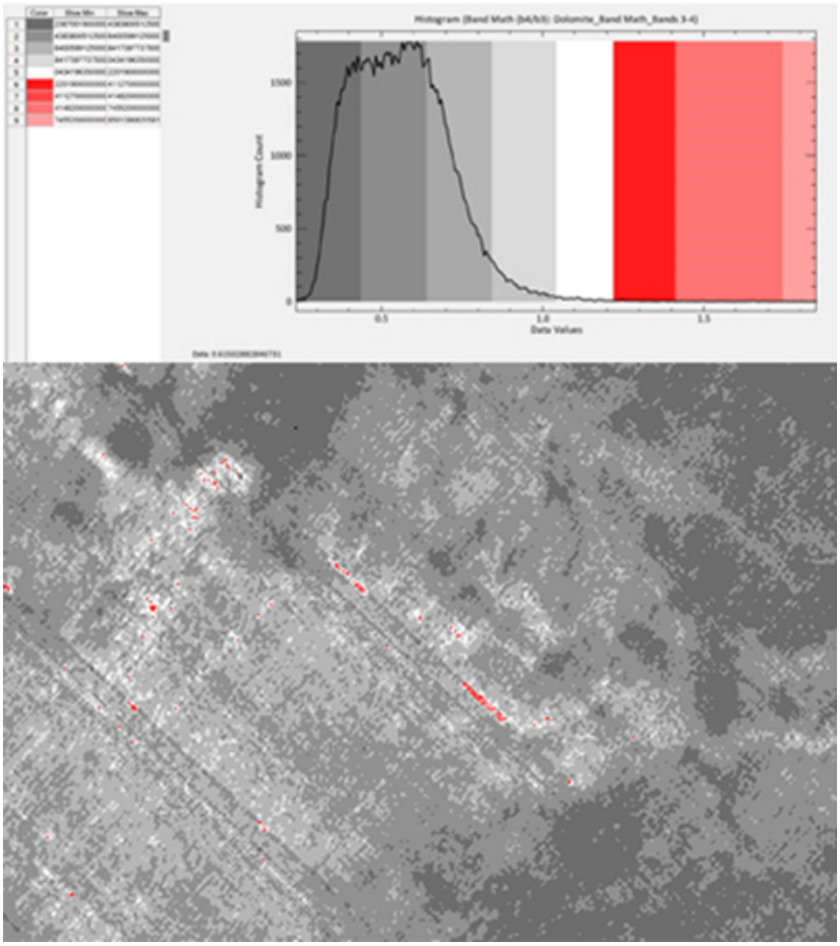

Figure 4.37: The raster color sliced image of the band math for Dolomites based on ECOSTRESS data.

ECOSTRESS: Apatite Spectral Analysis using Reflectance Reference Tables

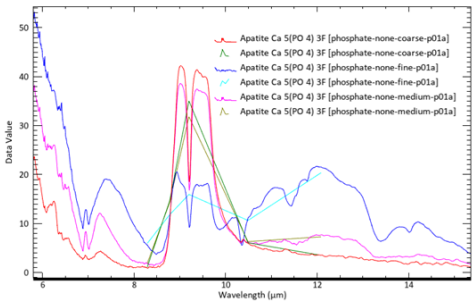

Figure 4.38: After resampling the spectra of Apatite from the Nicolet instrument to ECOSTRESS bands, 4 ECOSTRESS bands are consistently included in a common observed pattern.

Ecostress Bands for apatite with a repeating pattern	1	2	3	4	b3/(b1+b2+b4)
Apatite Ca5 (PO4)3F [Phosphate_None_Fine_p01a]	5.95000	11.82490	15.94810	10.64160	0.56123
Apatite Ca5 (PO4)3F [Phosphate_None_Medium_p01a]	1.88950	14.32820	31.83330	6.31710	1.41263
Apatite Ca5 (PO4)3F [Phosphate_None_Coarse_p01a]	1.12300	14.63460	35.04330	6.08050	1.60469

Table 4.15: Reflectance Reference Table for Apatite in TIR: Resampled Spectra Band Math values for detecting Apatite using ECOSTRESS bands 1,2,3 and 4, along with their reflectance values (y-axis) and the calculated ratio for selected samples

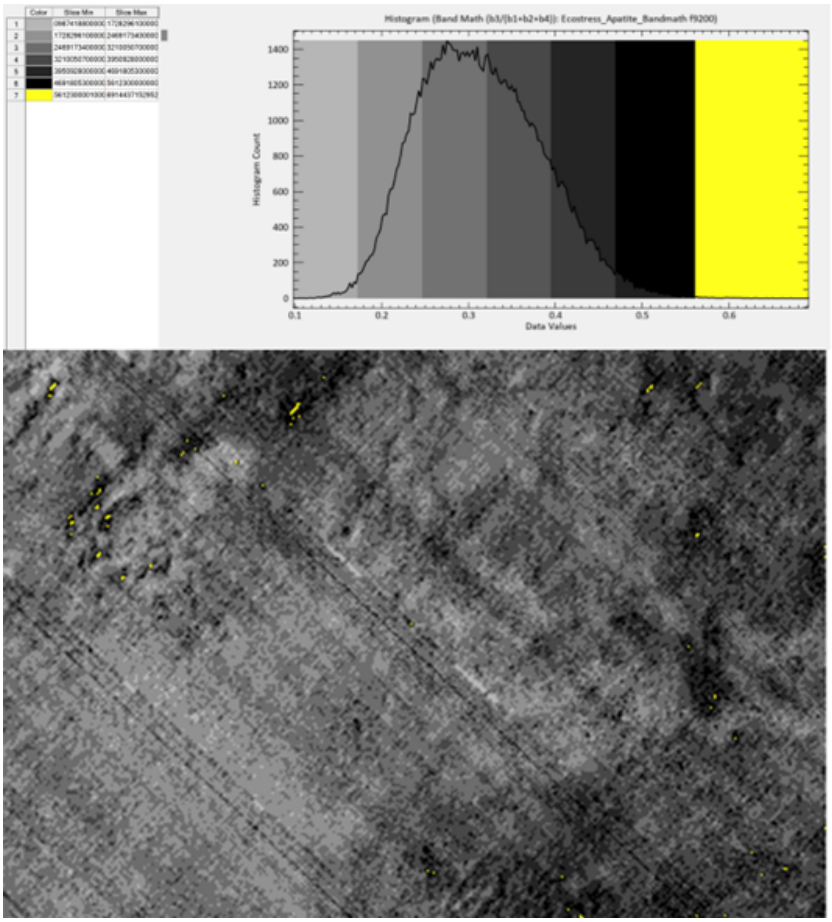

Figure 4.39: The raster color sliced image of the band math for apatite. Only reflections of this sample: Apatite Ca5 (PO4)3F [Phosphate_None_Fine_p01a] is within the range of "band math" which was calculated for resampled apatite that is shown is yellow color.

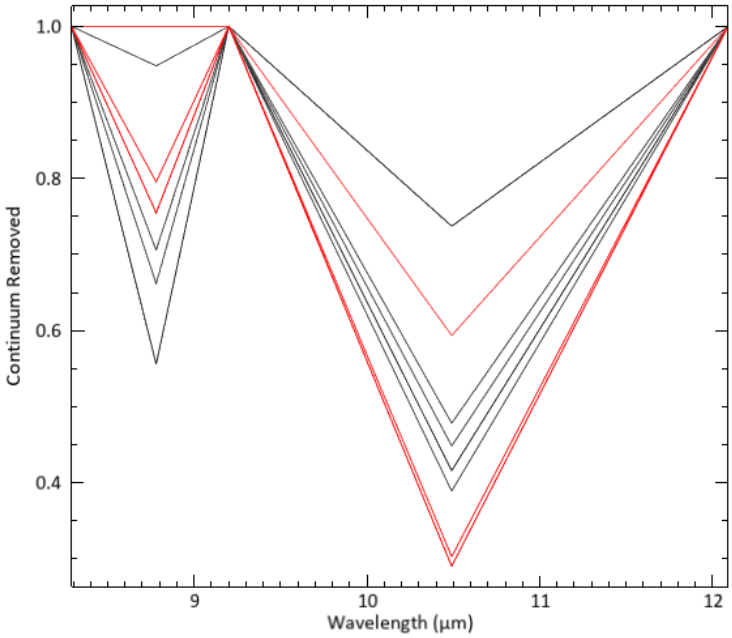

Figure 4.40: Comparison of the selected Apatite samples from the spectral library of ENVI(in red) with spectral profiles obtained from various points within the area of interest (in black) reveals similar patterns.

ECOSTRESS: Quartz Spectral Analysis using Reflectance Reference Tables

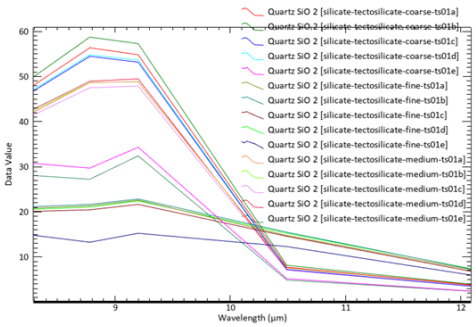

Figure 4.41: Quartz Samples in TIR: Fifteen Nicolet Samples of Quartz are selected from ENVI spectral library to find common patterns as a base for quartz detection

Ecostress Bands for Quartz with a repeating pattern	2	3	4	5	(b2+b4+b5)/b3
Quartz SiO2 [Silicate_Tectosilicate_Fine_ts01a]	21.34	22.6108	14.7769	7.1347	1.91287
Quartz SiO2 [Silicate_Tectosilicate_Fine_ts01b]	21.6569	22.8677	15.5071	7.3133	1.94498
Quartz SiO2 [Silicate_Tectosilicate_Fine_ts01c]	20.457	21.6588	14.5842	6.8036	1.93200
Quartz SiO2 [Silicate_Tectosilicate_Fine_ts01d]	21.0691	22.4413	15.2647	7.4193	1.94967
Quartz SiO2 [Silicate_Tectosilicate_Fine_ts01e]	13.274	15.2574	12.3056	5.9875	2.06897
Quartz SiO2 [Silicate_Tectosilicate_Medium_ts01a]	48.6534	48.8933	7.6164	3.8886	1.23040
Quartz SiO2 [Silicate_Tectosilicate_Medium_ts01b]	48.6534	48.8933	7.6164	3.8886	1.23040
Quartz SiO2 [Silicate_Tectosilicate_Medium_ts01c]	47.5152	47.9004	7.0805	3.562	1.21414
Quartz SiO2 [Silicate_Tectosilicate_Medium_ts01d]	48.9861	49.4889	7.0744	3.522	1.20396
Quartz SiO2 [Silicate_Tectosilicate_Medium_ts01e]	27.2281	32.4166	4.8793	2.3955	1.06436
Quartz SiO2 [Silicate_Tectosilicate_Coarse_ts01a]	56.3855	54.8271	7.7311	3.7478	1.23779
Quartz SiO2 [Silicate_Tectosilicate_Coarse_ts01b]	58.7481	57.3005	8.1538	3.9604	1.23668
Quartz SiO2 [Silicate_Tectosilicate_Coarse_ts01c]	54.4785	53.2001	7.2411	3.4982	1.22590
Quartz SiO2 [Silicate_Tectosilicate_Coarse_ts01d]	54.8067	53.6867	7.2464	3.4983	1.22100
Quartz SiO2 [Silicate_Tectosilicate_Coarse_ts01e]	29.7068	34.3352	5.1895	2.4318	1.08717

Table 4.16: Resampled Spectra Band Math values for detecting Quartz using ECOSTRESS bands 2,3, 4 and 5 along with their reflectance values (y-axis) and the calculated ratio for 15 particle sizes and types of quartz (fine, medium, coarse).

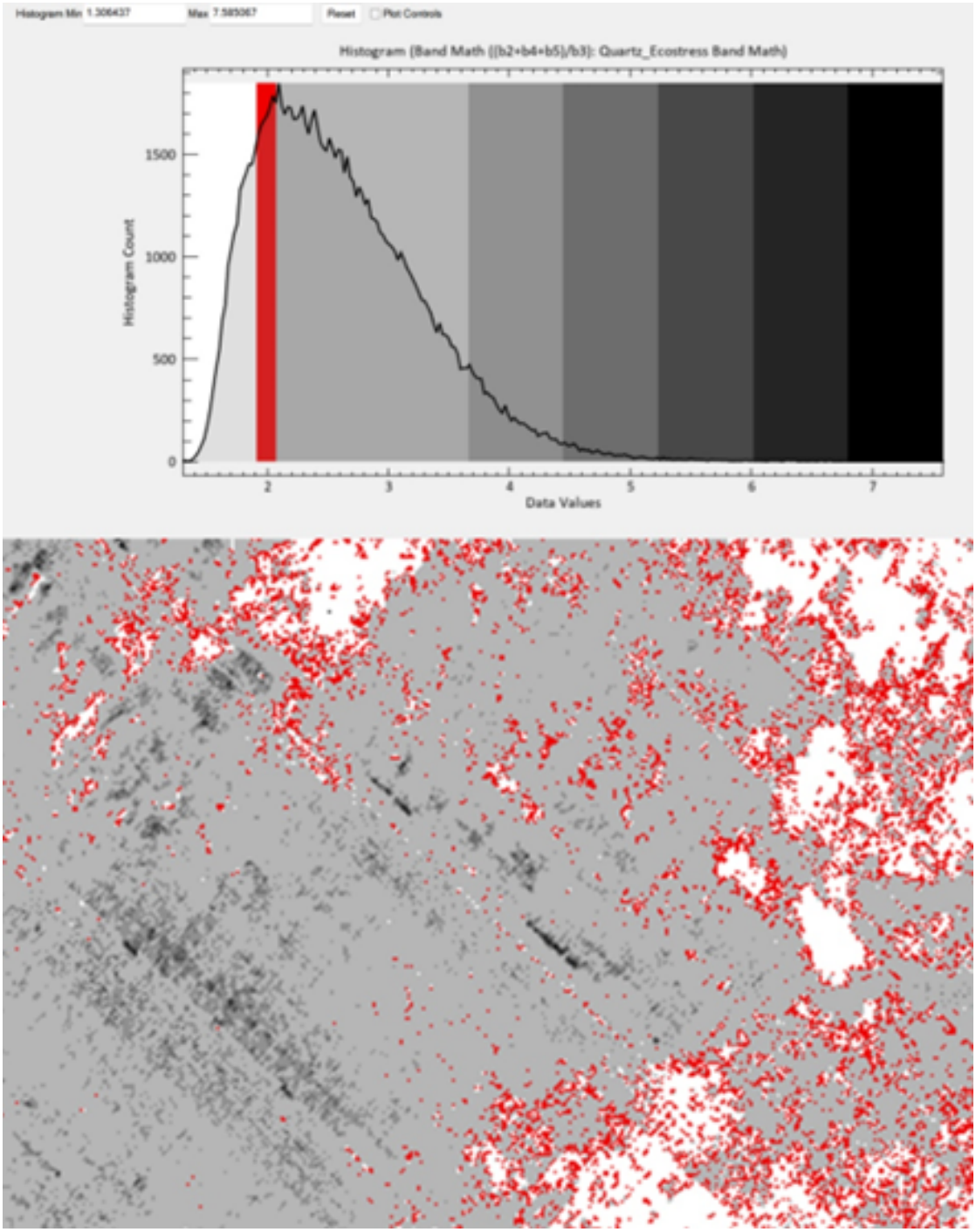

Figure 4.42: The raster color-coded image of the band math for quartz displays pixel values in the "red" range [1.91287, 2.06897], indicating possible quartz in the area

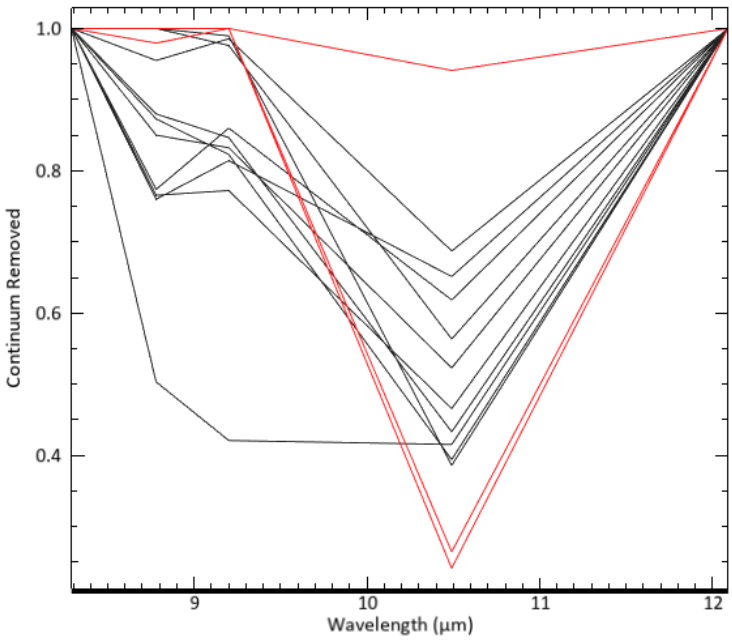

Figure 4.43: Comparison of the selected Quartz samples from the spectral library of ENVI(in red) with spectral profiles obtained from various points within the area of interest (in black) reveals similar patterns.

ECOSTRESS: Calcite Spectral Analysis using Reflectance Reference Tables

In the analysis of calcite samples, nine samples were chosen from the ASTER spectral library and the Nicolet spectrometer. Initially, it may be challenging to discern any obvious patterns among the samples. However, upon closer examination, a noticeable trend emerges: samples within the same category—specifically, the fine a, coarse a, and medium a groups—exhibit similar spectral patterns. To facilitate a more straightforward comparison, these samples are grouped into three distinct categories based on their shared characteristics. This grouping approach simplifies the analysis by highlighting the commonalities within each group, making it easier to identify and compare the spectral properties of calcite across different sample sets.

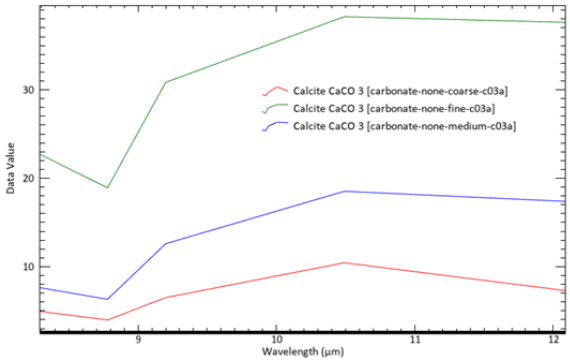

Figure 4.44: The resampled spectra for fine, medium, and coarse categories, specifically c03a, reveal similar patterns.

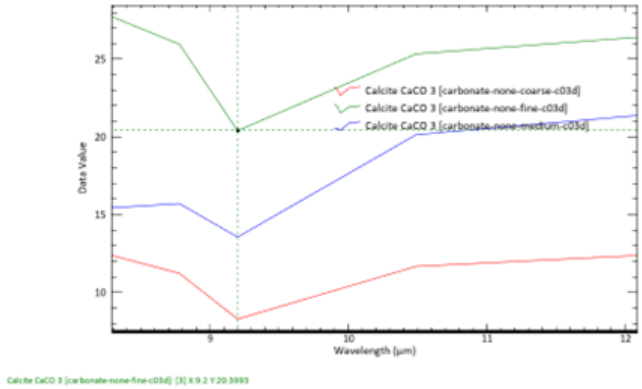

Figure 4.45: The resampled spectra for fine, medium, and coarse categories, specifically c03d, reveal similar patterns.

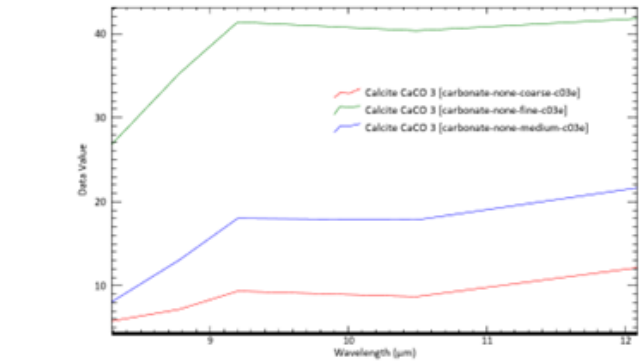

Figure 4.46: The resampled spectra for fine, medium, and coarse categories, specifically c03e, reveal similar patterns.

Calcite resamples of 1st category: fine, medium, and coarse [c03a]	band 1	band 2	band 3	band 4	band 5	(b1+b3+b4/b2)
Calcite CaCO3 [Carbonate_none_fine_c03a]	22.70980	18.91300	30.83750	38.26220	Not Relevant	4.04273
Calcite CaCO3 [Carbonate_none_Medium_c03a]	7.62150	6.31110	12.59670	18.52060	Not Relevant	5.08283
Calcite CaCO3 [Carbonate_none_Coarse_c03a]	4.94450	3.97480	6.50150	10.44130	Not Relevant	4.42660

Calcite Samples from Nicolet	band 1	band 2	band 3	band 4	band 5	(b1+b2+b4+b5)/b3
Calcite CaCO3 [Carbonate_none_fine_c03d]	27.73490	25.95310	20.39930	25.34080	26.40480	5.16849
Calcite CaCO3 [Carbonate_none_Medium_c03d]	15.43790	15.70820	13.55780	20.14070	21.38020	5.35979
Calcite CaCO3 [Carbonate_none_Coarse_c03d]	12.38330	11.22350	8.28210	11.67350	12.37320	5.75379

Calcite Samples from Nicolet	band 1	band 2	band 3	band 4	band 5	b3/(b1+b2+b4)
Calcite CaCO3 [Carbonate_none_fine_c03e]	26.82070	35.26950	41.37080	40.34070	Not Relevant	0.40389
Calcite CaCO3 [Carbonate_none_Medium_c03e]	8.08120	13.07790	18.01480	17.82610	Not Relevant	0.46209
Calcite CaCO3 [Carbonate_none_Coarse_c03e]	5.79510	7.20020	9.35580	8.70560	Not Relevant	0.43112

Table 4.17: Resampled Calcites band math for quality 'a', 'd' and 'e' of different particle sizes

It should be noted that the naming convention (a, d, e) indicates the purity of the mineral sample. Therefore, it is possible that quality "d" or "e" Calcite is not pure calcite; contamination by the presence of other minerals may occur. Consequently, what is being observed may or may not accurately represent calcite.

1st category of calcite: fine, medium and coarse, c03a

Resampled quality 'a' Quartz from Nicolet to ECOSTRESS has a range of [4.04273, 5.08283], but the image values of band math fall within the range [0.380718, 1.672620]. This discrepancy indicates that the band math image values do not align with the expected range for quality 'a' Quartz, suggesting that this mineral type is not detected within the current image data. As a result, the specific quality 'a' Quartz may be absent or not distinguishable based on the resampled data.

2nd category of calcite: fine, medium and coarse, c03d

For the resampled Calcite of quality "d" from Nicolet to ECOSTRESS across different particle sizes, the band math values fall within the range of [5.1689, 5.75379]. This specific range is fully contained within the broader image range of [1.90165, 13.52157], which indicates that the quality "d" Calcite can be accurately identified and distinguished within the dataset. The alignment of these ranges suggests that the spectral characteristics of quality "d" Calcite are preserved during the resampling process, allowing for effective detection and mapping within the image.

To visualize and highlight this detection, a raster color slice is applied to the image. By isolating the band math values corresponding to the range of quality "d" Calcite, the areas where this mineral is present are clearly delineated. These regions

are then colored in red, making it easy to identify the spatial distribution of quality "d" Calcite within the area of interest. This method enhances the interpretability of the data, providing a clear visual representation of where quality "d" Calcite is located based on the resampled spectra.

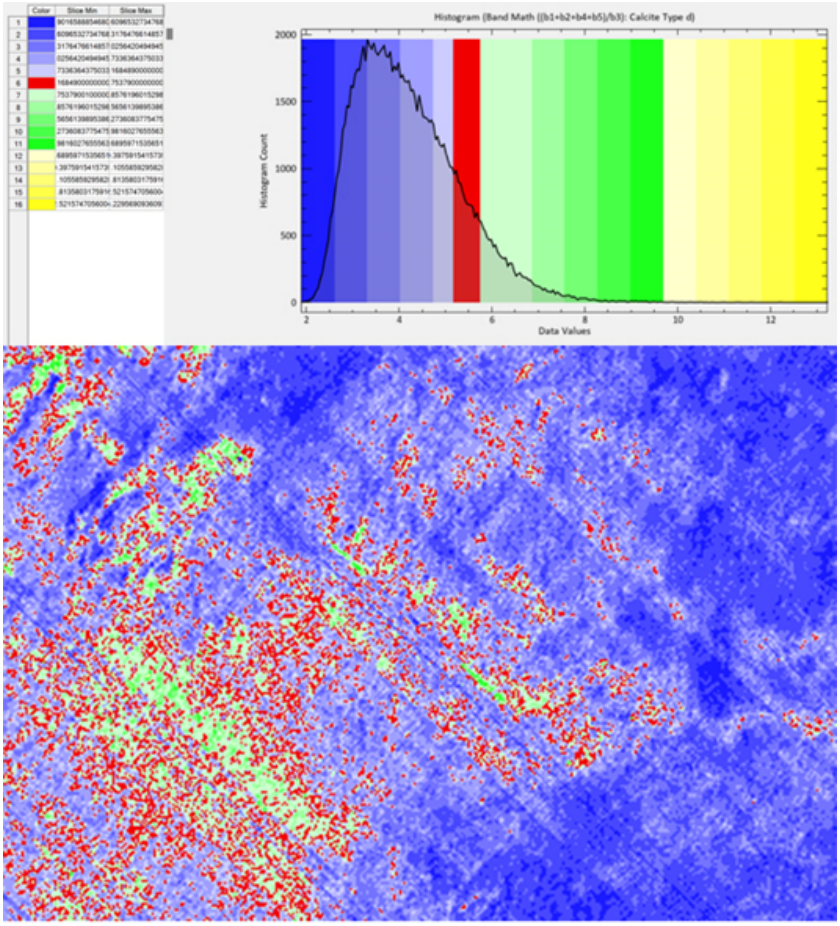

Figure 4.47: Quality 'd' Calcite is detected within the band math range [5.1689, 5.75379], fully contained in the image range [1.90165, 13.52157], and highlighted in red after raster color slicing.

3rd category of calcite: fine, medium and coarse, c03e

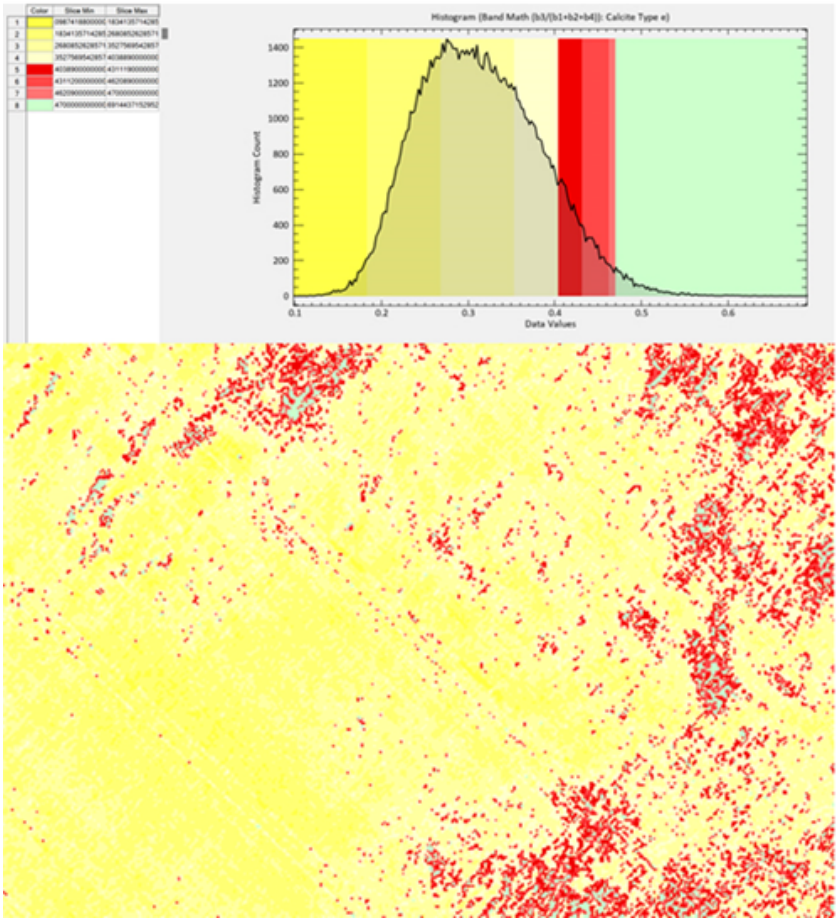

Figure 4.48: Quality 'e' Calcite is detected within the band math range [0.40389, 0.46209], fully contained in the image range [0.09874, 0.69144], and highlighted in shades of red after raster color slicing.

ECOSTRESS: Gypsum Spectral Analysis using Reflectance Reference Tables

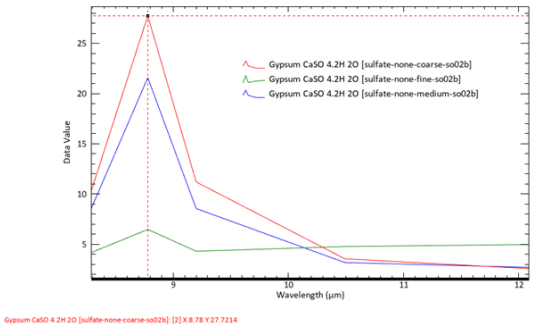

Figure 4.49: Reflectance Reference Table for Gypsum in TIR: The resampled and not resampled spectra for fine, medium, and coarse Gypsums showing similar patterns.

Ecostress Bands for Gypsum from the Library of Nicolet	1	2	3	4	5	(b1+b3+b4+b5)/(b2)
Gypsum CaSO4.2H2O [Sulfate_None_Fine_so02b]	4.1851	27.7214	11.2029	4.7857	3.9826	0.87140
Gypsum CaSO4.2H2O [Sulfate_None_medium_so02b]	8.577	21.5779	8.562	3.1919	2.7086	1.06774
Gypsum CaSO4.2H2O [Sulfate_None_coarse_so02b]	10.3325	6.4878	4.3151	3.5655	2.5875	3.20611

Table 4.18: Resampled Spectra Band Math values for detecting Gypsums using ECOSTRESS bands 1,2 and 3, along with their reflectance values (y-axis) and the calculated ratio for different particle grain sizes (fine, medium, coarse).

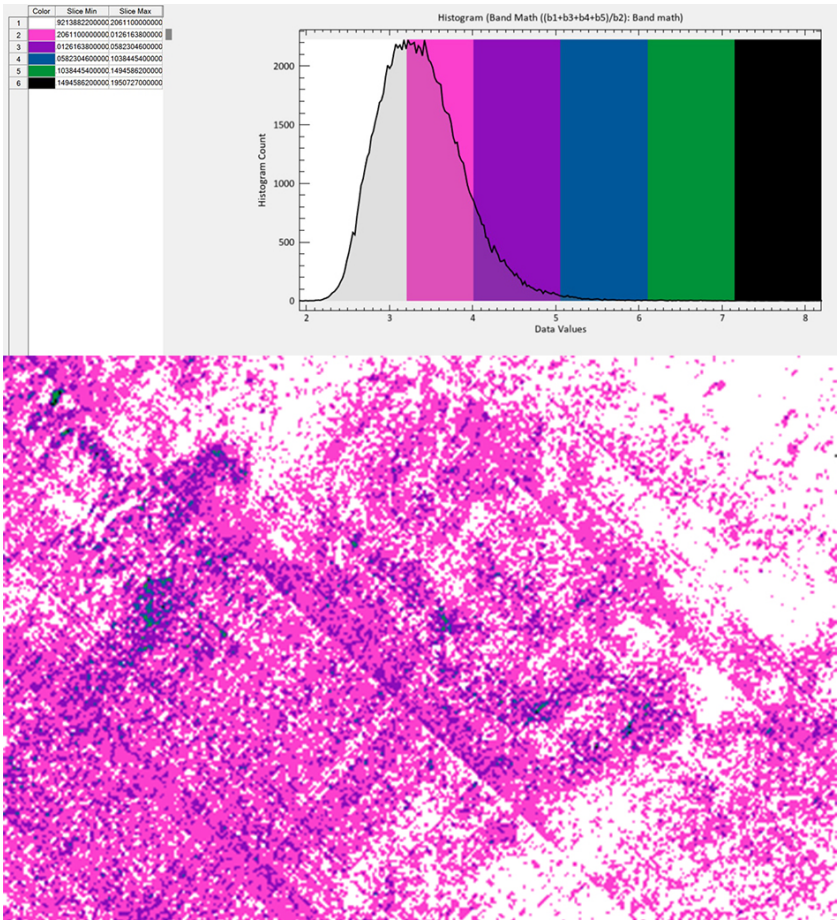

Figure 4.50: Raster color-sliced image of the band math with corresponding histogram, highlighting the broad geographical dispersion of gypsum (White Color) within the calculated spectral range

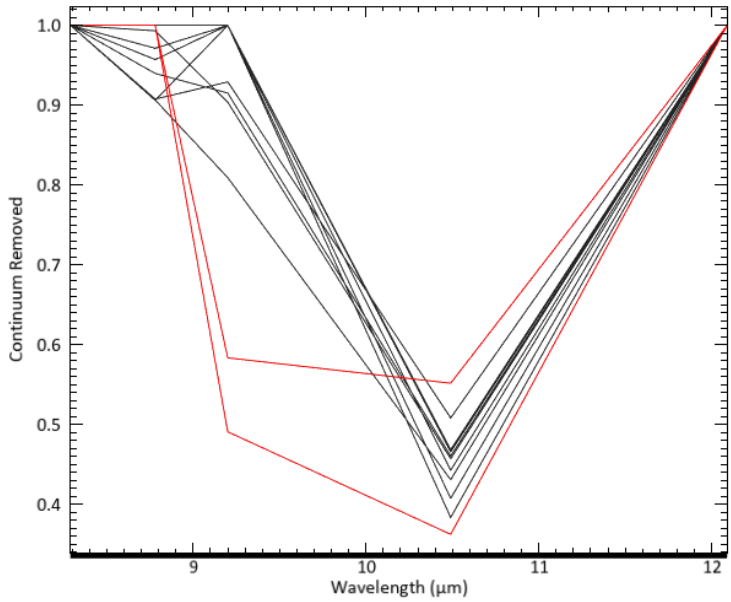

Figure 4.51: Comparison of the selected Gypsum samples from the spectral library of ENVI(in red) with spectral profiles obtained from various points within the area of interest (in black) reveals similar patterns.

ECOSTRESS: Illite Spectral Analysis using Reflectance Reference Tables

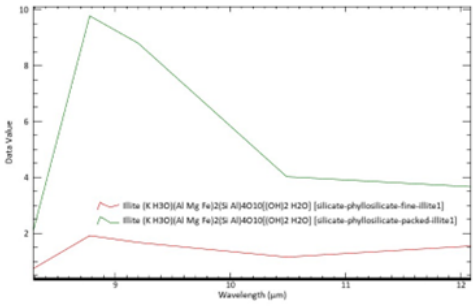

Figure 4.52: Reflectance Reference Table: The resampled spectra for fine and packed Illite-Smectite showing similar patterns.

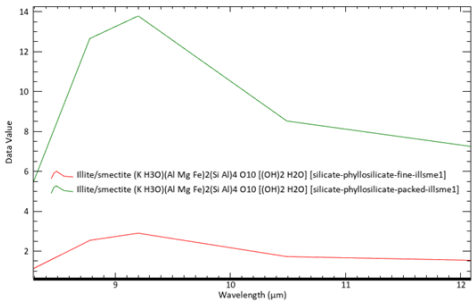

Figure 4.53: Reflectance Reference Table: The resampled spectra for fine and packed Illite showing similar patterns.

The geographical distribution of illite/smectite in the Youssoufia region has been analyzed, focusing on both fine and packed grain sizes. The band math values for the resampled spectra, which range from [1.2391, 1.2466], fall within the broader range of image pixel values, spanning [0.3301, 1.6768]. This specific range [1.2391, 1.2466] is associated with illite/smectite, particularly the fine-grained variety, characterized by the chemical formula (K H_3O)$(AlMgFe)_2(SiAl)_4O_{10}[(OH)_2H_2O]$ [Silicate_Phyllosilicate_fine_Illsme1].

However, pixel values exceeding 1.2466 may indicate the presence of packed illite/smectite. Since there is no clearly defined upper limit for these higher values, it becomes challenging to accurately represent the packed grain size distribution based solely on the initial data range. To address this, a +5% value adjustment is

Ecostress Bands for Illite (Pattern)	Band 1	Band 2	Band 3	Band 4	Band 5	(b2+b3)/(b1+b4)
Illite Fine	0.7345	1.9148	1.6702	4.0231	NR	0.4653
Illite Packed	2.0860	9.7788	8.8050	1.1477	NR	1.1921
Ecostress Bands for Illite/Smectite (Pattern)	**Band 1**	**Band 2**	**Band 3**	**Band 4**	**Band 5**	**(b2+b3)/(b1+b4+b5)**
Illite/Smectite Fine	1.1235	2.5406	2.9003	1.7260	1.5416	1.2391
Illite/Smectite Packed	5.4458	12.6576	13.7922	8.5241	7.2476	1.2466

Table 4.19: Ecostress bands for Illite and Illite/Smectite with respective spectral patterns and calculated ratios for different grain sizes.

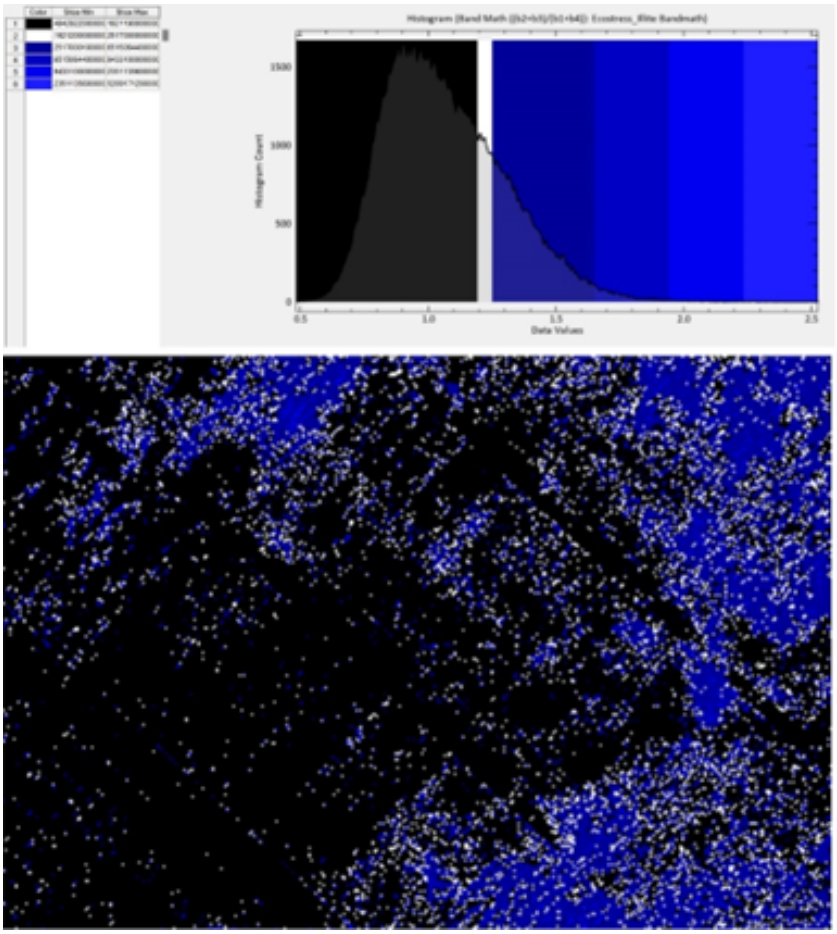

Figure 4.54: The geographical distribution of Illite obtained after applying the band math for it

applied to the packed grain size illite/smectite, providing a more plausible range to illustrate its potential distribution.

This adjustment allows for a more comprehensive depiction of the geographical distribution of illite/smectite in the region, considering both fine and packed grain

sizes.

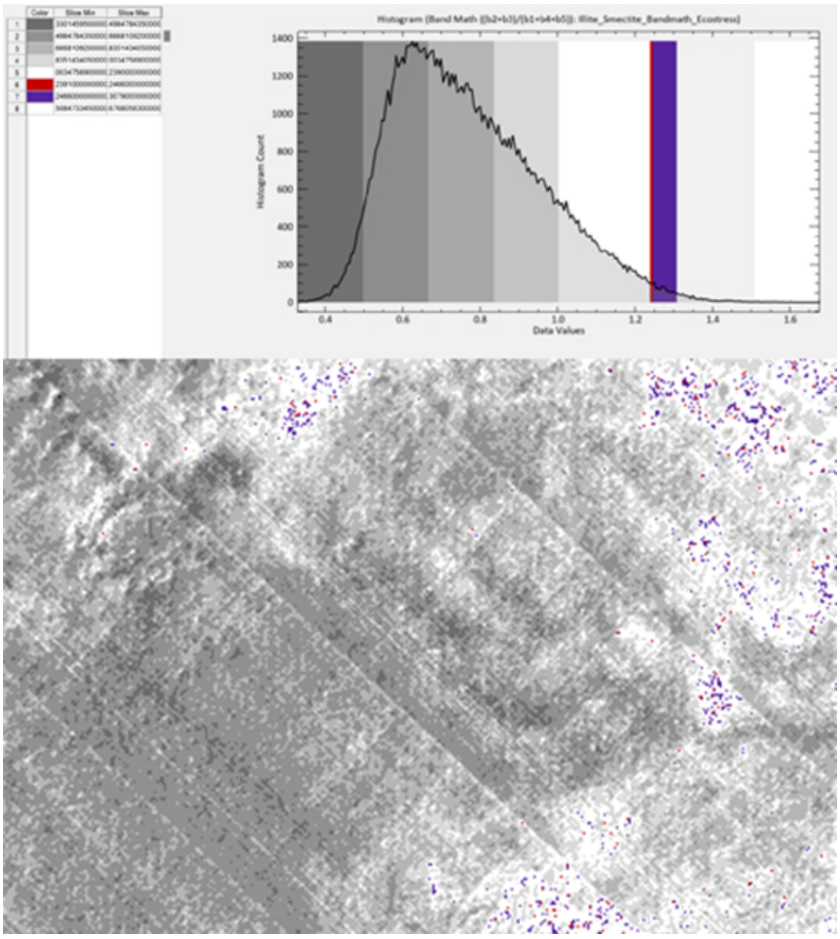

Figure 4.55: Raster color-sliced image and histogram showing the geographical distribution of fine and packed grain size illite/smectite in the Youssoufia region. The image highlights the adjusted pixel values to account for both fine and packed varieties, using a +5% **Stretch Value** to better represent the probable distribution.

ECOSTRESS: Kaolinite Spectral Analysis using Reflectance Reference Tables

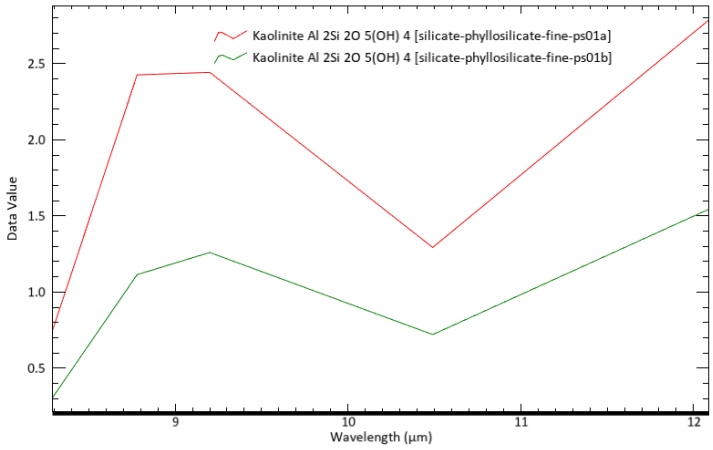

Figure 4.56: After resampling the spectra of Kaolinite from the Nicolet instrument to ECOSTRESS bands, 5 ECOSTRESS bands are consistently included in a common observed pattern.

Ecostress Bands for Kaolinite (Pattern)	Band 1	Band 2	Band 3	Band 4	Band 5	(b2+b3+b5)/(b1+b4)	Pixel Value Range
Kaolinite Fine (ps01a)	0.7456	2.4246	2.4429	1.2924	2.7884	3.7566	0.7113
Kaolinite Fine (ps01b)	0.3059	1.1144	1.2594	0.7204	1.5450	3.8184	3.3942

Table 4.20: Reflectance Reference Table for Kaolinite in TIR: Resampled Spectra Band Math values for detecting Kaolinite using ECOSTRESS bands 1,2,3,4 and 5 along with their reflectance values (y-axis) and the calculated ratio for fine particle grain sizes

Finally, the grayscale image of the band math for kaolinite was analyzed. Since there is no overlap between the range calculated for the resampled spectra and the pixel values, no conclusions can be drawn regarding the locations of fine dolomite within the area of interest.

4.2.4 ECOSTRESS Spectral Analysis-Logical Constraints Approach

I In this approach, after selecting and resampling a group of minerals, their common spectral patterns are closely examined. These patterns are analyzed to identify distinctive characteristics that can be used to differentiate the minerals from one another. The goal is to formulate these spectral patterns using logical operations such as "AND", "OR" and other similar operators. By applying these logical operations, one can create a set of conditions that describe the presence or absence of specific minerals based on their spectral signatures.

Once the logical conditions have been established, they are applied to the study image through a process known as band math. Band math, in this context, systematically checks each cell (or pixel) in the image against the logical conditions derived from the resampled spectra. This cell-by-cell analysis allows for the identification of the spectral patterns that correspond to the minerals being studied. The conditions are meticulously evaluated for every pixel to determine whether the spectral data at that location matches the expected patterns of the minerals.

This process results in the creation of a Boolean or binary image, where each pixel is assigned a value of either 0 or 1 based on whether it satisfies the provided logical conditions. A Boolean image is an image where each pixel can only have one of two possible values, typically representing binary states like black and white or 0 and 1. This type of image is often referred to as a binary image. In a Boolean or binary image: • 1 or true might represent white or the presence of a feature. • 0 or false might represent black or the absence of a feature. These images are used in various applications, such as edge detection, image segmentation, and pattern recognition, where the presence or absence of specific features is important. In the binary image, a pixel value of 0 indicates that the pixel does not meet the logical conditions for the resampled spectra of the mineral being analyzed. In other words, the spectral characteristics of that pixel do not match the expected patterns for the mineral, suggesting that the mineral is not present at that location. Conversely, a pixel value of 1 indicates that the pixel satisfies the logical conditions, meaning that the spectral data aligns with the patterns of the mineral in question, and thus, the mineral is likely present at that location.

This binary image provides a clear and straightforward way to visualize the distribution of the mineral across the study area. By performing band math and checking the conditions cell by cell, the approach ensures a precise identification of the mineral's presence, effectively mapping out areas where the mineral patterns are detected. This systematic method reduces the likelihood of false positives or negatives, offering a powerful tool for geologists and researchers to quickly and accurately identify areas of interest for further exploration and analysis.

Identifying Dolomite and Sepiolite by Developing logical constraints

To identify the presence of dolomite and sepiolite in satellite or spectral imagery, a distinct reflection pattern is utilized. Specifically, both dolomite and sepiolite exhibit higher reflection values in band 4 compared to band 3, which allows for their differentiation from other minerals. The following steps outline the methodology for using this feature:

Data Acquisition: Obtain the band values for the study area by analyzing spectral imagery. This involves acquiring images that contain the necessary band data, particularly band 3 and band 4, from a remote sensing instrument.

Ratio Calculation: Calculate the ratio of the reflection values by dividing the amount of light reflected in band 4 by the amount reflected in band 3. Mathematically, this is represented as: Ratio=B4/B3

Ratio Evaluation: Check whether the calculated ratio is greater than 1. If the ratio exceeds 1, the sample likely contains dolomite or sepiolite. This serves as the key indicator for identifying these minerals.

Band Math Application: Based on the common feature of dolomite and sepiolite, perform band math to enforce the logical condition: B4/B3>1 This equation filters out areas where the reflection pattern aligns with the expected characteristics of dolomite and sepiolite.

Raster Color Slice: Once the logical condition is applied, generate a raster image to visualize the result. Pixels that meet the condition (i.e., ratio > 1) are assigned a value of 1, while those that do not meet the condition are assigned a value of 0. This results in a binary or Boolean image where the detected mineral patterns are highlighted.

Since these patterns might be sparse, the image can appear predominantly black (with 0 values). To improve visibility, apply a raster color slicing technique, assigning distinct colors to highlight the pixels that meet the condition. This method enhances the differentiation of the minerals, making it easier to identify areas where dolomite or sepiolite is present.

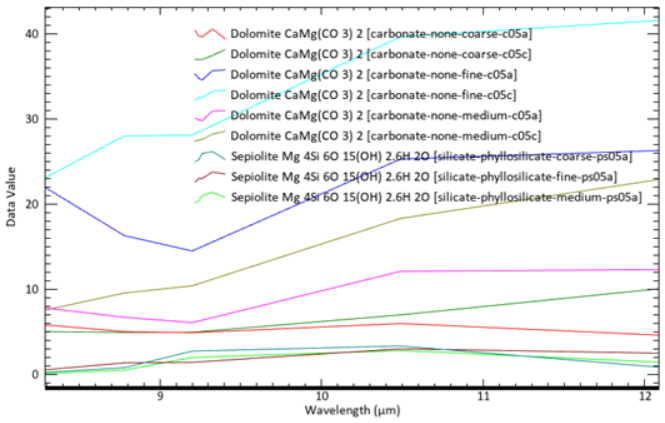

Figure 4.57: For both dolomite and sepiolite, the amount of reflection in band 4 is greater than the light reflected in band 3. This means that if we measure the ratio of the reflection in band 4 to band 3, it will be greater than 1. Not to mention that this condition, differentiates these two minerals from others in the selection.

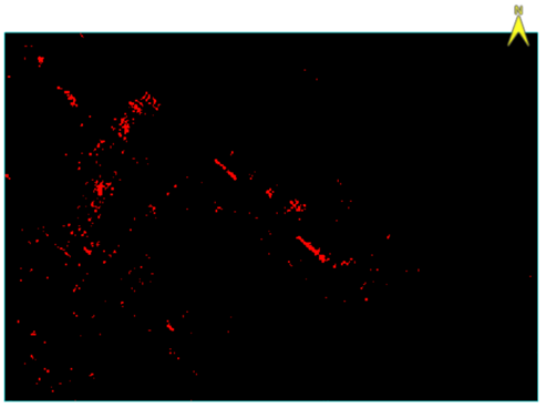

Figure 4.58: Probable Sepiolite and Dolomite Distribution in the Area of Interest: Raster Color Slice Tool Applied to Highlight Band Math Based on Common Reflection Features

Identifying Quartz by Developing logical constraints

As shown in Figure 4.41 ,To characterize the peak shape in the quartz spectra across bands 2, 3, and 4, the variation in slope is represented through a simple multiplicative condition:

$$(b_3 - b_2) \times (b_2 - b_1) \times (b_4 - b_3) > 0$$

For further refinement, additional constraints related to the specific values of the bands are applied to this initial condition, enhancing the robustness of the results.

The logical condition for the quartz spectral pattern (Equation 3) is expressed as:

$$(b_3 - b_2) \times (b_2 - b_1) \times (b_4 - b_3) > 0 \quad \text{and} \quad b_3 > b_1 \quad \text{and} \quad b_1 > b_2 \quad \text{and} \quad b_2 > b_4 \tag{4.1}$$

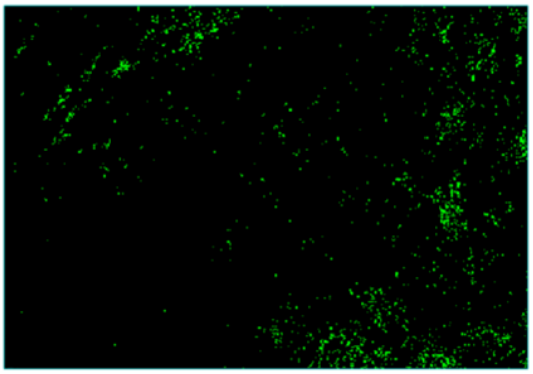

Figure 4.59: Detection of quartz in the area of interest using band math and logical conditions. Points satisfying the condition are highlighted in green.

Identifying Apatite by Developing logical constraints

As illustrated in Figure 4.38, the detection of apatite is based on a specific logical condition applied to the spectral bands. The condition is formulated as:

$$\begin{aligned} (b_3 - b_2) \times (b_2 - b_1) \times (b_4 - b_3) < 0 \quad & \text{and} \\ b_3 > b_2 \quad & \text{and} \\ b_2 > b_1 \quad & \text{and} \\ b_2 > b_4 \quad & \text{and} \\ b_4 > b_1 \quad & \end{aligned} \tag{4.2}$$

This condition highlights the characteristic pattern of apatite, capturing the relationships between the band values to identify its spectral signature effectively.

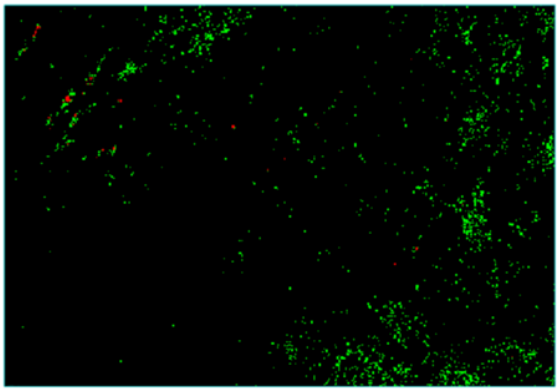

Figure 4.60: The image resulted from applying a logical constraint on the image of the Youssoufia area to depict quartz (green) and apatite (red)

Identifying Kaolinite by Developing logical constraints

According to resampled kaolinite for ECOSTRESS (image **??**), the detection of kaolinite is based on the following logical condition:

$$(B_2 - B_1) \times (B_3 - B_2) \times (B_4 - B_3) < 0 \quad \text{and} \quad B_2 > B_1 \quad \text{and} \quad B_4 < B_3$$
$$(B_4 - B_3) \times (B_5 - B_4) < 0 \quad \text{and} \quad B_4 < B_5 (4.3)$$

This condition captures kaolinite's spectral pattern characteristic by analyzing the bands' relationships. Figure 4.61 displays the resulting image, where the points satisfying these conditions through band math are visualized.

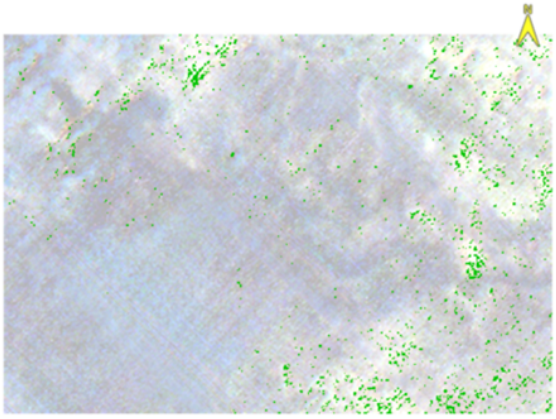

Figure 4.61: The resulting image of the conditions met in band math for Kaolinite (green)

Identifying Gypsum by Developing logical constraints

The logical constraint for detecting the spectral pattern of gypsum is provided in Equation 6 as follows:

$$\begin{aligned}(B_2 - B_1) \times (B_3 - B_2) \times (B_4 - B_3) < 0 \quad &\text{and} \\ B_2 > B_1 \quad &\text{and} \\ B_4 < B_3 \quad &\text{and} \\ (B_4 - B_3) \times (B_5 - B_4) < 0 \quad &\end{aligned} \tag{4.4}$$

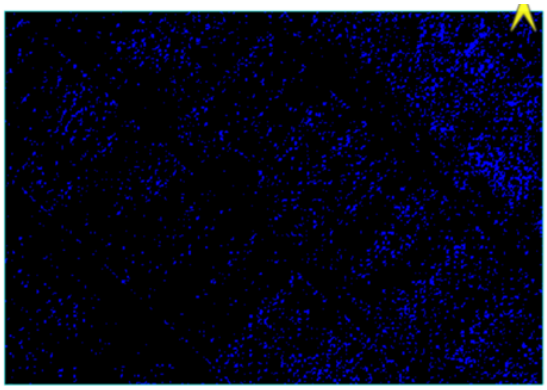

Figure 4.62: The image produced by applying a logical constraint to the Youssouffia area dataset in an attempt to detect gypsum yielded very poor results.

Identifying Illite by Developing logical constraints

The image obtained for illite shows an unexpectedly widespread distribution of this mineral, which seems unlikely based on current geological understanding. Also, Introducing conditions to binary image data, results in values falling between 0 and 1. This can occur due to mathematical operations, logical operations, thresholding difficulties, noise, and data representation limitations. Consequently, maintaining a strict binary output after applying conditions can be challenging and requires careful consideration of the specific data and operations involved.

Based on the resampled spectra of illite 4.52, the logical condition for identifying the spectral pattern of illite is defined as:

$$((B_2 - B_1) \times (B_3 - B_2) \times (B_4 - B_3) < 0) \quad \text{and} \quad ((B_2 - B_1) \times (B_3 - B_2) > 0) \tag{4.5}$$

This condition captures the necessary relationships between the spectral bands to effectively distinguish the presence of illite.

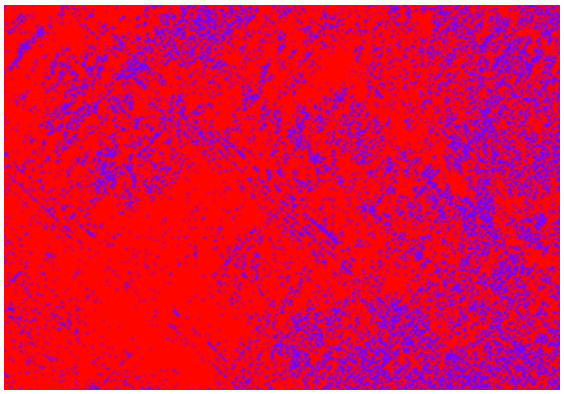

Figure 4.63: The Binary/Boolean image obtained by applying the logical condition for Illite in band math.

The image obtained for illite shows an unexpectedly widespread distribution of this mineral, which seems unlikely based on current geological understanding. Also, Introducing conditions to binary image data, results in values falling between 0 and 1. This can occur due to mathematical operations, logical operations, thresholding difficulties, noise, and data representation limitations. Consequently, maintaining a strict binary output after applying conditions can be challenging and requires careful consideration of the specific data and operations involved.

Chapter 5

Conclusion

5.1 Comparative Maps

5.1.1 Carbonates: Dolomites and Calcite

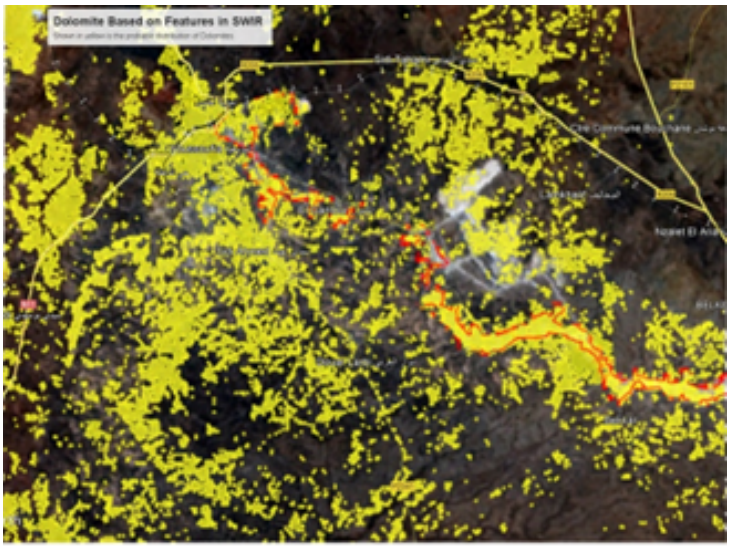

Mapping of Dolomites in SWIR using EMIT sensor

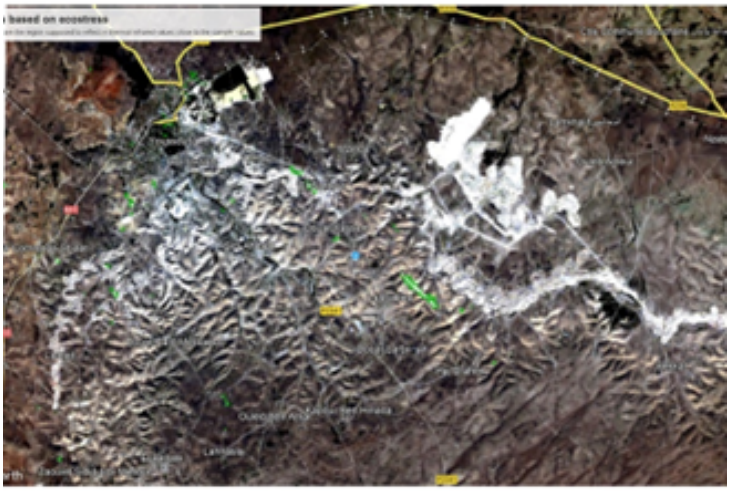

Mapping of Dolomites in TIR using ECOSTRESS sensor

Figure 5.1: Comparison of results of SWIR and TIR analysis for Dolomite

SWIR (Shortwave Infrared)

- **Absorption Bands:** Dolomites exhibit characteristic absorption bands in the SWIR region, particularly around 2320 nm. These bands are influenced by the presence of carbonate ions and can help distinguish dolomite from other carbonates like calcite, which has absorption bands around 2340 nm [**camargo2023**].
- **Chemical Composition:** Variations in the chemical composition, such as the substitution of Ca^2 and Mg^2 by Fe^2, can affect the spectral signatures in this region [**camargo2023**].

The differences in calcite mapping results using SWIR (Short-Wave Infrared) and TIR (Thermal Infrared) spectral analysis can be attributed to several factors:

1. **Spectral Sensitivity:** SWIR and TIR sensors detect different wavelengths, which means they interact with calcite in distinct ways. SWIR is sensitive to the vibrational overtones and combinations of molecular bonds, while TIR detects the fundamental vibrations of the crystal lattice [**zaini2012**].

2. **Grain Size and Mineral Mixtures:** The grain size of calcite and the presence of other minerals can affect the absorption features in both the SWIR and TIR regions. For instance, finer grains might show different spectral characteristics compared to coarser grains [**zaini2012**].

3. **Surface Temperature and Emissivity:** TIR data is influenced by surface temperature and emissivity variations, which can cause discrepancies in the detection of calcite compared to SWIR data, which is less affected by these factors [**ali2024**].

4. **Sensor Resolution:** The spatial resolution of the sensors might differ, leading to variations in the detail and accuracy of the mapping results [**khan2020**].

5. **Different Spectrometers, Different Samples:** Using samples and resamples from different spectral libraries can cause discrepancies in mineral mapping results. This is due to variations in instrument calibration, spectral resolution, and the conditions under which samples were measured. Additionally, interpolation and resampling methods can introduce discrepancies, and different instruments might add unique noise patterns or artifacts. These factors can affect the consistency and accuracy of spectral analysis.

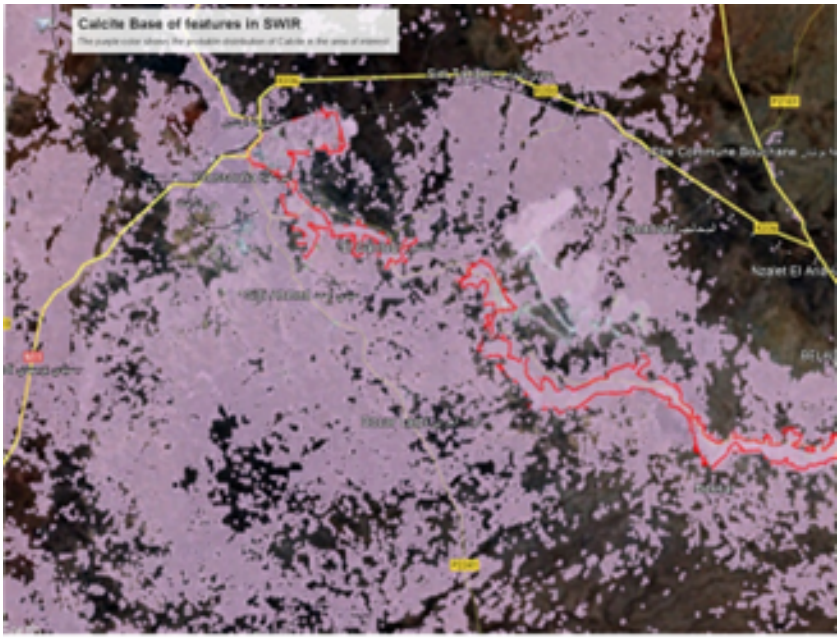

Calcite Mapping using EMIT sensor

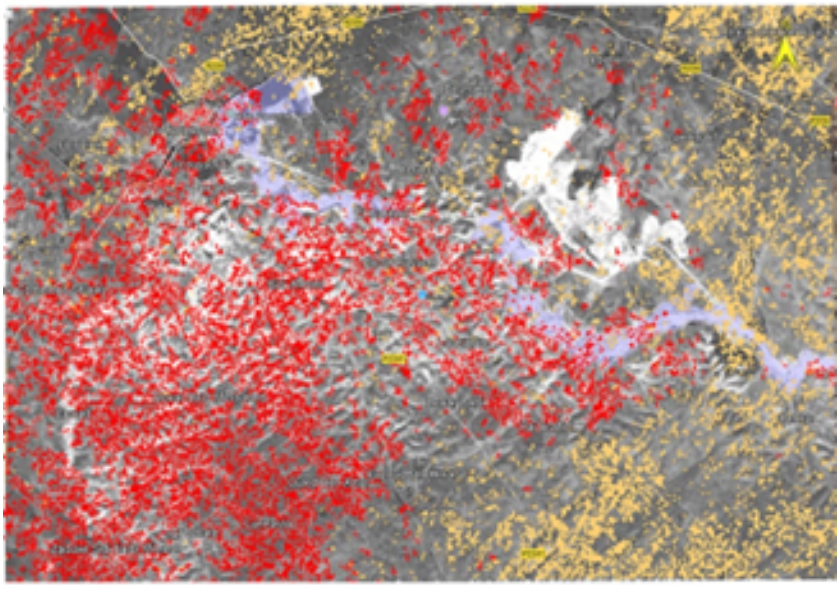

Calcite Mapping using ECOSTRESS sensor

Figure 5.2: Comparison of results of SWIR and TIR analysis for Calcite

5.1.2 Illite and Kaolinite (Clay minerals) and Gypsum (Sulfate mineral)

SWIR Absorption

All three minerals (illite, kaolinite, gypsum) exhibit strong absorption features around 2200 nm in the SWIR region.

Geographic Location: EMIT mapping reveals these minerals in the upper right corner of the region of interest, where band math identifies a common location for all three.

5.1.3 Illite & Kaolinite:

- Both show sharp absorption features near 2.2 µm, due to Al-OH bonds.
- Kaolinite has more pronounced doublet features at this wavelength.

5.1.4 Gypsum:

- Displays a strong absorption at 2.1 µm (due to SO stretching).
- Additional weaker absorption between 2.25–2.4 µm, related to water and sulfate interactions.

Thermal Infrared (ECOSTRESS)

Kaolinite, gypsum, and illite each have distinct absorption features in the thermal infrared range. Kaolinite is identified by its absorption around 9.6 µm and 10.4 µm due to Si-O stretching vibrations. Gypsum shows features near 8.6 µm and 11.1 µm, linked to sulfate ion vibrations. Illite has absorption features around 9.0 µm and 10.0 µm, primarily from Al-OH and Si-O vibrations. These characteristics are crucial for remote sensing and mineral exploration, enabling the identification and mapping of these minerals [**laukamp2021**].

However, due to the limited number of bands in ECOSTRESS, many of these features are lost during resampling. As a result, the analysis relies on resampled patterns of the spectra. While there are some similarities between the results in the SWIR and TIR regions, they may not be conclusive in the TIR range.

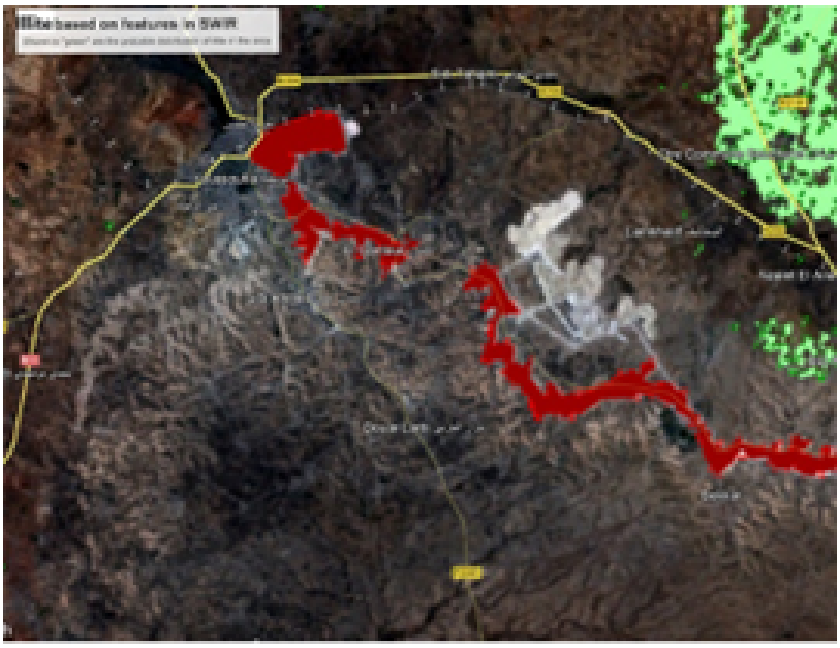

Mapping of ILLITE in SWIR using EMIT sensor

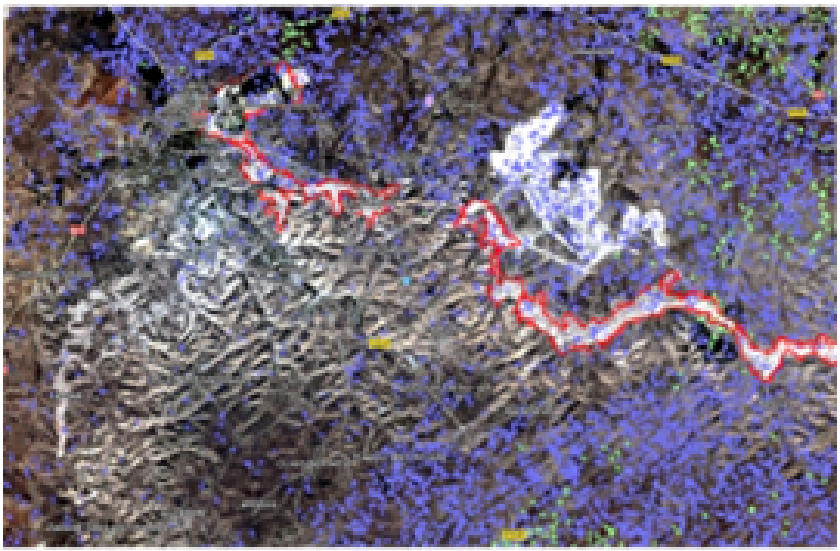

Mapping of ILLITE in TIR using ECOSTRESS sensor

Figure 5.3: Comparison of results of SWIR and TIR analysis for Illite

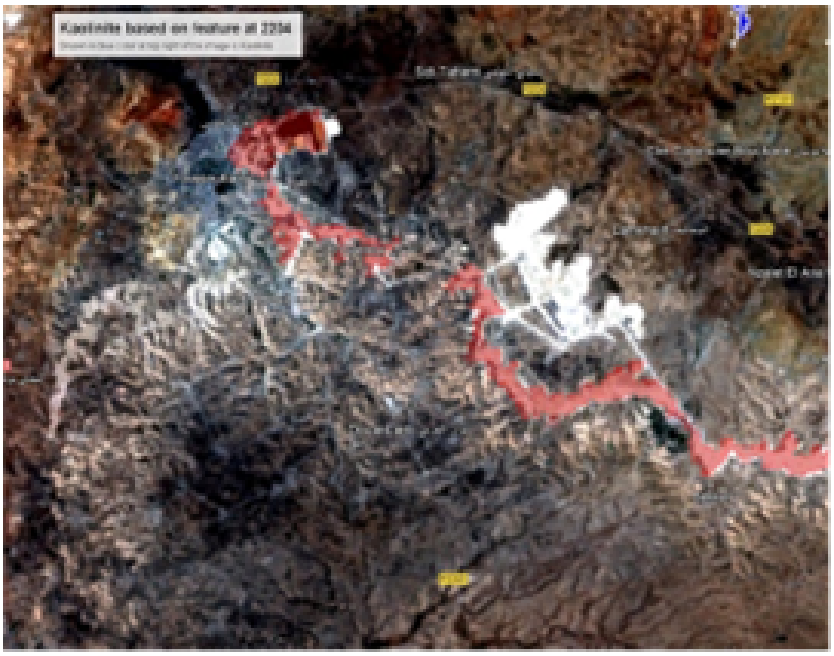

Figure 5.4: Result of SWIR for Kaolinite hyperspectral analysis

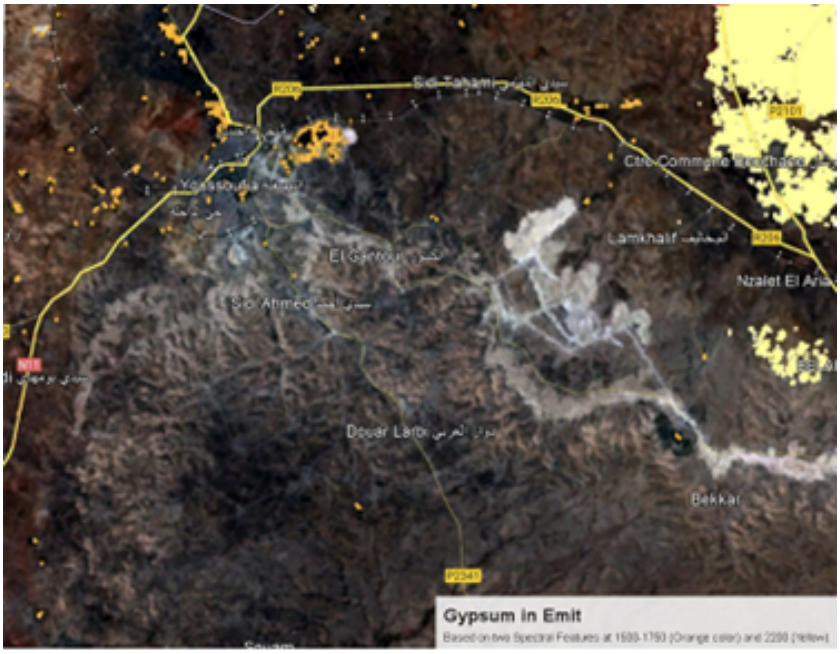

Mapping of Gypsum in SWIR using EMIT sensor

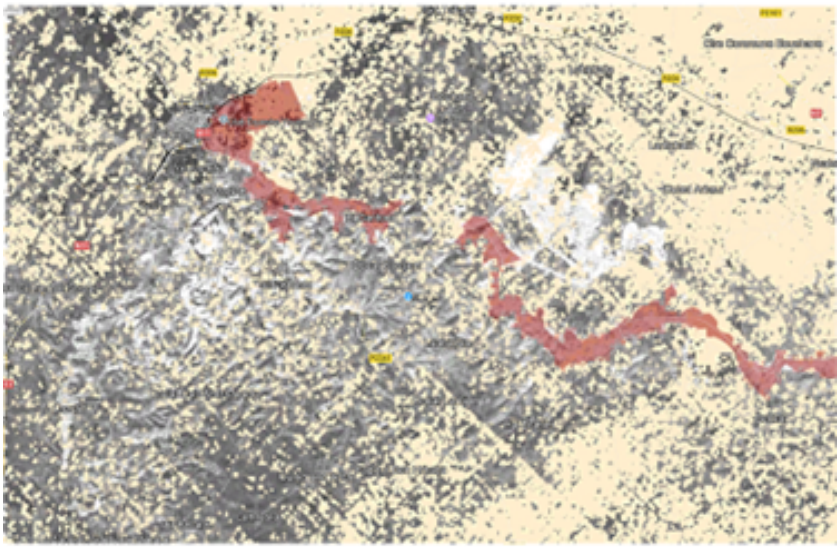

Mapping of Gypsum in TIR using ECOSTRESS sensor

Figure 5.5: Comparison of results of SWIR and TIR spectral analysis for Gypsum

5.1.5 Sepiolite Absorption Features

In the shortwave infrared (SWIR) range, sepiolite exhibits distinct absorption features due to its hydroxyl (OH) groups and water content. The weak absorptions at 1.4 µm and 1.9 µm are linked to the overtone and combination bands of water and OH, while the absorption near 2340 nm is associated with Mg-OH vibrations.

In the thermal infrared (TIR) range, sepiolite's unique fibrous structure and composition give rise to absorption features around 9.4 µm and 10.6 µm, corresponding to Si-O stretching and Mg-OH bending vibrations. However, due to the limitations of the sensor, these features cannot be detected in the TIR range.

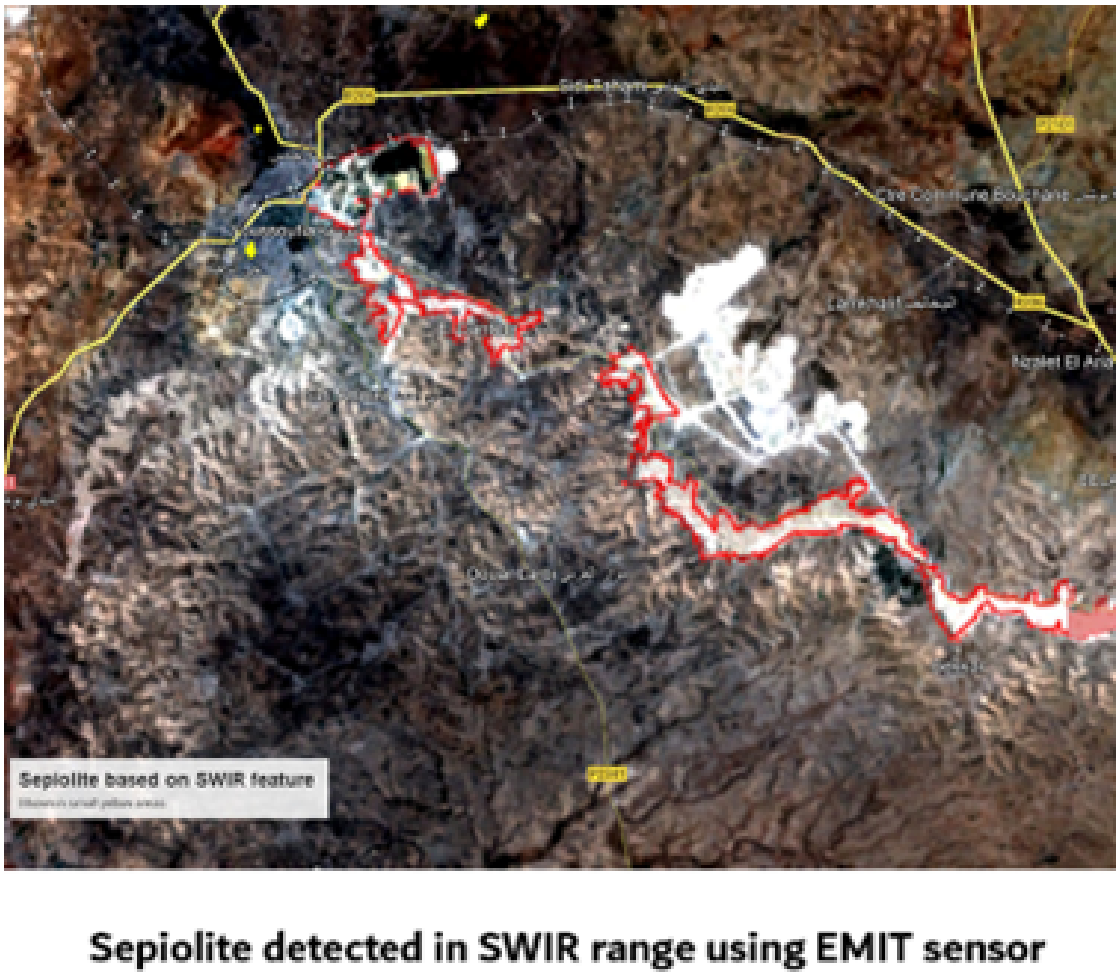

Figure 5.6: SWIR Analysis of Sepiolite

5.1.6 Apatite (phosphate mineral)

Mapping of Apatite in SWIR using EMIT sensor

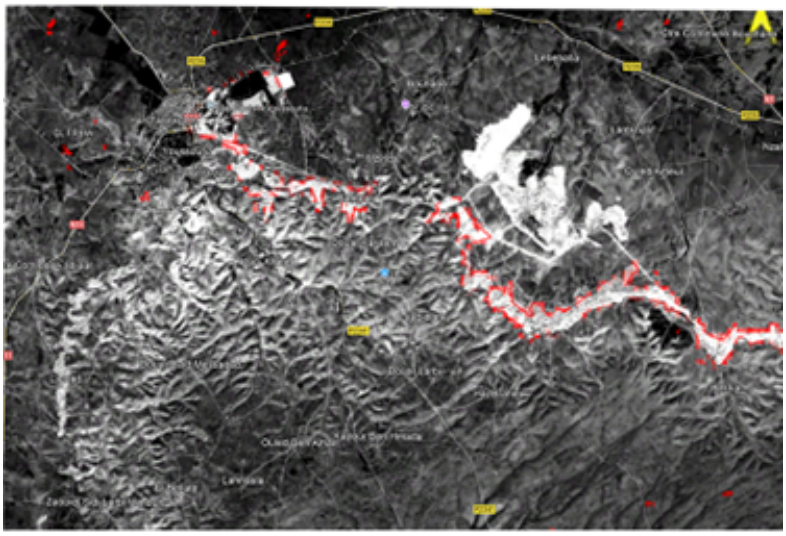

Mapping of Apatite in TIR using ECOSTRESS sensor

Figure 5.7: Comparison of results of SWIR and TIR spectral analysis for Apatiteaption

SWIR Spectral Features of Apatite

Apatite exhibits absorption features around 1400 nm, 1900 nm, and 2200 nm. These bands are primarily due to the presence of hydroxyl (OH) and phosphate (PO) groups [**ptacek2016**]. While apatite does show distinct absorption features in the SWIR region, these features are often not strong enough to be reliably detected using remote sensing images. This limitation arises from the relatively weak reflectance characteristics of apatite in the SWIR region, which can be overshadowed by other minerals and surface materials. Additionally, the presence of other minerals with similar spectral features can lead to false positives, making it challenging to accurately identify apatite using remote sensing techniques.

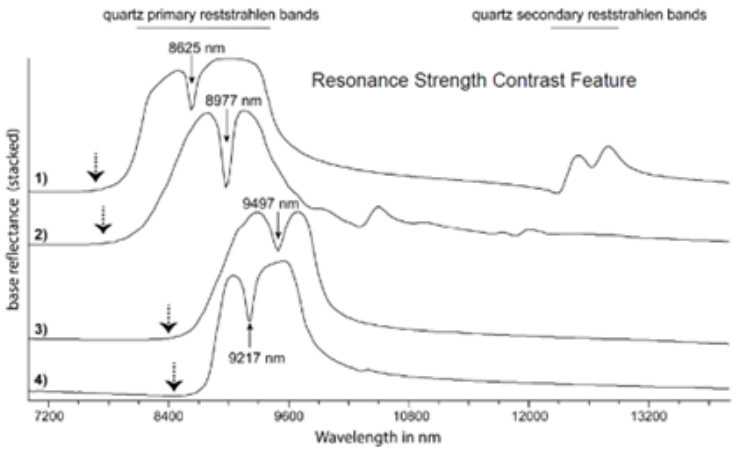

Figure 5.8: The figure shows the TIR reflectance spectra for quartz, pyrophyllite, talc, and apatite. The specific wavelengths corresponding to the respective Resonance Strength Contrast (RSC) features are highlighted in nanometers, along with the wavelength ranges for quartz's primary and secondary reststrahlen bands (with the secondary band represented by horizontal lines at the top of the figure). The position of the Christiansen minimum in each spectrum is marked with a dotted arrow.

The resampled spectra of apatite in ECOSTRESS can effectively capture its distinct feature at 9160 nm, commonly known as a reststrahlen band. This feature, characterized by an M-shaped curve, is a result of strong reflectance from the crystal structure of apatite, particularly in the thermal infrared region. Since ECOSTRESS has a band available near 9200 nm, it aligns well with this spectral signature, allowing for efficient detection of apatite's reststrahlen bands despite the sensor's limited spectral resolution. This makes ECOSTRESS suitable for identifying apatite even with resampled data.

5.1.7 Quartz (Silicate Mineral)

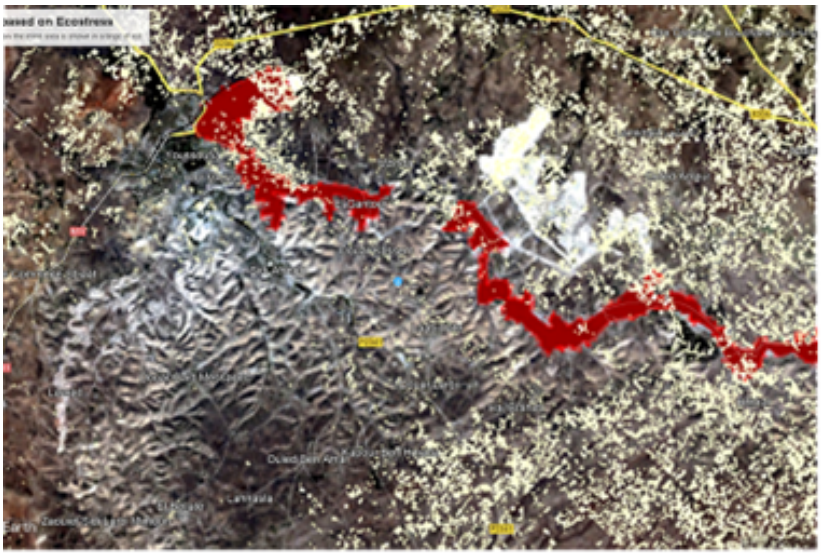

Figure 5.9: Distribution of Quartz (yellow) in the region of interest based on the spectral analysis in the TIR range utilizing ECOSTRESS sensor. Since quartz is featureless in SWIR, it cannot be detected in this range.

Similarly, for quartz, the resampled spectra in ECOSTRESS can capture its key feature at 8625 nm, another reststrahlen band. Although quartz's signature is slightly offset from the available 8780 nm band in ECOSTRESS, the proximity is close enough to still detect the characteristic M-shaped curve. This alignment allows ECOSTRESS to efficiently capture quartz's thermal infrared feature, despite the moderate spectral resolution. Together, these capabilities highlight how ECOSTRESS can effectively identify both apatite and quartz through their distinctive reststrahlen bands, even when dealing with resampled spectral data.

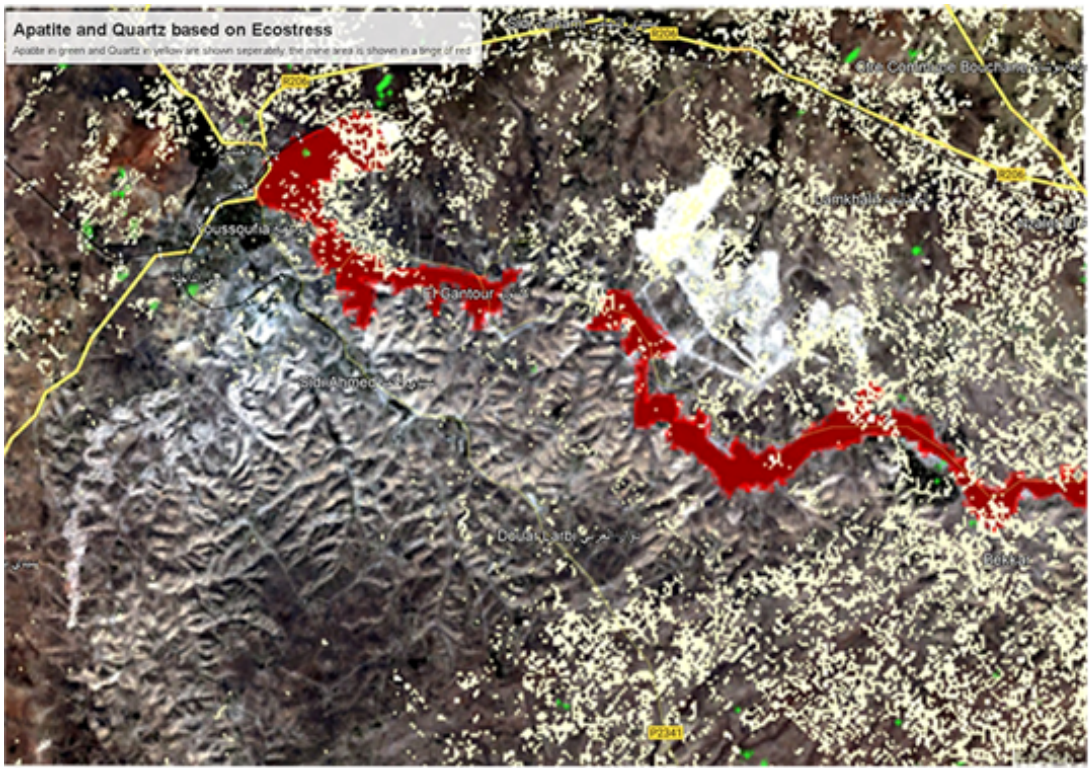

Figure 5.10: Well Separated distribution of Quartz (yellow) and Apatite(green) in the region of interest based on the spectral analysis in TIR range using ECOSTRESS sensor

5.2 Key Findings

ECOSTRESS was originally launched with the primary goal of measuring the evapotranspiration of plants, providing insight into how ecosystems respond to water availability and stress. However, in this study, its potential for detecting specific minerals has been successfully examined. By leveraging the sensor's thermal infrared capabilities, ECOSTRESS can capture key spectral features related to mineral composition, despite not being originally designed for this purpose. In this study, 2 methods of spectral analysis are examined. The first method focuses on using spectral features from the literature to identify minerals, creating a distribution diagram based on electromagnetic spectrum characteristics, and selecting samples from ENVI's spectral library. These samples are resampled to match the resolution of the observation device (e.g., ECOSTRESS or EMIT) before applying band math to highlight mineral signatures. Bad bands are discarded, and results are compared with reference ranges for validation. The second method applies band math to identify patterns in mineral distribution. However, it simplifies the data into Boolean outputs without a reference table, which may limit accuracy and validation, resulting in possible oversimplification and false positives or negatives.

booktabs graphicx array

Mineral	EMIT Band Math using reflectance reference tables	ECOSTRESS Band Math using reflectance reference tables	ECOSTRESS Band Math using Logical Constraints
Apatite	×	✓	✓
Quartz	×	✓	✓
Dolomite	✓	✓	✓
Kaolinite	✓	×	✓
Sepiolite	✓	×	×
Gypsum	✓	✓	×
Calcite	✓	✓	×
Illite	✓	✓	×

Figure 5.11: Detection possibility of different methods used in detecting minerals

The NDVI analysis for Youssoufia in 2023 highlights key environmental trends, showing minimal surface water and a predominance of low-canopy, drought-resistant vegetation. Vegetation peaks in March due to seasonal rains, while September shows the lowest density, reflecting the dry season's impact. High-canopy vegetation appears in microenvironments during November, March, and May, indicating areas with better growth conditions.

5.3 Limitations

5.3.1 Regarding Verification of the Results

The mineralogical and geological documentation for the area of interest is not publicly available, which poses a challenge for directly verifying the results obtained from remote sensing analysis. Without Geospatial Mineral Distribution maps or detailed geological reports, it becomes difficult to compare the spectral findings with established data. To ensure the accuracy of the results, ground truth validation is essential. Ground truthing involves collecting field samples and conducting on-site mineralogical analysis to cross-reference the remotely sensed data with physical samples from the area. This step is critical to verify the presence and distribution of the identified minerals and would strengthen the conclusions drawn from the remote sensing data.

However, conducting ground truth validation falls outside the scope of this research due to several limitations. First, logistical and resource constraints prevent extensive fieldwork in the area of interest. Additionally, the focus of this study is on evaluating the capability of remote sensing techniques, particularly using ECOSTRESS data, to detect and map specific minerals. Given the emphasis on methodological development and spectral analysis, incorporating on-site validation would require a significant expansion of the project's timeframe and resources. As a result, while ground truthing is crucial for future studies, this research remains focused on demonstrating the potential of remote sensing tools in mineral exploration.

5.3.2 Regarding Sensors

The sensors used in this study, EMIT and ECOSTRESS, while relatively new and advanced, have certain limitations in spectral and hyperspectral analysis. EMIT (Earth Surface Mineral Dust Source Investigation) is a hyperspectral sensor designed to detect and map surface minerals with high precision. However, like many remote sensing instruments, it may face challenges in fully capturing subtle mineralogical variations due to spectral resolution limitations, atmospheric interference, or the inherent complexity of mineral signatures. Additionally, its coverage and data acquisition capabilities may limit the temporal frequency or geographic extent of observations, potentially leaving gaps in continuous monitoring of the region.

Similarly, ECOSTRESS (Ecosystem Spaceborne Thermal Radiometer Experiment on Space Station), while effective in detecting thermal features and providing useful data for mineral identification, is constrained by its spectral resolution, particularly in the thermal infrared (TIR) range. The sensor's limited number of bands in key spectral regions can result in the loss of fine spectral details during

resampling, which is crucial for distinguishing between similar minerals. Moreover, both sensors are susceptible to generating false positives or negatives, where minerals might be incorrectly identified due to overlapping spectral signatures or noise introduced during data acquisition and processing. These limitations highlight the need for careful interpretation of the data and the potential need for ground truth validation or supplementary data from other sources to mitigate the risk of inaccuracies and improve the reliability of the results.

Bibliography

[1] Oskar Bär. *Die Phosphate Marokkos*. Tech. rep. (cit. on pp. 2, 4).

[2] Mowafa Taib. *2019 Minerals Yearbook*. Tech. rep. 6. 2020, p. 29 (cit. on p. 2).

[3] Radouan El Bamiki, Otmane Raji, Muhammad Ouabid, Abdellatif Elghali, Oussama Khadiri Yazami, and Jean Louis Bodinier. *Phosphate rocks: A review of sedimentary and igneous occurrences in Morocco*. Oct. 2021. DOI: 10.3390/min11101137 (cit. on pp. 2, 3, 5, 9).

[4] *OCP annual report 2021*. Tech. rep. 2021 (cit. on p. 4).

[5] Joseph Chan, Jeffrey Cooke, Tibor Horvath, and Sarah Aziz. «Dust suppression of phosphate rock: Storage, conveyance and shipping». In: *Procedia Engineering*. Vol. 46. Elsevier Ltd, 2012, pp. 213–219. DOI: 10.1016/j.proeng.2012.09.467 (cit. on p. 7).

[6] Gebrehiwet Reta et al. «Environmental impact of phosphate mining and beneficiation: review». In: *International Journal of Hydrology* 2.4 (2018). DOI: 10.15406/ijh.2018.02.00106 (cit. on p. 7).

[7] Sha Huang, Lina Tang, Joseph P Hupy, Yang Wang, and Guofan Shao. «A commentary review on the use of normalized difference vegetation index (NDVI) in the era of popular remote sensing». In: *Journal of Forestry Research* 32.1 (2021), pp. 1–6. ISSN: 1993-0607. DOI: 10.1007/s11676-020-01155-1. URL: https://doi.org/10.1007/s11676-020-01155-1 (cit. on pp. 7, 14, 23).

[8] C K Huanc and Peur F Konn. *INFRARED STUDY OF THE CARBONATE MINERALS*. Tech. rep. 1960 (cit. on p. 7).

[9] Jihen Jalali, Pierre Gaudin, Hervé Capiaux, Emna Ammar, and Thierry Lebeau. «Fate and transport of metal trace elements from phosphogypsum piles in Tunisia and their impact on soil bacteria and wild plants». In: *Ecotoxicology and Environmental Safety* 174 (June 2019), pp. 12–25. ISSN: 10902414. DOI: 10.1016/j.ecoenv.2019.02.051 (cit. on pp. 7, 8).

[10] G Dongarrà, E Manno, D Varrica, M Lombardo, and M Vultaggio. «Study on ambient concentrations of PM10, PM10–2.5, PM2.5 and gaseous pollutants. Trace elements and chemical speciation of atmospheric particulates». In: *Atmospheric Environment* 44.39 (2010), pp. 5244–5257. ISSN: 1352-2310. DOI: https://doi.org/10.1016/j.atmosenv.2010.08.041. URL: https://www.sciencedirect.com/science/article/pii/S1352231010007260 (cit. on p. 7).

[11] M. Lghoul, A. Maqsoud, R. Hakkou, and A. Kchikach. «Hydrogeochemical behavior around the abandoned Kettara mine site, Morocco». In: *Journal of Geochemical Exploration* 144.PC (2014), pp. 456–467. ISSN: 03756742. DOI: 10.1016/j.gexplo.2013.12.003 (cit. on p. 7).

[12] S Rodríguez et al. «Transport of desert dust mixed with North African industrial pollutants in the subtropical Saharan Air Layer». In: *Atmos. Chem. Phys.* 11.13 (July 2011), pp. 6663–6685. ISSN: 1680-7324. DOI: 10.5194/acp-11-6663-2011. URL: https://acp.copernicus.org/articles/11/6663/2011/%20https://acp.copernicus.org/articles/11/6663/2011/acp-11-6663-2011.pdf (cit. on p. 7).

[13] A. Khalil, L. Hanich, A. Bannari, L. Zouhri, O. Pourret, and R. Hakkou. «Assessment of soil contamination around an abandoned mine in a semi-arid environment using geochemistry and geostatistics: Pre-work of geochemical process modeling with numerical models». In: *Journal of Geochemical Exploration* 125 (Feb. 2013), pp. 117–129. ISSN: 03756742. DOI: 10.1016/j.gexplo.2012.11.018 (cit. on p. 8).

[14] Eduardo Ferreira da Silva, Ammar Mlayah, Celso Gomes, Fernando Noronha, Abdelkrim Charef, Cristina Sequeira, Valdemar Esteves, and Ana Raquel Figueiredo Marques. «Heavy elements in the phosphorite from Kalaat Khasba mine (North-western Tunisia): Potential implications on the environment and human health». In: *Journal of Hazardous Materials* 182.1-3 (Oct. 2010), pp. 232–245. ISSN: 03043894. DOI: 10.1016/j.jhazmat.2010.06.020 (cit. on p. 8).

[15] Adam T. Cross and Hans Lambers. *Young calcareous soil chronosequences as a model for ecological restoration on alkaline mine tailings*. Dec. 2017. DOI: 10.1016/j.scitotenv.2017.07.005 (cit. on p. 8).

[16] Rachid Hakkou, Mostafa Benzaazoua, and Bruno Bussière. «Valorization of Phosphate Waste Rocks and Sludge from the Moroccan Phosphate Mines: Challenges and Perspectives». In: *Procedia Engineering*. Vol. 138. Elsevier Ltd, 2016, pp. 110–118. DOI: 10.1016/j.proeng.2016.02.068 (cit. on p. 8).

[17] Rachid Hakkou, Mostafa Benzaazoua, and Bruno Bussière. «Valorization of Phosphate Waste Rocks and Sludge from the Moroccan Phosphate Mines: Challenges and Perspectives». In: *Procedia Engineering* 138 (2016), pp. 110–118. ISSN: 18777058. DOI: 10.1016/j.proeng.2016.02.068 (cit. on p. 8).

[18] Hamza Zine, Rachid Hakkou, Abdelhak Elmansour, Sara Elgadi, Ahmed Ouhammou, and Mostafa Benzaazoua. «Native plant diversity for ecological reclamation in Moroccan open-pit phosphate mines». In: *Biodiversity Data Journal* 11 (July 2023). ISSN: 1314-2828. DOI: 10.3897/BDJ.11.e104592 (cit. on p. 8).

[19] Bilal BOUMAZA and Tatyana Vladimirovna CHEKUSHINA. «Assessment of metallic trace elements contamination in a mining area of the processing of Djebel Onk phosphate ore (Algeria)». In: *NEWS of the Ural State Mining University* 1 (Mar. 2021), pp. 7–16. ISSN: 23072091. DOI: 10.21440/2307-2091-2021-1-7-16 (cit. on p. 8).

[20] Najoua Mghazli, Laila Sbabou, Rachid Hakkou, Ahmed Ouhammou, Mariam El Adnani, and Odile Bruneel. «Description of Microbial Communities of Phosphate Mine Wastes in Morocco, a Semi-Arid Climate, Using High-Throughput Sequencing and Functional Prediction». In: *Frontiers in Microbiology* 12 (July 2021). ISSN: 1664302X. DOI: 10.3389/fmicb.2021.666936 (cit. on p. 8).

[21] Carsten Laukamp, Andrew Rodger, Monica Legras, Heta Lampinen, Ian C. Lau, Bobby Pejcic, Jessica Stromberg, Neil Francis, and Erick Ramanaidou. «Mineral physicochemistry underlying feature-based extraction of mineral abundance and composition from shortwave, mid and thermal infrared reflectance spectra». In: *Minerals* 11.4 (Apr. 2021). ISSN: 2075163X. DOI: 10.3390/min11040347 (cit. on p. 8).

[22] N. Clavier, A. Mesbah, S. Szenknect, and N. Dacheux. «Monazite, rhabdophane, xenotime & churchite: Vibrational spectroscopy of gadolinium phosphate polymorphs». In: *Spectrochimica Acta - Part A: Molecular and Biomolecular Spectroscopy* 205 (Dec. 2018), pp. 85–94. ISSN: 13861425. DOI: 10.1016/j.saa.2018.07.016 (cit. on p. 10).

[23] H.H Adler. *INFRARED SPECTRA OF PHOSPHATE MINERALS: SYMMETRY AND SUBSTITUTIONAL EFFECTS IN THE PYROMORPHITE SERIES*. Tech. rep. 1964 (cit. on p. 10).

[24] Roger N Clark. *USGS Spectroscopy Lab: Spectroscopy of Rocks and Minerals, and Principles of Spectroscopy Spectroscopy of Rocks and Minerals, and Principles of Spectroscopy*. Tech. rep. 1999. URL: http://speclab.cr.usgs.govhttp://speclab.cr.usgs.gov/PAPERS.refl-mrs/ (cit. on pp. 10, 11, 13–15, 17).

[25] SuseN J Gerrsvt. *Spectral reflectance of-carbonate minerals in the visible and near infrared (0.35-2.55 microns): calcite, aragonite, and dolomite*. Tech. rep. 1986, pp. 151–162 (cit. on p. 10).

[26] Enton Bedini. *OPEN JOURNAL SYSTEMS Journal of Hyperspectral Remote Sensing The use of hyperspectral remote sensing for mineral exploration: a review*. Tech. rep. 4. 2017, pp. 189–211. URL: www.periodicos.ufpe.br/revistas/jhrs (cit. on p. 11).

[27] Freek D van der Meer et al. «Multi- and hyperspectral geologic remote sensing: A review». In: *International Journal of Applied Earth Observation and Geoinformation* 14.1 (2012), pp. 112–128. ISSN: 1569-8432. DOI: https://doi.org/10.1016/j.jag.2011.08.002. URL: https://www.sciencedirect.com/science/article/pii/S0303243411001103 (cit. on p. 11).

[28] John W Salisbury and Dana M D'Aria. «Infrared (8–14 μm) remote sensing of soil particle size». In: *Remote Sensing of Environment* 42.2 (1992), pp. 157–165. ISSN: 0034-4257. DOI: https://doi.org/10.1016/0034-4257(92)90099-6. URL: https://www.sciencedirect.com/science/article/pii/0034425792900996 (cit. on pp. 11, 13–16).

[29] W G Spitzer and D A Kleinman. «Infrared Lattice Bands of Quartz». In: *Physical Review* 121.5 (Mar. 1961), pp. 1324–1335. DOI: 10.1103/PhysRev.121.1324. URL: https://link.aps.org/doi/10.1103/PhysRev.121.1324 (cit. on p. 11).

[30] Robert D. Hewson, Thomas J. Cudahy, Malcolm Jones, and Matilda Thomas. «Investigations into Soil Composition and Texture Using Infrared Spectroscopy (2–14 <math id="M1"> <mrow> <mi mathvariant="bold-italic">μ</mi> </mrow> </math> m)». In: *Applied and Environmental Soil Science* 2012 (2012), pp. 1–12. ISSN: 1687-7667. DOI: 10.1155/2012/535646 (cit. on p. 11).

[31] Mark P Simpson. *Reflectance spectrometry [SWIR] of alteration minerals surrounding the Favona epithermal vein. Waihi vein system, Hauraki Goldfield*. Tech. rep. 2022. URL: https://www.researchgate.net/publication/282933781 (cit. on pp. 11, 64).

[32] Nasrullah Zaini. *Calcite-Dolomite Mapping to Assess Dolomitization Patterns Using Laboratory Spectra and Hyperspectral Remote Sensing: A Case Study of Bédarieux Mining Area, SE France*. Tech. rep. 2009 (cit. on pp. 13, 14).

[33] Huang CK and Kerr PF. « Infrared study of the carbonate minerals.» In: *The American Mineralogist* 45 (1961), pp. 311–324 (cit. on p. 13).

[34] Graham R Hunt and J Salisbury. «Visible and near infrared spectra of minerals and rocks. II. Carbonates». In: 1971. URL: https://api.semanticscholar.org/CorpusID:128727775 (cit. on pp. 13–16).

[35] Susan J. Gaffey. «Spectral Reflectance Of-Carbonate Minerals in the Visible and near Infrared (0.35-2.55 Microns): Calcite, Aragonite, and Dolomite.» In: *American Mineralogist* 71 (1986) (cit. on pp. 13, 14).

[36] Freek Van der Meer. «Spectral reflectance of carbonate mineral mixtures and bidirectional reflectance theory: Quantitative analysis techniques for application in remote sensing». In: *Remote Sensing Reviews* 13.1-2 (Aug. 1995), pp. 67–94. ISSN: 0275-7257. DOI: 10.1080/02757259509532297. URL: https://doi.org/10.1080/02757259509532297 (cit. on pp. 13, 14).

[37] F. Bosch Reig, J. V.Gimeno Adelantado, and M. C.M. Moya Moreno. «FTIR quantitative analysis of calcium carbonate (calcite) and silica (quartz) mixtures using the constant ratio method. Application to geological samples». In: *Talanta* 58.4 (Oct. 2002), pp. 811–821. ISSN: 00399140. DOI: 10.1016/S0039-9140(02)00372-7 (cit. on pp. 13, 14).

[38] N Öztan and Mehmet Süzen. «Mapping evaporate minerals by ASTER». In: *International Journal of Remote Sensing* 32 (Mar. 2011), pp. 1651–1673. DOI: 10.1080/01431160903586799 (cit. on p. 15).

[39] Asad Khan, Shah Faisal, Muhammad Shafique, Saad Khan, and Alam Sher Bacha. «ASTER-based remote sensing investigation of gypsum in the Kohat Plateau, north Pakistan». In: *Carbonates and Evaporites* 35.1 (Mar. 2020). ISSN: 18785212. DOI: 10.1007/s13146-019-00543-x (cit. on p. 15).

[40] Raymond F Kokaly and Roger N Clark. *Spectroscopic Determination of Leaf Biochemistry Using Band-Depth Analysis of Absorption Features and Stepwise Multiple Linear Regression The measurement of plant biochemical content by.* Tech. rep. 1999 (cit. on p. 15).

[41] James K Crowley. «Visible and near-infrared (0.4–2.5 μm) reflectance spectra of Playa evaporite minerals». In: *Journal of Geophysical Research: Solid Earth* 96.B10 (Sept. 1991), pp. 16231–16240. ISSN: 0148-0227. DOI: https://doi.org/10.1029/91JB01714. URL: https://doi.org/10.1029/91JB01714 (cit. on pp. 15, 74).

[42] Raymond F Kokaly, Trude V V King, and Todd M Hoefen. *MAPPING THE DISTRIBUTION OF MATERIALS IN HYPERSPECTRAL DATA USING THE USGS MATERIAL IDENTIFICATION AND CHARACTERIZATION ALGORITHM (MICA).* Tech. rep. 2011 (cit. on p. 15).

[43] Robert Milewski, Sabine Chabrillat, and Robert Behling. «Analyses of recent sediment surface dynamic of a Namibian Kalahari salt pan based on multi-temporal landsat and hyperspectral hyperion data». In: *Remote Sensing* 9.2 (2017). ISSN: 20724292. DOI: 10.3390/rs9020170 (cit. on p. 16).

[44] Janice L. Bishop. «Visible and Near-Infrared Reflectance Spectroscopy». In: *Remote Compositional Analysis*. Cambridge University Press, Nov. 2019, pp. 68–101. DOI: 10.1017/9781316888872.006 (cit. on p. 16).

[45] Andrea García-Vicente, Adrián Lorenzo, Juan Morales, Emilia García-Romero, and Mercedes Suárez. «Field Spectroscopy Applied to the Kaolinite Polytypes Identification». In: MDPI AG, June 2021, p. 16. DOI: 10.3390/iecms2021-09353 (cit. on p. 16).

[46] G. W. Brindley, Chih-Chun Kao, J. L. Harrison, M. Lipsicas, and R. Raythatha. «Relation Between Structural Disorder and Other Characteristics of Kaolinites and Dickites». In: *Clays and Clay Minerals* 34.3 (June 1986), pp. 239–249. ISSN: 0009-8604. DOI: 10.1346/CCMN.1986.0340303 (cit. on p. 17).

[47] Ursula Johansson, Ray L Frost, Willis Forsling, and J Theo Kloprogge. «Raman Spectroscopy of the Kaolinite Hydroxyls at 77 K». In: *Appl. Spectrosc.* 52.10 (Oct. 1998), pp. 1277–1282. URL: https://opg.optica.org/as/abstract.cfm?URI=as-52-10-1277 (cit. on p. 17).

[48] *EMIT Specifications*. 2024. URL: https://earth.jpl.nasa.gov/emit/instrument/specifications/ (cit. on p. 22).

[49] Sally Younger. *https://ecostress.jpl.nasa.gov/*. 2024. URL: https://ecostress.jpl.nasa.gov/ (cit. on pp. 22, 29).

[50] *Landsat 9*. 2024. URL: https://landsat.gsfc.nasa.gov/satellites/landsat-9/ (cit. on p. 22).

[51] Compton J Tucker. «Red and photographic infrared linear combinations for monitoring vegetation». In: *Remote Sensing of Environment* 8.2 (1979), pp. 127–150. ISSN: 0034-4257. DOI: https://doi.org/10.1016/0034-4257(79)90013-0. URL: https://www.sciencedirect.com/science/article/pii/0034425779900130 (cit. on pp. 23, 26).

[52] Jr. Rouse J.
W., R. H. Haas, J. A. Schell, and D. W. Deering. «Monitoring Vegetation Systems in the Great Plains with Erts». In: *NASA Special Publication*. Ed. by Stanley C Freden, Enrico P Mercanti, and Margaret A Becker. Vol. 351. 1974, p. 309 (cit. on pp. 23, 26).

[53] Genesis T Yengoh, David Dent, Lennart Olsson, Anna E Tengberg Compton, and J Tucker Iii. *SPRINGER BRIEFS IN ENVIRONMENTAL SCIENCE Use of the Normalized Diff erence Vegetation Index (NDVI) to Assess Land Degradation at Multiple Scales Current Status, Future Trends, and Practical Considerations*. Tech. rep. 2015. URL: http://www.springer.com/series/8868 (cit. on p. 23).

[54] R Person. «Remote mapping of standing crop biomass for estimation of the productivity of the short-grass Prairie, Pawnee National Grasslands, Colorado». In: 1972. URL: https://api.semanticscholar.org/CorpusID:204258424 (cit. on p. 26).

[55] A Huete, K Didan, T Miura, E P Rodriguez, X Gao, and L G Ferreira. «Overview of the radiometric and biophysical performance of the MODIS vegetation indices». In: *Remote Sensing of Environment* 83.1 (2002), pp. 195–213. ISSN: 0034-4257. DOI: https://doi.org/10.1016/S0034-4257(02)00096-2. URL: https://www.sciencedirect.com/science/article/pii/S0034425702000962 (cit. on p. 26).

[56] A J Richardsons and A Wiegand. «DISTINGUISHING VEGETATION FROM SOIL BACKGROUND INFORMATION». In: *Photogrammetric Engineering and Remote Sensing* 43 (1977), pp. 1541–1552. URL: https://api.semanticscholar.org/CorpusID:126604551 (cit. on p. 26).

[57] A R Huete. «A soil-adjusted vegetation index (SAVI)». In: *Remote Sensing of Environment* 25.3 (1988), pp. 295–309. ISSN: 0034-4257. DOI: https://doi.org/10.1016/0034-4257(88)90106-X. URL: https://www.sciencedirect.com/science/article/pii/003442578890106X (cit. on p. 26).

[58] J Qi, A Chehbouni, A R Huete, Y H Kerr, and S Sorooshian. «A modified soil adjusted vegetation index». eng. In: *Remote Sensing of Environment.* 48.2 (1994), pp. 119–126. ISSN: 0034-4257. DOI: 10.1016/0034-4257(94)90134-1. URL: http://europepmc.org/abstract/AGR/IND20402188%20https://doi.org/10.1016/0034-4257(94)90134-1 (cit. on p. 26).

[59] F Baret and G Guyot. «Potentials and limits of vegetation indices for LAI and APAR assessment». In: *Remote Sensing of Environment* 35.2 (1991), pp. 161–173. ISSN: 0034-4257. DOI: https://doi.org/10.1016/0034-4257(91)90009-U. URL: https://www.sciencedirect.com/science/article/pii/003442579190009U (cit. on p. 26).

[60] Y J Kaufman and D Tanre. «Atmospherically resistant vegetation index (ARVI) for EOS-MODIS». In: *IEEE Transactions on Geoscience and Remote Sensing* 30.2 (1992), pp. 261–270. DOI: 10.1109/36.134076 (cit. on p. 26).

[61] David R Thompson, Philip Brodrick, Robert O Green, Olga Kalashnikova, Sarah Lundeen, Gregory Okin, Winston Olson-Duvall, and Thomas Painter. *Earth Mineral dust source InvesTigation (EMIT) EMIT L2A Algorithm: Surface Reflectance and Scene Content Masks Theoretical Basis*. Tech. rep. 2020 (cit. on p. 29).

[62] LP DAAC. *LP DAAC Data User Resources: ECOSTRESS_swath2grid*. English. Nov. 2022. URL: https://git.earthdata.nasa.gov/projects/LPDUR/repos/ecostress_swath2grid/browse (cit. on p. 29).

[63] Hamza Zine, Rachid Hakkou, Abdelhak Elmansour, Sara Elgadi, Ahmed Ouhammou, and Mostafa Benzaazoua. «Native plant diversity for ecological reclamation in Moroccan open-pit phosphate mines». In: *Biodiversity Data Journal* 11 (2023). ISSN: 13142828. DOI: 10.3897/BDJ.11.E104592 (cit. on p. 41).

[64] Soufian Chakkour, Erwin Bergmeier, Stefan Meyer, Jalal Kassout, Mohamed Kadiri, and Mohammed Ater. «Plant diversity in traditional agroecosystems of North Morocco». In: *Vegetation Classification and Survey* 4 (2023), pp. 31–45. ISSN: 26830671. DOI: 10.3897/VCS.86024 (cit. on p. 41).

[65] Bruce Hapke. *Theory of Reflectance and Emittance Spectroscopy*. Cambridge University Press, Jan. 2012. ISBN: 9780521883498. DOI: 10.1017/CBO9781139025683 (cit. on p. 43).

[66] Robert A. Schowengerdt. *Remote Sensing*. Elsevier, 2007. ISBN: 9780123694072. DOI: 10.1016/B978-0-12-369407-2.X5000-1 (cit. on p. 43).

[67] Roger N. Clark and Ted L. Roush. «Reflectance spectroscopy: Quantitative analysis techniques for remote sensing applications». In: *Journal of Geophysical Research: Solid Earth* 89.B7 (July 1984), pp. 6329–6340. ISSN: 0148-0227. DOI: 10.1029/JB089iB07p06329 (cit. on p. 74).